STARS

2015

Optical Propagation of Self-sustaining Wavefronts and Nonlinear Dynamics in Parabolic Multimode Fibers

Matthew Mills
University of Central Florida

Showcase of Text, Archives, Research & Scholarship

OPTICAL PROPAGATION OF SELF-SUSTAINING WAVEFRONTS

AND

NONLINEAR DYNAMICS IN PARABOLIC MULTIMODE FIBERS

by

MATTHEW STEPHEN MILLS
B.S. Rose-Hulman Institute of Technology, 2010
M.S. Unversity of Central Florida, 2012
Ph.D University of Central Florida, 2015

A dissertation submitted in partial fulfillment of the requirements
for the degree of Doctor of Philosophy
in the College of Optics and Photonics
at the University of Central Florida
Orlando, Florida

Fall Term
2015

Major Professor: Demetri Christodoulides

ABSTRACT

The aim of this thesis is to introduce my work which has generally been focused on optical wavefronts that have the unusual property of resisting commonplace phenomena such as diffraction and dispersion. Interestingly, these special beams are found both in linear and nonlinear situations. For example, in the linear regime, localized spatio-temporal waves which resemble the spherical harmonic symmetries of the hydrogen quantum orbitals can simultaneously negotiate both diffractive and dispersive effects. In the nonlinear regime, dressed optical filaments can be arranged to propagate multi-photon produced plasma channels orders of magnitude longer than expected.

The first portion of this dissertation will begin by surveying the history of diffraction-free beams and introducing some of their mathematical treatments. Interjected throughout this discussion will be several relevant concepts which I explored during my first years a CREOL. The discussion will then be steered into a detailed account of diffraction/dispersion free wavefronts which display hydrogen-like symmetries. The second segment of the document will cover the highly nonlinear process of optical filamentation. This chapter will almost entirely investigate the idea of the dressed filament, an entity which allows for substantial prolongation of this light string. I will then conclude by delving into the topic of supercontinuum generation in parabolic multimode fibers which, in the upcoming years, has great potential of becoming important in optics.

Dedicated to Emily Lakes

ACKNOWLEDGMENT

This dissertation is most deservingly dedicated to many individuals who helped guide me during my Ph.D studies at CREOL. First and foremost, I would like to thank my advisor, Demetri Christodoulides, whom has shaped a large portion of my formative years as a professional scientist; in my future endeavors, I can only hope to emulate the same passion and charisma he showed.

I am very grateful to Professor Miroslav Kolesik of the University of Arizona for his kindness, patience, and willingness to integrate me in his own research project. I learned a great deal of skills through his guidance and I could not have completed this dissertation without his help.

I must also thank Dr. Frank Wise of Cornell University and his research group for their involvement with our research efforts. The latter end of this dissertation is certainly a direct result of our collaboration.

I am so glad to have met and interacted with each and every member of the nonlinear wave propagation group at CREOL: Dr. Mohammad Ali Miri, Parinaz Aleahmad, Ahmed El Halawani, Mohammad Amin Eftekhar, Absar Hassan, Nicolas Nye, Midya Parto, Fan Wu, and Armando Perez-Leija.

The staff of CREOL has always been so cheerful and helpful to me throughout my stay – I am very much appreciative of them.

Finally, I would like to express my appreciation for the constant unyielding support I received from my family and friends throughout graduate school: Craig Mills, Mary Lou Mills, Mike Mills, Mark Mills, Monica Mills, Emily and the Lakes family, Bill and Kaye Branson, Mitch Saunders, Elizabeth Finn, Janet Feldman, Rosie and Joe Jenne, Michael Gates, The Muche family, Larry, Jason, Scott, Tony and Kristina Klee, Matthew Reichert, Casey Kretzer, Richard Lepkowicz, Bobby Brown, and Charlotte Cuevas.

TABLE OF CONTENTS

LIST OF FIGURES

LIST OF ABBREVIATIONS

CREOL: The College of Optics and Photonics, iii

FWHM: Full Width Half Maximum, 55

PDW: Pump Dispersive Wave, 83

RS: Raman Scattering, 83

RSDW: Raman Scattering Dispersive Wave, 84

SPM: Self Phase Modulation, 80

THG: Third Harminc Generation, 84

UPPE: Unidirectional Pulse Propagation Equations, 43

CHAPTER ONE: LINEAR DIFFRACTIONLESS OPTICAL BEAMS

1.1. Diffraction and the paraxial wave equation

Diffraction, whose Latin roots translate as "to break into pieces", is a characteristic of light resulting from its wave nature. By definition, diffraction is any deviation a light ray takes from a rectilinear path that cannot be explained as reflection or refraction [1]. Specifically, the amplitude and phase of a wavefront is altered as it propagates because of lateral confinement. In this section, we begin with Maxwell's equations, which govern the evolution of all electromagnetic waves, and reduce them down to the paraxial wave equation [2]. This equation, despite several simplifications, provides extremely good insight into the activity of laser beams and will pave the way into our discussion of diffractionless entities.

Maxwell's equations describe the evolution dynamics of electromagnetic waves in media,

$$\nabla \cdot \epsilon \vec{E}(x,y,z,t) = \rho \qquad\qquad \nabla \cdot \mu \vec{H}(x,y,z,t) = 0$$

$$\nabla \times \vec{E}(x,y,z,t) = -\mu \frac{\partial \vec{H}(x,y,z,t)}{\partial t} \qquad \nabla \times \vec{H}(x,y,z,t) = \sigma \vec{E}(x,y,z,t) + \epsilon \frac{\partial \vec{E}(x,y,z,t)}{\partial t}.$$

Where $\vec{E}(x,y,z,t)$ and $\vec{H}(x,y,z,t)$ are the electric and magnetic vector fields, ρ is the charge density, σ is the conductance, and ϵ and μ are respectively the permittivity and permeability of the medium. Let us suppose we are working in a lossless nonmagnetic ($\mu = \mu_0$) medium with no conductance, $\sigma = 0$, and no free charge density, $\rho = 0$. Within the scope of our assumptions, we can simplify things further by following a scalar electric field as opposed to the full vectorial treatment. By using the identity, $\nabla \times \nabla \times E = -\nabla^2 E + \nabla(\nabla \cdot E)$ we can easily combine these relationships to arrive at the wave equation,

$$\nabla^2 E(x,y,z,t) - \mu_0\epsilon \frac{\partial^2 E(x,y,z,t)}{\partial t^2} = 0.$$

Note that we are only following the electric field even though a similar equation can be obtained for the magnetic component. For the quasi-monochromatic wavefronts to be in question, the time dependence of $E(x,y,z,t)$ can be conveniently decomposed into a linearly independent sinusoid, $E(x,y,z,t) = E(x,y,z)\exp(-i\omega t)$. Inserting this into the wave equation results in the Helmholtz Equation,

$$\nabla^2 E(x,y,z) + k^2 E(x,y,z) = 0 \tag{1}$$

Where, $k = \omega\sqrt{\mu_0\epsilon} = n\omega\sqrt{\mu_0\epsilon_0} = 2\pi n/\lambda_0$, is known as the wavenumber and has been expressed in terms of an index of refraction, $n = \sqrt{\epsilon/\epsilon_0}$, and a wavelength, λ_0. At this point, we have nearly arrived at the paraxial wave equation. We only need to assume that the waveforms of interest are narrowly-banded in space and propagate primarily along one direction – a very good approximation of laser light, $E(x,y,z) = \psi(x,y,z)\exp(-ikz)$, (by convention the z direction). Substituting this into the Helmholtz equation produces the paraxial wave equation,

$$i\frac{\partial\psi(x,y,z)}{\partial z} + \frac{1}{2k}\nabla_\perp^2\psi(x,y,z) = 0. \tag{2}$$

Here, $\nabla_\perp^2 = \partial_{xx} + \partial_{yy}$, is the transverse Laplacian operator. The second term in (2) is linear in nature and responsible for encoding the diffraction or spreading of light waves.

If we briefly return to equation (1), a basic solution is a plane wave of the form, $\psi(x,y,z) = \psi_0\exp\left(-i[k_x x + k_y y + k_z z]\right)$ with $k^2 = k_x^2 + k_y^2 + k_z^2$. Owing to superposition, the most general solution is expressible as a Fourier transform,

$E(x,y,z) =$

$$\frac{1}{(2\pi)^2}\int_{-\infty}^{\infty}\int_{-\infty}^{\infty}\tilde{E}(k_x,k_y)\exp\left[-i\left(k_x x + k_y y + z\sqrt{k^2 - k_x^2 - k_y^2}\right)\right]dk_x dk_y \tag{3}$$

$$\tilde{E}(k_x, k_y) = \int_{-\infty}^{\infty}\int_{-\infty}^{\infty} E(x, y, z = 0) \exp\left[+i(k_x x + k_y y)\right] dx dy$$

Where the k-spectrum, $\tilde{E}(k_x, k_y)$ can be found at the starting position $z = 0$.

Although equation (3) is an exact solution to the Helmholtz equation and more general than the paraxial wave equation, the square root factor in the complex exponent prohibits integration in most cases. Fortunately, by transitioning equation (3) to the paraxial regime, we obtain a more agreeable integral. To do so, we only consider $\vec{k}$ vectors which propagate primarily in the $\hat{z}$ direction resulting in k_x/k and k_y/k being small terms (Fig. 1). This allows us to Taylor expand the square root, $\sqrt{k^2 - k_x^2 - k_y^2} = k\sqrt{1 - (k_x^2 + k_y^2)/k^2} \approx k - (k_x^2 + k_y^2)/2k$. We then obtain the more pliable formula:

$$\psi(x, y, z) = \frac{1}{(2\pi)^2}\int_{-\infty}^{\infty}\int_{-\infty}^{\infty}\tilde{\psi}(k_x, k_y)\exp\left[-i\left(k_x x + k_y y - \frac{z}{2k}(k_x^2 + k_y^2)\right)\right]dk_x dk_y \qquad (4)$$

$$\tilde{\psi}(k_x, k_y) = \int_{-\infty}^{\infty}\int_{-\infty}^{\infty}\psi(x, y, z = 0)\exp\left[+i(k_x x + k_y y)\right]dx dy$$
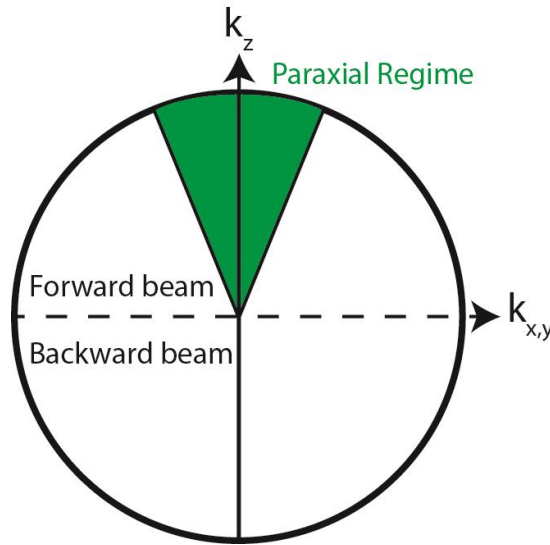
Figure 1| The paraxial wave equation accounts for only $\vec{k}$-vectors which are primarily in the $\hat{z}$ direction – a good approximation for laser light.

Note in equation (4) that each plane wave has a quadratic dependence on the lateral $\vec{k}$ vectors in the term proportional to z. This paints an intuitive picture of plane waves which spatially "walk-off" or "diffract" from one another in the transverse direction as they propagate. For an example, consider a standard Gaussian envelope given by $\psi(x, y, z = 0) = \psi_0 \exp(-(x^2 + y^2)/w^2)$, we can insert this initial condition into equation (4) and directly integrate to obtain [3, 4]:

$$\psi(x, y, z)$$

$$= \psi_0 \frac{\exp[i \operatorname{atan}(z/z_0)]}{\left[1 + \left(\frac{z}{z_0}\right)^2\right]} \exp\left[-\frac{x^2 + y^2}{w^2\left(1 + \left(\frac{z}{z_0}\right)^2\right)}\right] \exp\left[-\frac{iz(x^2 + y^2)}{z_0 w^2\left(1 + \left(\frac{z}{z_0}\right)^2\right)}\right] \tag{5}$$

Where $z_0 = \pi n w^2 / \lambda_0$ is the Rayleigh range. We see that as a Gaussian beam evolves along $\hat{z}$, it decreases in intensity and spreads out. An example of equation (5) with $\psi_0 = 1$, $w = 0.5\ mm$, and $\lambda = 1\ \mu m$ is plotted in Fig. 2 at three different propagation distances.
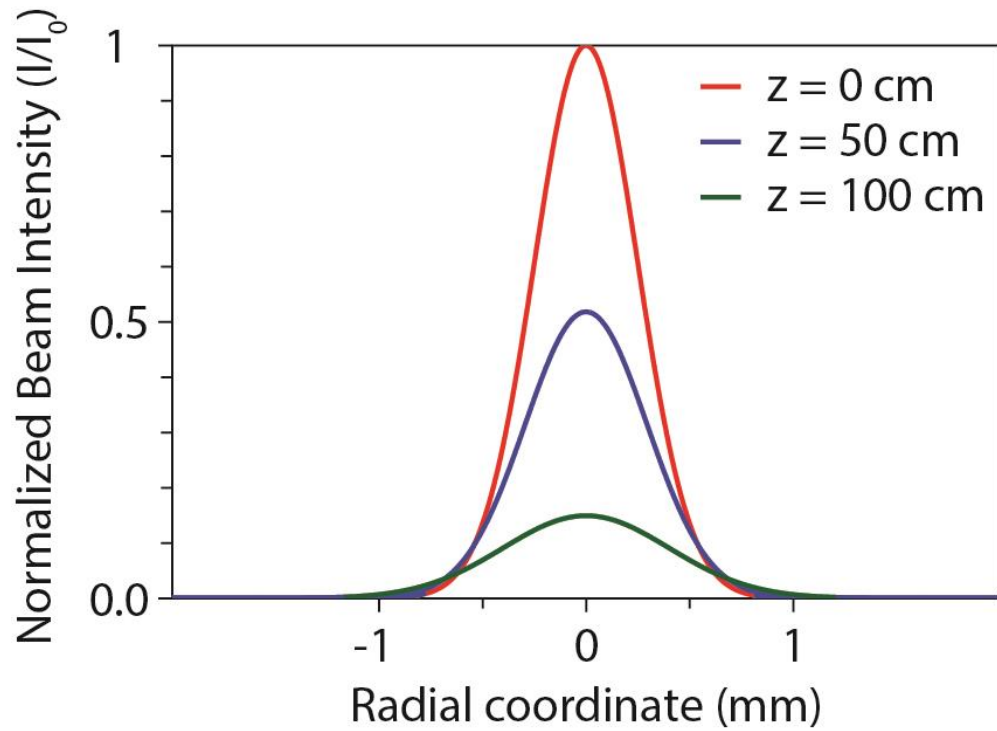
Figure 2| The intensity of a Gaussian beam suffering diffraction as it propagates. By half a meter of propagation, the beam has spread out and the peak intensity has diminished to approximately half its original value. Intensity values ($I \propto |\psi|^2$) are scaled to the peak of the beam at $z = 0$, I_0 .

1.2. Introduction to diffraction-free beams

The prospect of beams which defy the innate wavefront characteristic diffraction was first meme-named and investigated by Durnin and colleagues in 1987 [5, 6]. Since then, numerous wavefronts which seemingly resist the natural spread of light have been explored in detail [7-16]. The applications of these beams have appeared numerously in areas [17-19] ranging from micromanipulation [20-23] and data storage [24] to harmonic generation [25, 26], imaging [27, 28], electron beam creation [29], and microlithography [30]. In these subsections, the exotic properties of diffractionless beams are explored in detail.

1.2.1. The non-spreading property

As stated earlier, the plane wave, $\psi(x, y, z) = \psi_0 \exp\left(-i\left[k_x x + k_y y + k_z z\right]\right)$, is a solution to the Helmholtz equation, (1). This is equivalent to stating that these eigenfunctions pass through "unaffected" by the terms in the partial differential equation. If we look at the intensity of this plane wave solution, which is proportional to the absolute value squared of the electric field envelope, we find that the z-dependence vanishes as it only exists as a phase factor (i.e. $|\psi|^2 = \psi_0^2$). In other words, a plane wave is invariant along $\hat{z}$ and is arguably the simplest example of a non-spreading or diffractionless wavefront. This is in stark contrast to the evolution dynamics of a standard Gaussian beam whose intensity profile continuously reshapes as it propagates. There is a caveat, however, tied to this strange property: the power contained within an ideal diffraction-free beam is always infinite (e.g. the plane wave: $P_{beam} = \int |\psi_0|^2 dA = \infty$) [31]. This theoretical abstraction can be removed by apodizing the beam (to be discussed in a later section).

However, when discussing diffractionless beams, it is the Bessel beam [5, 6], not the plane wave, which has become the paragon. Consider the Helmholtz equation, equation (1), in a cylindrical coordinate system,

$$\frac{\partial^2 E(r,\theta,z)}{\partial r^2} + \frac{1}{r}\frac{\partial E(r,\theta,z)}{\partial r} + \frac{1}{r^2}\frac{\partial^2 E(r,\theta,z)}{\partial \theta^2} + \frac{\partial^2 E(r,\theta,z)}{\partial z^2} + k^2 E(r,\theta,z) = 0 \qquad (6)$$

Here, $r^2 = x^2 + y^2$ is the radial component and $\theta = \arctan(y/x)$ is the azimuthal component both of which are in the transverse plane. A diffractionless solution to this equation insists that any z-dependence appears only as a phase factor: $E(r,\theta,z) = R(r)\exp(in\theta)\exp(i\beta z)$. In this expression β is the propagation constant of the beam and n is an integer. Substitution of this ansatz into equation (6) results in Bessel's differential equation for the radial function:

$$r^2 \frac{\partial^2 R(r)}{\partial r^2} + r\frac{\partial R(r)}{\partial r} + [(k^2 - \beta^2)r^2 - n^2]R(r) = 0 \qquad (7)$$

Being a second order ordinary differential equation, two solutions exist: the Bessel functions of the first, J_n, and second, Y_n, kinds. The linear combination of these two solutions, $R(r) = A_0 J_n(\alpha r) + B_0 Y_n(\alpha r)$, can be reduced to include the former term only, $R(r) = A_0 J_n(\alpha r)$, due to the singularity that Y_n has at $r = 0$ (in these expressions, $\alpha^2 = k^2 - \beta^2$). Thus, we have the full solution to the Helmholtz equation in cylindrical coordinates:

$$E(r,\theta,z) = A_0 J_n(\alpha r)\exp(in\theta)\exp(i\beta z) \qquad (8)$$

These are the Bessel beams. Note immediately, that the intensity of this beam, $I \propto A_0^2 J_n^2(\alpha r)$, remains invariant upon propagation, and because J_n does not asymptotically approach zero for any order, n, carries infinite power. Fig. 3 displays the intensity profiles of several orders of Bessel beams in the transverse plane.
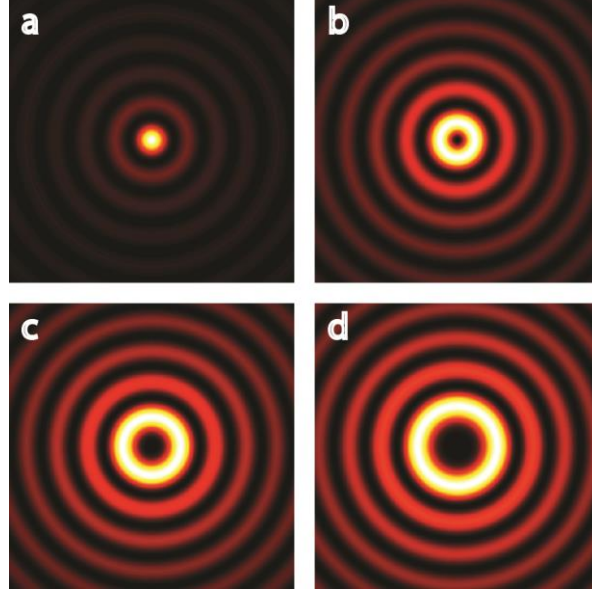
Figure 3| Transverse intensity profiles of diffractionless Bessel beams. a) $n = 0$, b) $n = 1$, c) $n = 2$, d) $n = 3$.

1.2.2. Conical superposition

Up until this point, we have presented two propagation invariant entities, the plane wave and the Bessel beam. Both were solutions to the Helmholtz equation in a (2+1)D space meaning two transverse dimensions, $\hat{x}$ and $\hat{y}$, and one propagation direction, $\hat{z}$. In this subsection, it will be shown that in fact an infinite amount of diffractionless (2+1)D wavefronts are possible. To begin, we start with the paraxial wave equation in Cartesian coordinates with two transverse spatial dimensions:

$$i\frac{\partial \psi(x,y,z)}{\partial z} + \frac{1}{2k}\left[\frac{\partial^2 \psi(x,y,z)}{\partial x^2} + \frac{\partial^2 \psi(x,y,z)}{\partial y^2}\right] = 0. \tag{9}$$

As before, we immediately recognize the plane wave, $\psi(x,y,z) = \psi_0 \exp\left[-i\left(k_x x + k_y y + k_z z\right)\right]$, as a solution. Differently from the Helmholtz solution, we recongize that $k_z = \left(k_x^2 + k_y^2\right)/2k = \gamma^2/2k$ which arises because of the paraxial approximation. However notice that these particular four plane waves are also a solution to equation (2),

$$\psi(x,y,z) = \left[\frac{\exp\left(i\frac{\gamma x}{\sqrt{2}}\right) + \exp\left(-i\frac{\gamma x}{\sqrt{2}}\right)}{2} + \frac{\exp\left(i\frac{\gamma y}{\sqrt{2}}\right) + \exp\left(-i\frac{\gamma y}{\sqrt{2}}\right)}{2} \right] \exp\left(-i\frac{\gamma^2}{2k}z\right). \qquad (10)$$

Let us look at equation (10) in some detail. The key feature which enables this expression to satisfy equation (9) is that each of the four plane wave components shares the same z dependent phase, $\exp[-i\gamma^2 z/2k]$. This is to say that in k-space, each wavefront has the same value of k_z. Furthermore, each individual wavefront has the same total k vector magnitude, $|k|$. Qualitatively, note that in the first two terms, the transverse $\vec{k}$ vector component is only travelling in the positive or negative $\hat{x}$ direction respectively, and in the last two terms, only the positive or negative $\hat{y}$ direction respectively. By plotting these $\vec{k}$-vectors we see that the four plane waves trace out a square in $\vec{k}$-space (Fig. 4a), and the resulting real-space transverse intensity profile, $|\psi|^2$, is a grid-like pattern that is indeed propagation invariant (Fig. 4b).
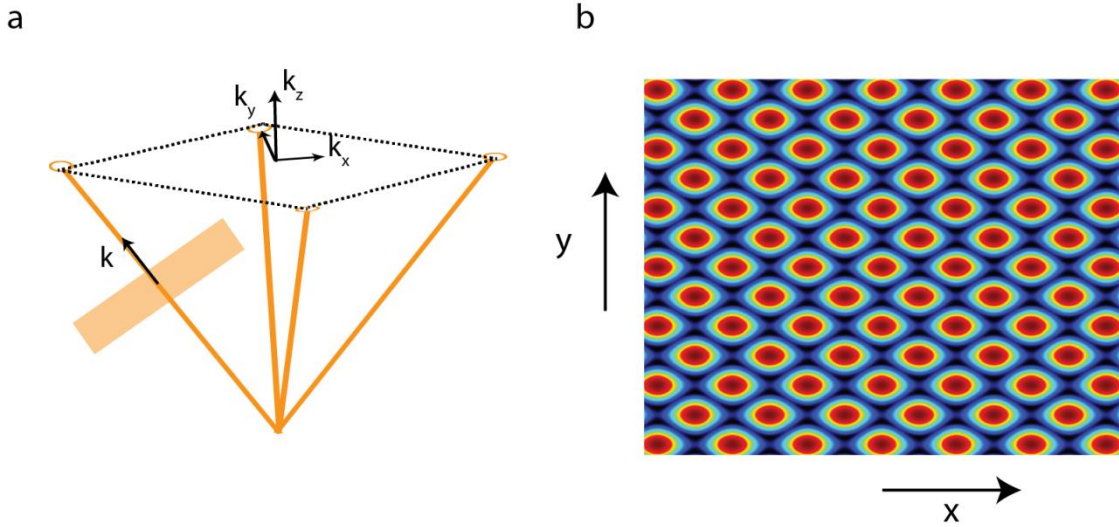
Figure 4| The solution given by equation (10) has four plane waves with equal values of $\boldsymbol{k_z}$ and $|\boldsymbol{k}|$. (a) This traces out a square in $\boldsymbol{k}$-space. (b) The resulting transverse intensity pattern is diffractionless.

Interestingly, if the stipulations on k_z and $|k|$ are adhered to, one can generalize the plane wave solution so that any wavefront emanating in an arbitrary azimuthal direction, θ, will also satisfy equation (9):

$$\psi(x,y,z) = \exp[i\gamma(x\cos\theta + y\sin\theta)]\exp\left(-i\frac{\gamma^2}{2k}z\right). \tag{11}$$

Because each and every choice of θ on $[0, 2\pi]$ gives rise to a valid solution, we can conclude that the most general diffraction-free solution comprised of angled plane waves in $\vec{k}$-space is given by:

$$\psi(x,y,z) = \int_0^{2\pi} G(\theta)\exp[i\gamma'(x\cos\theta + y\sin\theta)]\exp\left(-i\frac{\gamma^2}{2k}z\right)d\theta. \tag{12}$$

Where $G(\theta)$ is a "spectrum" function specifying which plane waves will compose the diffractionless solution and γ' is an normalized coefficient that adjusts according to the amount of plane waves superimposed (for a single plane wave, $\gamma' = \gamma$). Analogous to the k-space square that was traced out by the four plane waves in Fig. 4a, the general solution presented in equation (12) accounts for all the plane waves emitted from a common point at different angles, θ, which forms a cone in k-space (Fig. 5). This is origin of the term "conical superposition of plane waves".
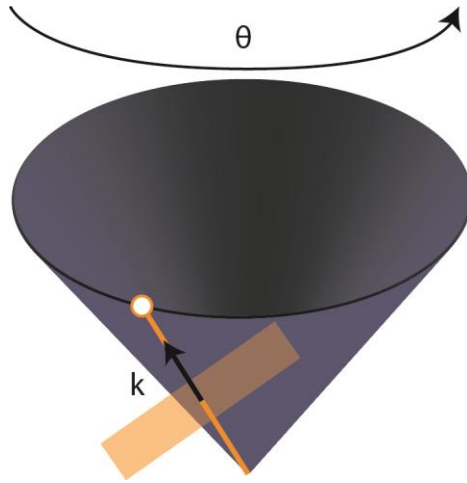
Figure 5| Propagation invariant plan wave solutions of the form seen in equation (12) emanate from a common point and form a cone in $\vec{k}$-space

Excitingly, for every unique $G(\theta)$, a new diffractionless beam emerges; thus, conical superposition generates a seemingly infinite amount of diffractionless beams. Notice in the special case of $G(\theta) = 1/2\sum_{i=0}^{3}\delta(\theta - i\pi/2)$ and $\gamma' = \gamma/\sqrt{2}$ we recover the solution given by equation (10).

One immediate and interesting prospect is to find out what happens when we approach $G(\theta) = 1$; that is, when we superimpose every possible conical plane wave together. A clever and surprisingly aesthetic way to investigate this is to pick plane waves in such a way that regular polygons are traced out on the base of the k-space cone. Then, by increasing the order of the regular polygon, the full conical superposition is eventually delineated. Fig. 6 conically superimposes several regular polygons having $N = 3, 5, 8, 12$, and 100 sides and displays each resulting transverse intensity profile. In the $N = 3$ case, a crystal-like optical pattern akin to a Bravais lattice forms (Fig. 6a). A pentagon of plane waves, $N = 5$, results in a transverse pattern akin to a quasi-crystal Penrose lattice (Fig. 6b). More complicated patterns emerge as the number of sides increases (Fig. 6c and Fig. 6d). Remarkably, however, we find that as the amount of sides approaches infinity, that is, a spectrum of $G(\theta) = 1$, the zero order Bessel beam emerges (Fig. 6e). A rigorous treatment would indeed show that the Bessel beam is representable by the full superposition of all conical plane waves.
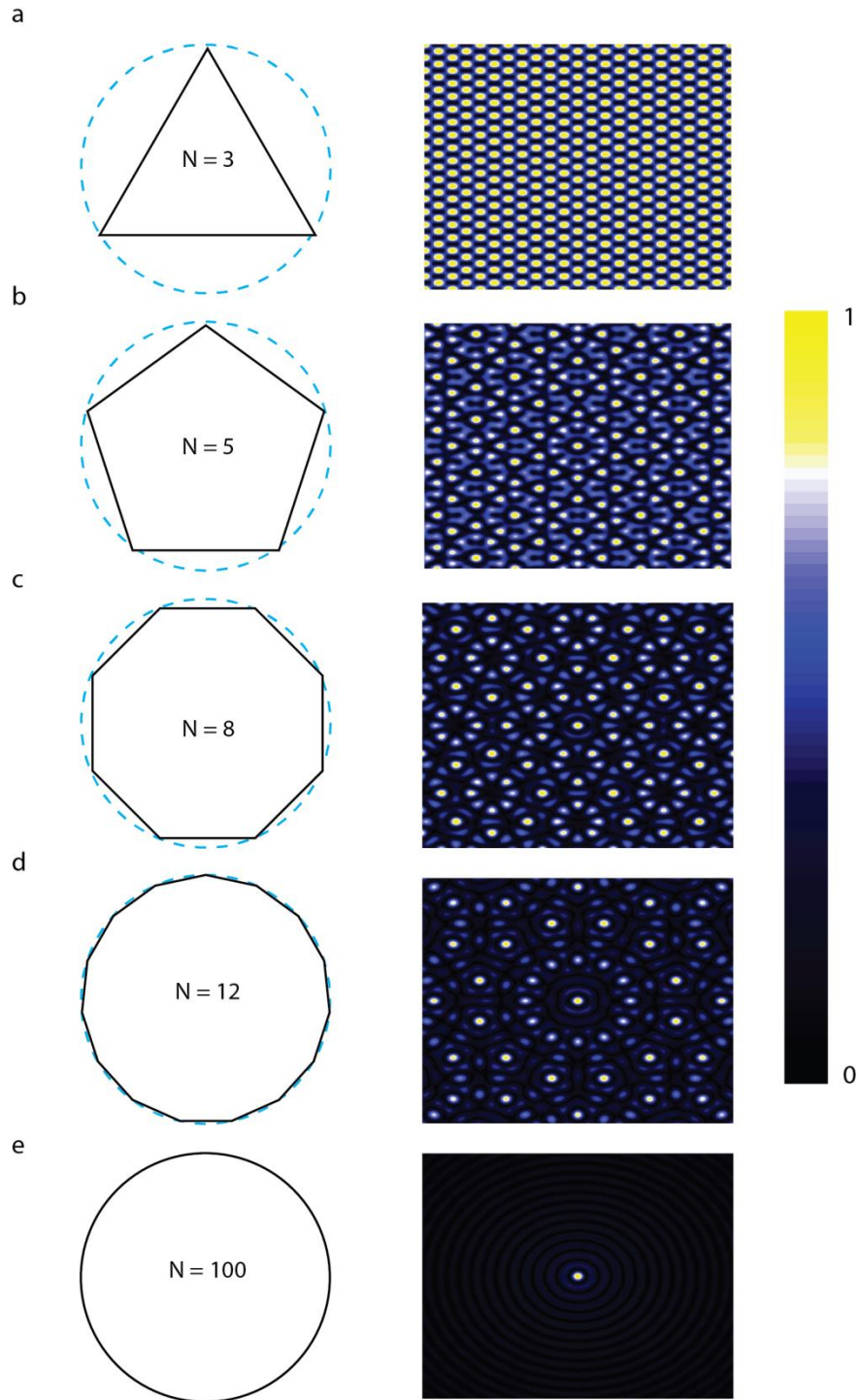
Figure 6| Inscribing regular polygons via conical superposition. For each polygon, the resulting propagation invariant transverse intensity profile is plotted with the maximum of the pattern scaled to unity. a) An inscribed triangle produces a crystal pattern; b) An inscribed pentagon forms a quasi-crystal arrangement; c) An inscribed octagon crystal pattern; d) An inscribed dodecagon quasi-crystal showing complex patterns; e) An inscribed 100 sided regular polygon approximates the $G(\theta) = 1$ case and approaches a zero order Bessel beam.

12

1.2.3. Self-healing property

Shockingly, propagation invariant beams tend to reconfigure themselves back into their ideal electric field arrangements even after appreciable adulterations. This property of self-healing [32] is a direct result of Babinet's principle of diffraction [33]. The rule states that any object's far-field diffraction pattern can be decomposed as a sum of parts. To clarify this, consider the two examples given in Fig. 7. If we wanted to compute what the electric field distribution would look like in the far-field for coherent light passing through the house-shaped aperture seen in Fig. 7a, we could so by calculating the propagation of light for the rectangular base and the triangular top independently and then sum the two results together. The power of the method becomes clearer in configurations like that of Fig. 7b where complicated apertures suddenly become simple to evaluate.
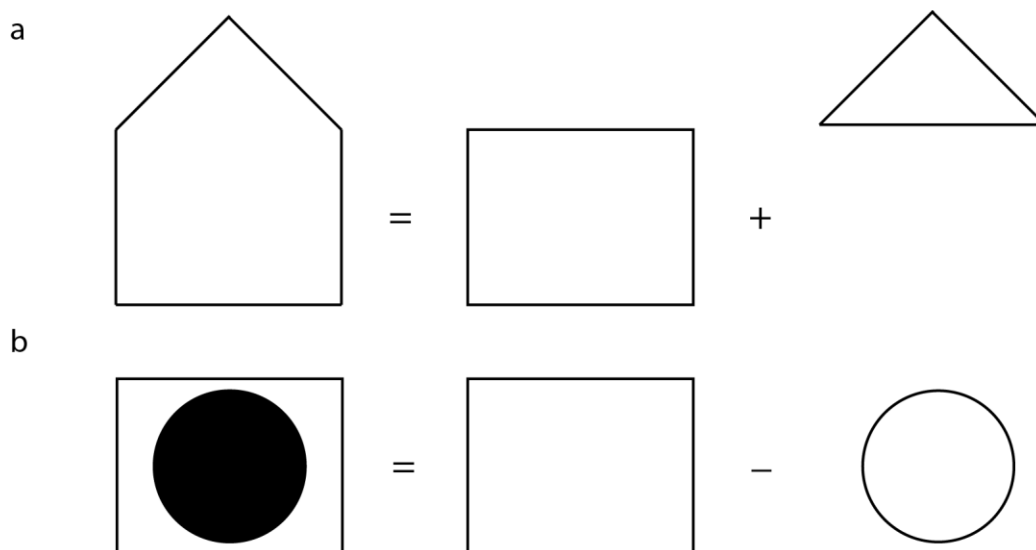
Figure 7| Babinet's principle states that the far-field electric field distribution can be decomposed into parts. (a) A house-shaped aperture can be split into two additive components. (b) A square window with a circular opaque object can be computed via subtraction.

Consider now an initial Bessel beam, $\psi_{Bess}(x, y, z = 0)$, which collides with some obstructing object before it propagates. If the object has an initial "negative" distribution, $\psi_{obj}(x, y, z = 0)$, then the

far-field diffraction pattern of the obstructed Bessel beam, $\psi_{Total}(x,y,z)$, can be found using Babinet's principle; that is, $\psi_{Total}(x,y,z) = \psi_{Bess}(x,y,z) - \psi_{obj}(x,y,z)$. Temporarily dropping the notation where the independent variables are written, the resulting intensity of this wavefront would be given by:

$|\psi_{Total}|^2 = |\psi_{Bess}|^2 + |\psi_{obj}|^2 - \psi_{Bess}\psi_{obj}^* - \psi_{Bess}^*\psi_{obj}$. Any linear far-field electric field pattern can be computed via the Fresnel diffraction integral [1]:

$$\psi(x,y,z) =$$

$$\frac{\exp(ikz)}{i\lambda z} \int_{-\infty}^{\infty} \int_{\infty}^{\infty} \psi_{Bess}(x,y,z=0) \exp\left[\frac{ik}{2z}((x-x')^2 + (y-y')^2)\right] dx' dy'. \tag{13}$$

As we know, ψ_{Bess} is a propagation invariant so $\psi_{Bess}(x,y,z=0) = \psi_{Bess}(x,y,z)$ for all z, and therefore one knows the far-field pattern. The opaque object on the other hand, $\psi_{obj}(x,y,z)$ will have a pattern which evolves according to equation (13). Looking closely at this expression, we see that the electric field envelope, $\psi_{obj}(x,y,z)$, will decrease in proportion to z^{-1} throughout its propagation. This means that as $z \to \infty$, only the complex envelope of the Bessel beam will remain intact; In other words, $\psi_{obj}(x,y,z)$ approaches zero everywhere. Hence, we find the total intensity at large propagation distances to be $|\psi_{Total}|^2 = |\psi_{Bess}|^2$. The effects of the obstruction have vanished, and the diffractionless beam has "healed itself".

This property is illustrated in Fig. 8 where both a whole and partially blocked Bessel beam ($\lambda_0 = 532\ nm$) are simulated each using a main lobe size of $x_0 = 200\ \mu m$. In both cases, the beam is finite so some diffraction results. Fig. 8a and 8b shows an initial cross section of an unobstructed Bessel beam and the propagation that results (Fig. 8b). In this case, we see the expected invariant propagation along the z direction. Yet, as we have shown, even if such a beam is obfuscated initially (Fig. 8c), it eventually reforms into its diffractionless shape (Fig. 8d).
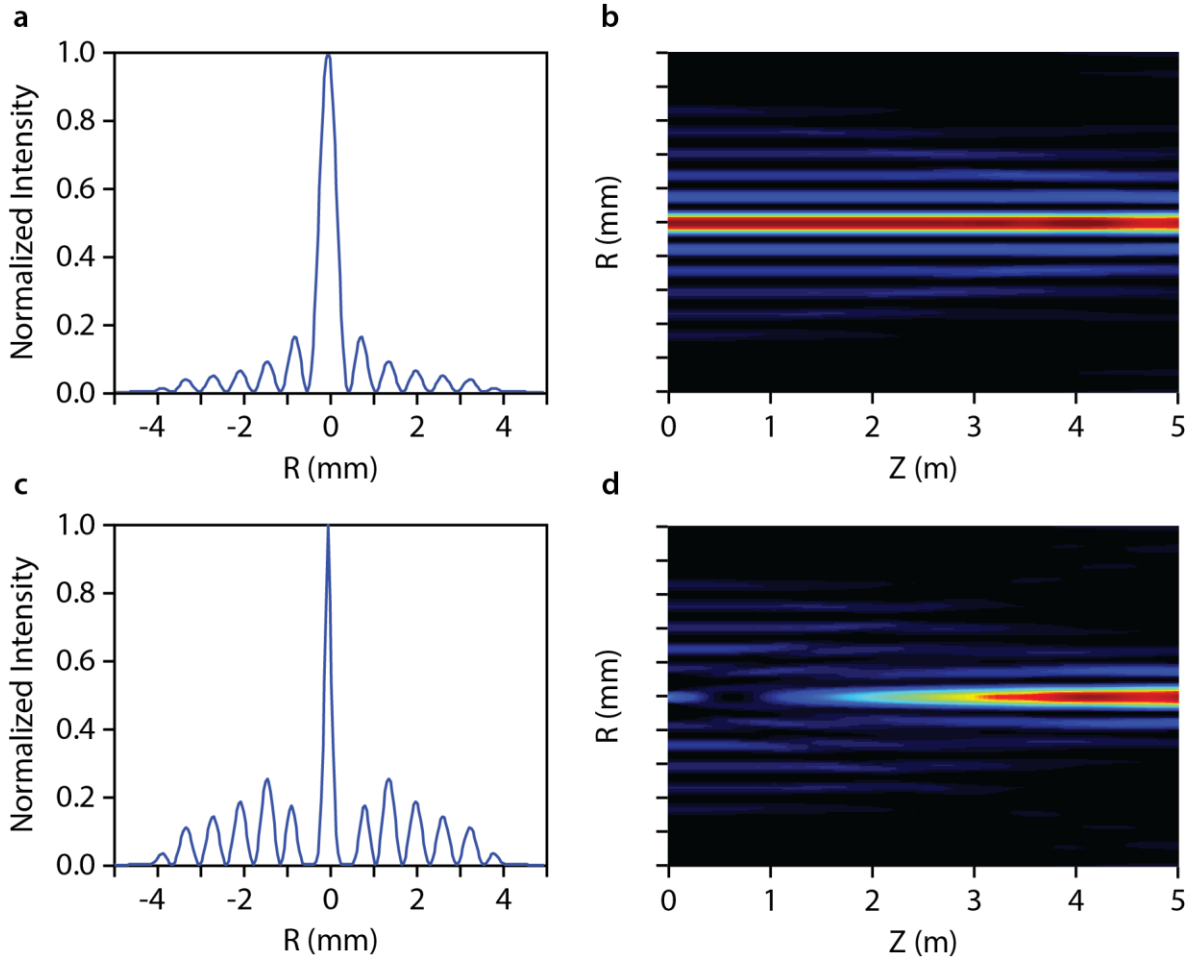
Figure 8| The self-healing property is illustrated with a finite Bessel beam. An unobstructed Bessel beam, (a), propagates in a quasi-diffractionless manner, (b). If a section of the wavefront is removed, (c), the obstructed Bessel beam heals itself after several diffraction lengths, (d).

15

1.2.4. Apodization

In practice, all beam profiles must be finite is both energy and extent. Because of this, the ideal wavefronts discussed in the previous sections must be truncated so that they contain a finite amount of power – this is known as apodization. As a result, these beam profiles begin to compromise their diffractionless and self-healing property. It is important to note, however, that the quasi-diffractionless beams which result still out perform their standard counterpart when it comes the discussed qualities [34].

Consider a standard example, apodizing a zero order Bessel beam with a Gaussian enclosure, $E(r, \theta) = A_0 J_n(\alpha r) \exp(-r^2/w^2)$. We showed earlier that the unapodized version carries infinite power and is an eigenfucntion solution to the Helmholtz equation under radially symmetric conditions. In this new case, however, the beam if finite in power and evolves in the z direction [35].

$$\psi(x, y, z) = -\frac{ikA_0}{2zQ} \exp\left[ik\left(z + \frac{r^2}{2z}\right)\right] J_0\left(\frac{i\alpha kr}{2zQ}\right) \exp\left[-\frac{1}{4Q}\left(\alpha^2 + \frac{k^2 r^2}{z^2}\right)\right]. \tag{144}$$

Where $Q = w^{-2} - ik/2z$. Note that the pre-factor is proportional to z^{-1} indicating that the beam spreads. More interestingly, similar to the fact that a Bessel beam is comprised of a delta-ring of $\vec{k}$-vectors (as uncovered in section 1.2.2), a Gaussian apodized Bessel beam is a thick ring in $\vec{k}$-space with a Gaussian profile in the $\vec{k}$-radial direction (Fig. 9).
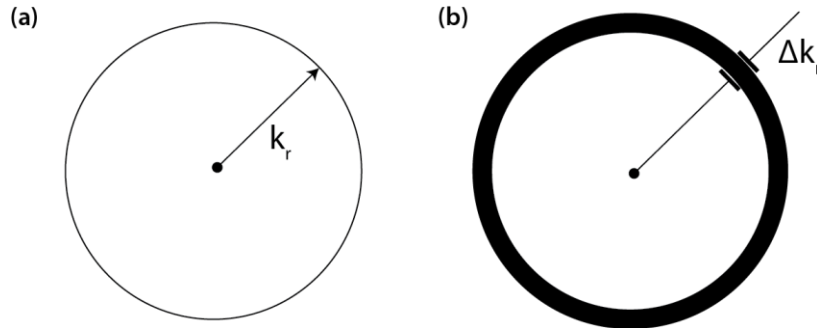
Figure 9| (a) An unapodized Bessel beam is formed from a delta-ring of $\vec{k}$-vectors. (b) Apodizing this beam with a Gaussian profile thickens the ring so that it includes $\vec{k}$ vectors in a range of values, $\mathbf{\Delta k_r}$.

1.3. Airy Beams

The idea that light travels in straight lines has been deeply ingrained in human consciousness since antiquity. This concept was first postulated by Euclid in his Optica and was one of the pillars of Newton's corpuscular hypothesis. Even with the advent of wave theories and Maxwell's electrodynamics, this very basic premise persisted as a direct outcome of electromagnetic momentum conservation. Because of this, one always is keen to expect that the intensity centroid of an optical beam should always follow a straight line; however, this law does not in any way restrict how the intensity features of an optical wavefront should behave during propagation. This latent aspect opens up an intriguing question: is it feasible to produce an optical beam whose intensity peaks move along curved trajectories?

In 2007, Siviloglou and Christodoulides introduced and subsequently observed the Airy beam, an optical wavefront whose intensity features follow a curved trajectory [11, 36, 37]. The simplest Airy beam can be obtained from a normalized (1+1)D paraxial wave equation:

$$i \frac{\partial \psi(x,z)}{\partial z} + \frac{1}{2k} \frac{\partial^2 \psi(x,z)}{\partial x} = 0. \tag{15}$$

Where, as before, the normalized coordinates are given by $x = \tilde{x}/x_0$ and $z = \tilde{z}/z_0 = \tilde{z}/2kx_0^2$. The initial condition, $\psi(x, z = 0) = Ai(x) \exp(ax)$ results in the following solution,

$$\psi(x,z) = Ai\left(x - \frac{z^2}{4} + iaz\right) \exp\left[ax - \frac{az^2}{2} - i\left(\frac{z^3}{12} - \frac{a^2z^2}{2} - \frac{xz}{2}\right)\right]. \tag{16}$$

This solution not only carries the same intriguing properties akin to the other diffractionless members [11, 38], but brings along some new features. For example, one can show that this is the *only* one dimensional diffraction free solution and that the main intensity peak follows a parabolic trajectory [38, 39]. This ballistic nature occurs even in the absence of external forces as it is an intrinsic characteristic of the wavefront [40]. Fig. 10 illustrates the propagation dynamics of this unique wavefront for $\lambda = 500\,nm$, $x_0 = 100\,\mu m$, $z_0 = 12\,cm$, and several different attenuation coefficients, $a =$

$\{.01, .05, .10\}$. For these parameters, the FWHM of the main airy lobe is about $171\,\mu m$ and remains quasi-diffractionless for approximately 10, 8, and 6 diffraction lengths respectively.
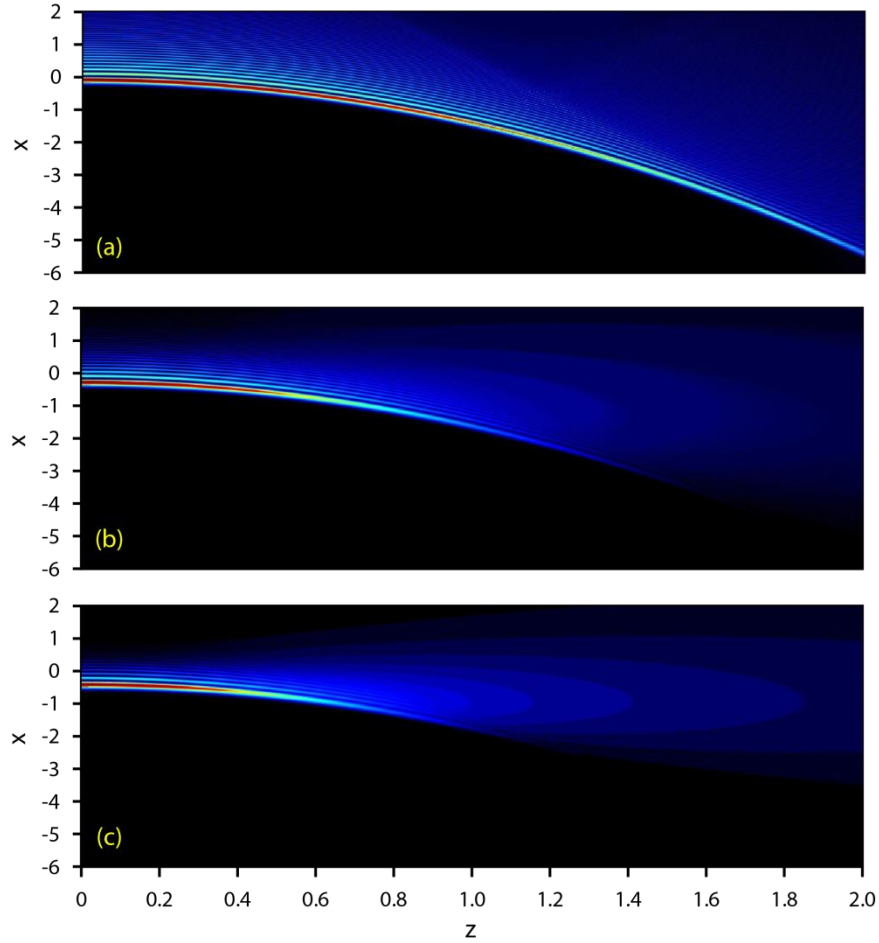
Figure 10| Propagation of a finite Airy beam with various attenuation coefficients. (a) a = .01, (b) a = .05, and (c) a = .10. The main airy lobe remains approximately diffractionless for 6, 8, and 10 diffraction lengths respectively.

Because the paraxial wave equation can be sequestered via the method of separation of variables, and the Airy beam is a (1+1)D solution, higher dimension Airy waves are possible [36, 41]. Consider the (2+1)D paraxial wave equation. Airy beam solutions can be constructed as the product of two orthogonal (1+1)D versions:

$$\psi(x,y,z) = \prod_{p=x,y} Ai\left(p - \frac{z^2}{4} + ia_p z\right) \exp\left[a_p p - \frac{a_p z^2}{2} - i\left(\frac{z^3}{12} - \frac{a_p^2 z^2}{2} - \frac{pz}{2}\right)\right]. \qquad (17)$$

Utilizing the same parameters as in Fig. 10 and having the attenuation coefficients be the same in both directions $a_x = a_y = .05$, Fig. 11 illustrates the propagation dynamics of the (2+1)D Airy beam at three different propagation distances.
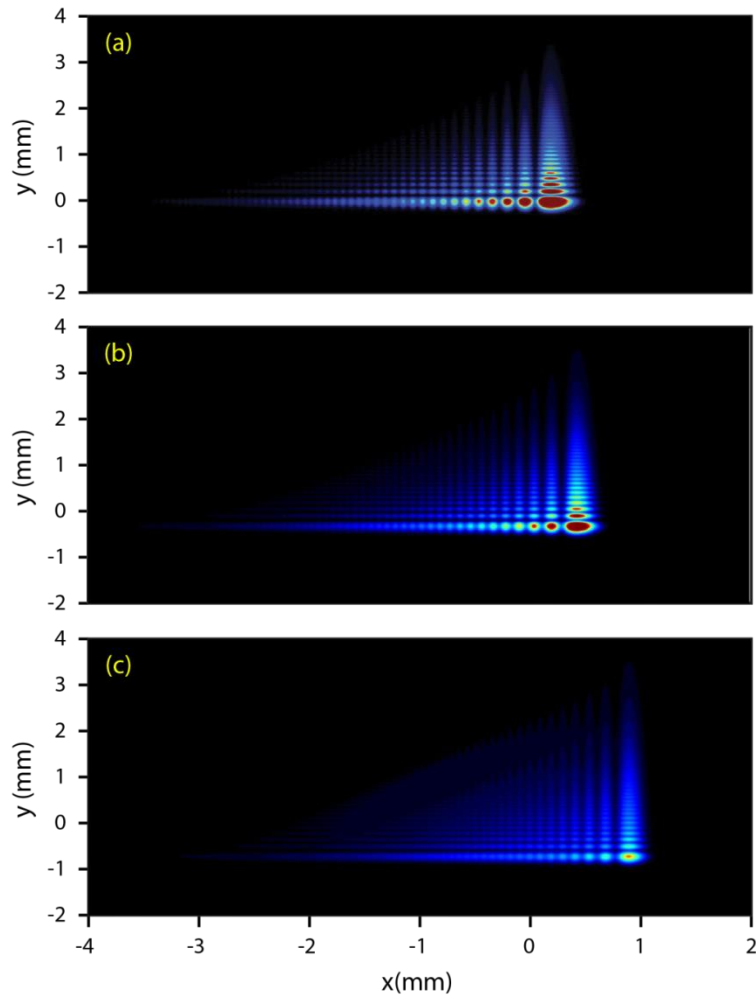
Figure 11| Propagation of a two dimensional finite Airy beam at various propagation distances. (a) z = 0 cm, (b) z = 55 cm, and (c) z = 75 cm.

1.3.1. Autofocusing beams

One of the most important characteristics of optical beams is their focusing dynamics in free space; that is, how they collapse under linear conditions. A wavefront will either focus or defocus depending on its initial phase and amplitude distribution. For example, a standard Gaussian wavefront has a complex electric field envelope given by equation (5). The peak intensity of such a beam follows a Lorentzian distribution – a gently rising and falling function.

In applications such as corneal refractive surgery [42] or optical filamentation [43], a beam which instead suddenly spikes in intensity and then subsides can be more desirable. A radially symmetric arrangement of Airy beams in free space is a good candidate to meet these criteria [44].

$$\psi(r,z) = \psi(r,z) = \psi Ai(r_0 - r) \exp[a(r_0 - r)] \qquad (18)$$

Here, $r^2 = x^2 + y^2$ and r_0 is the initial radial displacement of the main ring. Note that for $|r| < r_0$ equation (18) decays quickly and for $|r| > r_0$ the slowly decaying Airy oscillations occur. To give an example, consider a case where $\lambda = 1 \ \mu m \ r_0 = 1 \ mm$ and $a = .05 \ mm^{-1}$ (Fig. 12).
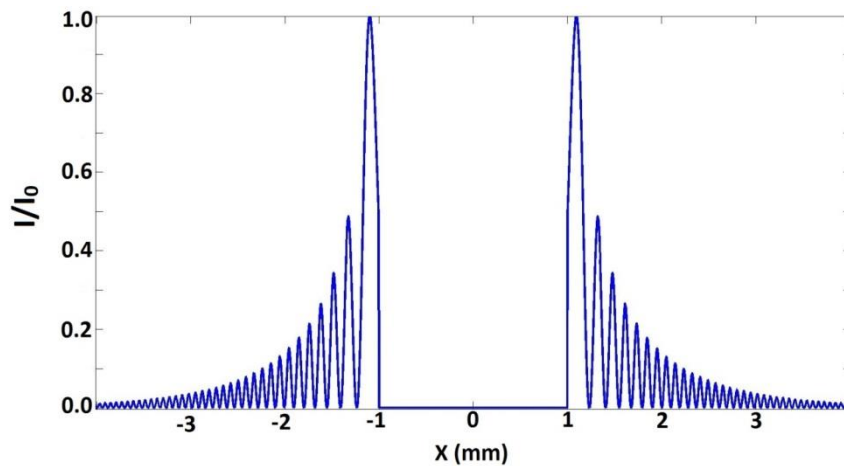
Figure 12| Initial intensity distribution of equation (18) along Y=0 for $r_0 = 1 \ cm$ and $a = .05 \ mm^{-1}$. Values are scaled to an initial peak value of unity.

The complex electric field shown in Fig. 12 will evolve according to the same Fresnel diffraction integral that was introduced earlier, equation (3); however, this integral can be simplified because of equation (18)'s azimuthal symmetry. The simplified integral given in cylindrical coordinates is:

$$\psi(r,z) = \frac{1}{2\pi} \int_0^\infty \tilde{\psi}(k_r, z = 0) k_r J_0(k_r r) \exp\left[-\frac{ik^2 z}{2}\right] dk_r \tag{19}$$

Where $\tilde{\psi}(k_r, z = 0)$ is the Hankel transform of equation (19) at $z = 0$.

$$\tilde{\psi}(k_r, z = 0) = 2\pi \int_0^\infty \psi(r, z = 0) J_0(k_r r) r \, dr \tag{20}$$

A numerical computation of $\psi(r,z)$ is found using a beam propagation method and a cross section of the results is displayed in Fig. 13. The following properties are apparent: The on-axis intensity of the wavefront abruptly reaches a value that is 120 times the initial peak intensity. Two, after coming to this sudden focus, the peak intensity drops off rapidly. Three, in the far field, the diffraction pattern approximately forms a finite first order Bessel beam [22].

The autofocusing Airy profile can be generalized to include an entire family of abruptly autofocusing waves. These beams can be understood via the concept of caustics and careful manipulation of their sub linear chirps allows for one to pre-engineer a wavefront resulting in customizable autofocusing characteristics [45].
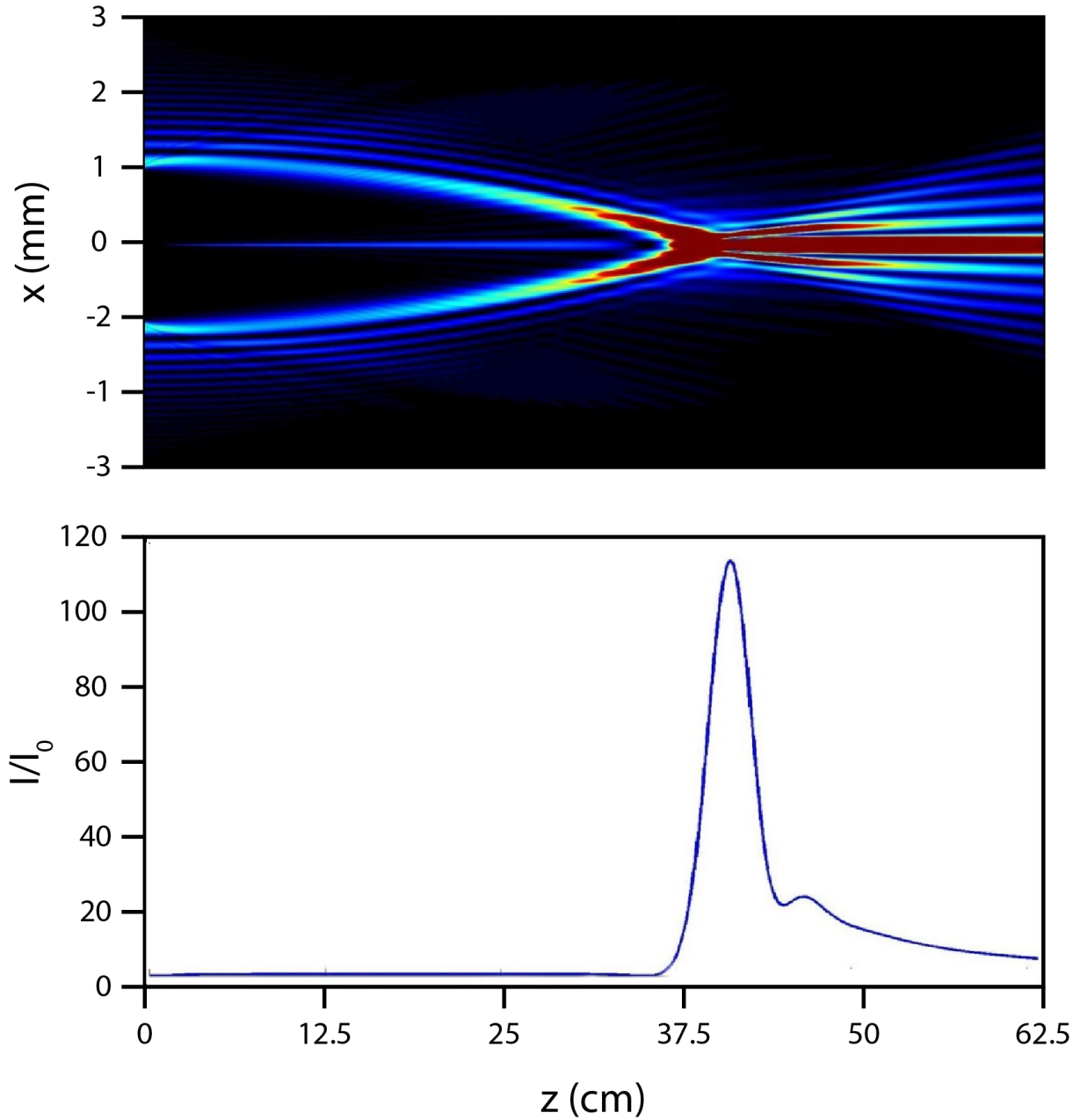
Figure 13| (a) Cross section along Y = 0 showing the propagation dynamics of the radial Airy distribution where $\lambda = 1\ \mu m$, $r_0 = 1\ mm$ and $a = .05\ mm^{-1}$. (b) On-axis intensity, $R = 0$, showing the abruptly focusing characteristic of this wavefront.

1.3.2. Non-paraxial accelerating beams

Although the Airy beam is indeed the only (1+1)D non-diffracting solution to the paraxial wave equation, there exist multiple solutions in the non-paraxial domain [14, 46-51]. This arises from the fact that the Helmholtz equation, which describes these wavefronts, has no preferred coordinate system [37]. The method to finding any new family of propagation invariant accelerating wavefronts is practically algorithmic. The first step is to convert the Helmholtz equation into a chosen coordinate system. Then, solutions whose intensity profiles are independent of z are saught; such solutions will consist of both forward and backward propagating waves. The final step is discarding the backwards propagating waves.

Consider our previous example when the Helmholtz equation is solved in cylindrical coordinates. The solutions are the Bessel beams, $\psi(r,z) = J_n(\alpha r)\exp(in\theta)\exp(i\beta z)$, which are indeed z independent. If we choose a high order of n, we would expect a ring pattern where the first main lobe occurs at the first maximum of $J_n(\alpha r)$. If we then cleave the backward propropagating wave, we obtain the non-paraxial half-Bessel beam (Fig. 14a). Several other examples can be seen in Fig. 14b-d.
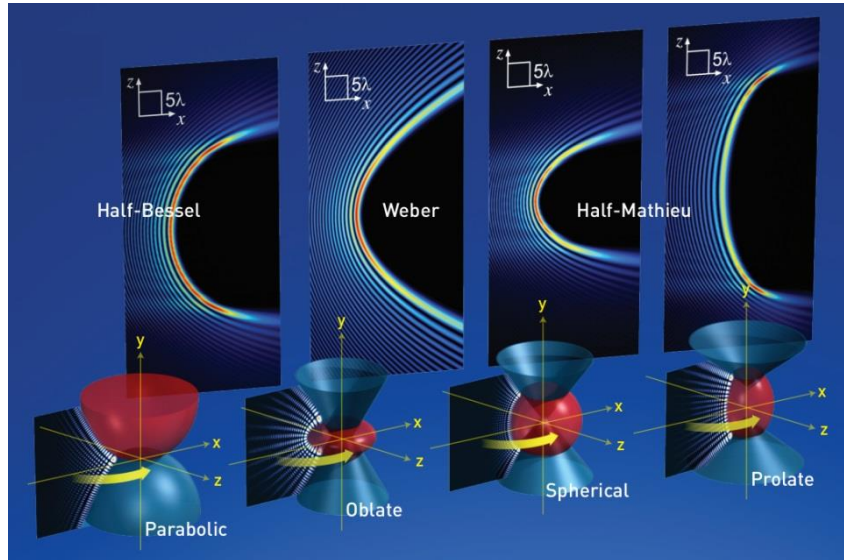
Figure 14| (a) Cross section along Y = 0 showing the propagation dynamics of the radial Airy distribution where $\lambda = 1\ \mu m$, $r_0 = 1\ mm$ and $a = .05\ mm^{-1}$. (b) On-axis intensity, $R = 0$, showing the abruptly focusing characteristic of this wavefront.

CHAPTER TWO: LOCALIZED WAVES WITH HYDROGEN-LIKE SYMMETRIES

In the spatiotemporal domain, the prospect for localized waves that can simultaneously negotiate both dispersion and diffraction effects in the bulk has been actively pursued by several research groups in both the linear and nonlinear regimes [52-54]. In general, an optical wave packet propagating in a homogeneous dielectric medium will expand because of diffraction effects while at the same time its temporal profile will broaden because of dispersion. In the linear domain, specific wave solutions are known to exist under normally and anomalously dispersive conditions. For normal dispersion, these solutions exhibit an X-wave structure [55, 56] — a direct outcome of the bi-dispersive nature of the underlying wave equation [8]. In the anomalous domain, spherical O-waves [13, 54] are allowed and Bessel-X pulses are possible under specific conditions [57]; however, this constraint on the sign of dispersion can be relaxed either under non-paraxial conditions or when the velocity of the localized wave is largely different from the medium's linear group velocity. In fact, not only has it been shown that a crossover from X- to O-waves can occur in a dispersive medium, but localized waves that fit neither category are also possible [58, 59]. Recently, three-dimensional (3D) Airy-Bessel bullets that are impervious to both dispersion and diffraction have been suggested [11] and successfully demonstrated in dispersive media [15]. This versatile class of optical wave packets was made possible by exploiting the fact that non-spreading Airy waves can exist even in one dimension (1D). This class of Airy-Bessel bullets is possible irrespective of the dispersion properties of the material itself. The quest for such spatio-temporal entities is clearly intertwined with experimental capabilities of simultaneously shaping their $\vec{k}$-ω spectra. Over the years, various techniques have been developed to address these needs in both the spatial and temporal domain [55-57, 60, 61]. Lately, methods which allow for the generation of quasi-nondiffracting light beams with complex transverse shapes have been demonstrated [61, 62]. Further progress in this area may pave the way towards the generation of other exotic space-time bullets with unique properties tailored for particular light-matter interaction processes [63].

In this section, we present a novel class of linear optical bullets that is possible under anomalously dispersive conditions. Depending on their angular momentum numbers, these wavepackets exhibit angular symmetries akin to those encountered in the quantum mechanical wavefunctions of a hydrogen atom. The dynamics of such states when they are apodized is analytically studied along with their associated energy flows. Other types of linear optical bullets generated through a spherical superposition from Archimedean and Platonic solids in $\vec{k} - \omega$ space are also investigated in this work. The possibility of spinning bullets is considered and the prospect for their realization is discussed.

2.1. Problem formulation and analysis

In general, the primary electric field associated with a wavepacket can be expressed through a slowly varying envelope via $\vec{E}(\vec{r}, t) = \vec{u}\psi(\vec{r}, t) \exp[i(k_0 z - \omega_0 t)]$, where ω_0 is the carrier angular frequency, $k_0 = \omega_0 n(\omega_0)/c$, is the wavenumber evaluated at ω_0, and $n(\omega_0)$ is the refractive index. The spatio-temporal evolution of the envelope, $\psi(\vec{r}, t)$, under the combined action of diffraction and group velocity dispersion is known to obey the following evolution equation:

$$i\frac{\partial \psi}{\partial z} + \frac{1}{2k}\left(\frac{\partial^2 \psi}{\partial x^2} + \frac{\partial^2 \psi}{\partial y^2}\right) - \frac{k_2}{2}\frac{\partial^2 \psi}{\partial \tau^2} = 0, \tag{21}$$

where in equation (21), $\tau = t - z/v_g$ is a time coordinate frame moving at the wave's group speed, v_g, and $k_2 = \partial^2 k/\partial \omega^2$ represents the dispersive coefficient of the homogeneous medium again evaluated at ω_0. The material is anomalously dispersive if $k_2 < 0$ and is normally if $k_2 > 0$. The transverse spatial operators in equation (21) account for diffraction effects while the temporal operator for the action of dispersion. Equation (21) can be judiciously scaled by normalizing the independent variables involved in such a way that the diffraction length $L_{diff} = 2kd^2$ is equal to the corresponding dispersion length $L_{disp} = \tau_0^2/|k_2|$, i.e., $L_{diff} = L_{disp}$. Here, d is an arbitrary length scale and τ_0 is associated with the pulsewidth of the wavepacket. From this point on, the material dispersion is taken to be anomalous in our analysis. Under these transformations and assumptions, equation (21) takes the form:

$$i\frac{\partial \psi}{\partial Z} + \frac{\partial^2 \psi}{\partial X^2} + \frac{\partial^2 \psi}{\partial Y^2} + \frac{\partial^2 \psi}{\partial T^2} = 0. \tag{22}$$

Here in equation (22) we have employed the following set of normalized coordinates and variables $X = x/d$, $Y = y/d$, $Z = z/(2kd^2)$, and $T = \tau/\tau_0$. The aforementioned spatio-temporal wavepackets can be studied experimentally in anomalously dispersive bulk media such as silica glass. Silica, at $\lambda_0 = 1550 \, nm$, exhibits a dispersive coefficient of $k_2 = -2.8 \times 10^{-2} \, ps^2/m$. For this example, a dispersion-diffraction equalization ($L_{diff} = L_{disp} = 5.7 \, cm$) is possible provided that the

wavepacket generated from a transform-limited femtosecond laser has the following parameters: $\tau_0 = 40\,fs$ and $d = 100\,\mu m$.

In what follows, we will derive the electromagnetic equations describing the internal power flow associated with a spatio-temporal wavepacket as a result of dispersion and diffraction. This is necessary in order to comprehend the underlying dynamics in such systems. With this in mind, we employ a perturbative approach, valid within the slowly varying envelope approximation and paraxial diffraction optics. We start our analysis by writing the electric field as a superposition of plane waves centered around a carrier frequency, ω_0. Without any loss of generality, the primary electric field component is taken here to be $\hat{x}$ polarized. In this case:

$$\vec{E} = \hat{x}\iiint F_0(\omega - \omega_0; k_x, k_y) \times \exp\left[i(\vec{k}\cdot\vec{r} - \omega t)\right] d\omega dk_x dk_y \qquad (23)$$

This same field can also be expressed in terms of a slowly varying envelope ψ, i.e $\vec{E}(\vec{r}, t) = \hat{x}\psi(\vec{r}, t)\exp\left(i(k_0 z - \omega_0 t)\right)$. Given that $k_z \approx k - (k_x^2 + k_y^2)/(2k)$ and that the wavenumber can be expanded in a Taylor series around ω_0, $k \approx k_0 + k_1\Omega + k_2\Omega^2/2$ (where $\Omega = \omega - \omega_0$), one finds:

$$\vec{\psi}(\vec{r}, t) = \iiint F_0(\Omega; k_x, k_y) \exp\left[i(k_x x + k_y y)\right] \exp\left[-\frac{i}{2k}(k_x^2 + k_y^2)z\right] \qquad (24)$$

$$\times \exp\left[i(k_1\Omega + k_2\frac{\Omega^2}{2})z\right] \exp[-i\Omega\tau]\, d\Omega dk_x dk_y$$

where $v_g^{-1} = k_1$. The associated longitudinal component of the electric field can be then obtained from $\nabla\cdot\vec{E} = 0$, leading to a total (corrected to first order) electric field that is given by:

$$\vec{E} = \left(\hat{x}\psi + \hat{z}\frac{i}{k_0}\frac{\partial\psi}{\partial x}\right)\exp[i(k_0 z - \omega_0 t)] \qquad (25)$$

The primary magnetic field of this wavepacket can be obtained from the electric field through the material intrinsic impedance $\eta(\omega) = \eta_0/n(\omega)$ where $\eta_0 = (\mu_0/\epsilon_0)^{1/2}$. Therefore:

$$\vec{H} = \hat{y}\iiint \frac{F_0(\Omega; k_x, k_y)}{\eta(\omega)} \exp\left[i(\vec{k}\cdot\vec{r} - \omega t)\right] d\omega dk_x dk_y$$

$$= \hat{y} \iiint \frac{F_0(\Omega; k_x, k_y)}{\eta_0} (n_0 + n_1 \Omega) \exp[i(k_x x + k_y y)] \exp\left[-\frac{i}{2k}(k_x^2 + k_y^2)z\right]$$

$$\times \exp\left[i(k_1 \Omega + k_2 \frac{\Omega^2}{2})z\right] \exp[-i\Omega\tau] \, d\Omega dk_x dk_y$$

$$= \left(\frac{1}{\eta_0} \hat{y}\left[n_0 \psi + in_1 \frac{\partial \psi}{\partial \tau}\right]\right) \exp[i(k_0 z - \omega_0 t)] \qquad (26)$$

where in equation (26) $n(\omega) = n(\omega_0 + \Omega)$ and $n_1 = \partial n/\partial \omega$ at ω_0. These coefficients can, in principle, be evaluated from the corresponding Sellmeier equation associated with the dispersive medium. From $\nabla \cdot \vec{H} = 0$, one can determine, to first order, the longitudinal component of the magnetic field. The total magnetic field is found to be:

$$\vec{H} = \left(\hat{y}\frac{1}{\eta_0}\left[n_0 \psi + in_1 \frac{\partial \psi}{\partial \tau}\right] + \hat{z}i\frac{n_0}{k_0 \eta_0}\frac{\partial \psi}{\partial y}\right) \exp[i(k_0 z - \omega_0 t)] \qquad (27)$$

The power flow within the spatiotemporal wavepacket can now be established from equations (25) and (27), i.e.

$$\overrightarrow{S_{av}} = \hat{z}\frac{n_0}{2\eta_0}|\psi|^2 - i\hat{z}\frac{n_1}{4\eta_0}\left[\psi\frac{\partial \psi^*}{\partial \tau} - \psi^*\frac{\partial \psi}{\partial \tau}\right] + \frac{in_0}{4k_0\eta_0}[\psi\nabla_\perp \psi^* - \psi^*\nabla_\perp \psi] \qquad (15)$$

where $\nabla_\perp = (\partial/\partial x)\hat{x} + (\partial/\partial y)\hat{y}$. The last two terms in equation (28) correspond to relative power flow corrections. The second term along $\hat{z}$ is due to temporal effects while the $\nabla_\perp$ component accounts for energy transport because of transverse effects. We note here that the first term in equation (28) represents the dominant contribution to the power flow. Equation (28) can now be expressed in normalized units as follows:

$$\overrightarrow{S_{av}} = \overrightarrow{S_0} + \overrightarrow{S_r}$$

$$\overrightarrow{S_0} = \hat{z}\frac{n_0}{2\eta_0}|\psi_0|^2$$

$$\overrightarrow{S_r} = -i\hat{z}\frac{n_1}{4\eta_0 \tau_0}\left[\psi\frac{\partial \psi^*}{\partial T} - \psi^*\frac{\partial \psi}{\partial T}\right] + \frac{in_0}{4k_0\eta_0 d}[\psi\widetilde{\nabla}_\perp \psi^* - \psi^*\widetilde{\nabla}_\perp \psi] \qquad (16)$$

where the transverse $\widetilde{\nabla}_\perp$ operator involves the X and Y scaled coordinates .

2.2. Localized waves with hydrogen-like symmetries

Propagation invariant solutions to equation (22) can be directly obtained via separation of variables in spatio-temporal spherical coordinates R, θ, ϕ where $R^2 = X^2 + Y^2 + T^2$. To do so, we write the solution as $\psi = \psi_0 G(R) P(\theta) \exp(im\phi) \exp(-i\alpha^2 Z)$. Direct substitution of this latter form into equation (22) gives the following:

$$\frac{d}{d\theta}\left[\sin\theta \frac{dP}{d\theta}\right] + \sin\theta \left[\ell(\ell+1) - \frac{m^2}{\sin^2\theta}\right] P = 0 \tag{30}$$

$$R^2 \frac{d^2 G}{dR^2} + 2R \frac{dG}{dR} + \left(\alpha^2 R^2 - \ell(\ell+1)\right) G = 0 \tag{31}$$

It is interesting to note that a similar polar-azimuthal differential equation is encountered in the analysis of hydrogen quantum orbitals. The solutions to the Legendre equation (30) can be obtained in terms of the associated Legendre polynomials, $P_\ell^m(\gamma)$, of degree ℓ and order m where $\gamma = \cos(\theta)$. Equation (31), on the other hand, has spherical Bessel function solutions $j_\ell(\alpha R) = \sqrt{\pi/2\alpha R} \cdot J_{\ell+1/2}(\alpha R)$ which can be expressed in terms of elementary functions since ℓ belongs to the natural numbers. Therefore, invariant solutions to equation (22) are given by:

$$\psi_B = \psi_0 \sqrt{2\pi} j_\ell(\alpha R) P_\ell^m(\cos(\theta)) \exp[im\phi] \exp[-i\alpha^2 Z] \tag{32}$$

where ψ_0 is a constant amplitude. Akin to the two angular momentum quantum numbers in the hydrogen atom, the integer index ℓ takes values from the set $\ell = 0, 1, 2, \dots$ while the integer order m is constrained in the range $|m| \leq \ell$. We note that in general these solutions depend on how the spherical coordinate system is oriented with respect to the X, Y, T axes. If, for example, the T coordinate coincides with the spherical polar axis then $\theta = \tan^{-1}\left(\sqrt{X^2 + Y^2}/T\right)$ and $\phi = \tan^{-1}(Y/X)$. In principle, however, the spherical polar axis can be oriented in any direction (for example along X or Y). This choice has an important effect on the associated relative internal power flows $\overrightarrow{S_r}$. In this case, the vorticity arising from the term $\exp[im\phi]$ takes on a whole new physical meaning in space-time.

The simplest possible member in this family of solutions given by equation (32) is obtained when $\ell = m = 0$. This lowest state optical bullet has no internal spin, and because it resembles the 's' orbital in a hydrogen atom, we call it an 's' bullet. An iso-intensity contour plot of this wavepacket is depicted in Fig. 15(a). This wave is evidently spherical and its field follows a $j_0(x) \propto \sin(R)/R$ radial distribution. As a result, its intensity structure involves concentric spherical shells as shown in Fig 15(b), which represents a cross-section of this bullet in the $Y - T$ plane.

(a)   (b)
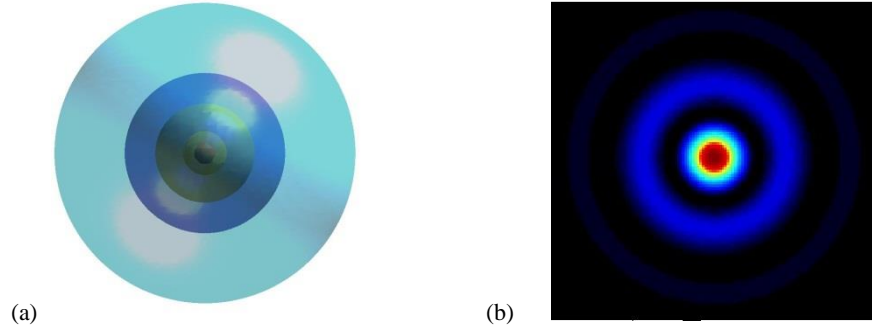
Figure 15| (a) Intensity iso-surface plots of an $\boldsymbol{\ell = m = 0}$ optical bullet. (b) Intensity cross section reveals the $\boldsymbol{j_\ell \propto \sin R/R}$ profile of this 's' state.

We note that this specific 's' member is identical to the so-called "o-wave" previously obtained in other studies [13, 54]. Figure 16(a), on the other hand, shows an iso-intensity plot of a space-time optical bullet when $\ell = 1, m = 0$, in which case it corresponds to a p_T–like orbital. The structure of this solution is no longer spherical and lacks spin since $m = 0$. It must be reiterated that this same state can be arbitrarily oriented in the X, Y, T system. A cross-section of this solution along $X = 0$ (Fig. 16(b)) reveals the finer structure in its field distribution.

(a)   (b)
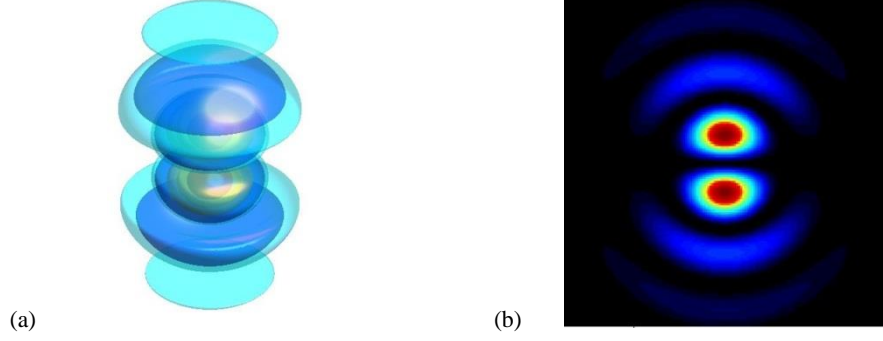
Figure 16| (a) Intensity iso-surface plots of an $\ell = 1;\ m = 0$ optical bullet. (b) Intensity cross section of 'p' shell for $X = 0$.

As in the case of 's' waves, these solutions exhibit infinitely many rings in sharp contrast to the quantum orbitals of hydrogen. This is because in our case the Coulombic potential is not involved. Similarly, p_x and p_y bullets can be generated from the same "quantum" numbers $\ell = 1,\ m = 0$. By further increasing the ℓ number, optical bullets of higher symmetries can be generated similar to the ones depicted in Fig. 17. In particular, when $\ell = 2$ and $m = 0$ (Fig. 17(a)) the propagation invariant wavepacket corresponds to the d_{TT} group (d-orbitals). An f-symmetric light bullet with $\ell = 3$ and $m = 0$ is shown in Fig. 17(b).

(a)   (b)   (c)   (d)
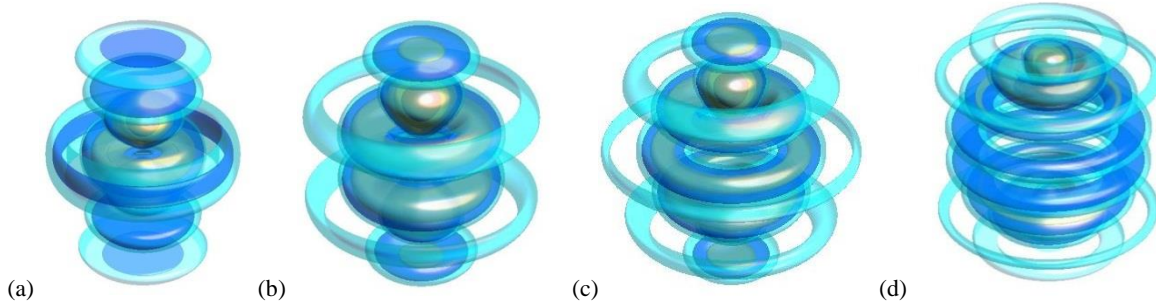
Figure 17| Intensity iso-surfaces corresponding to higher order optical bullets having $m = 0$ when: (a) $\ell = 2$, (b) $\ell = 3$, (c) $\ell = 4$, (d) $\ell = 7$.

If we assume a state with finite spin ($m \neq 0$), an internal power flow will be present in the wavepacket arising from its $\exp[im\phi]$ dependence. Figure 18(a) depicts the iso-intensity plot of an $\ell = m = +2$ bullet while Fig. 18(b) shows its corresponding internal power circulation $\overrightarrow{S_r}$ which happens in this case

to be clockwise. As would be anticipated, for $m = -2$, we obtain the same iso-intensity plot while the power circulation is counter-clockwise (Fig. 18(c)).

(a)   (b)   (c)
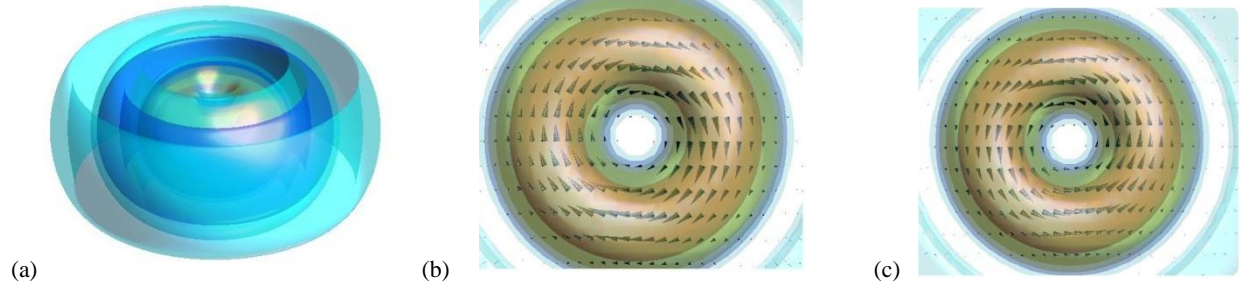
Figure 18| (a) Intensity iso-surfaces of an $\ell = 2; \, m = \pm 2$ optical bullet. (b) Top view of power circulation when $= +2$. (c) Power circulation in this same state when $= -2$.

This leads to the possibility of realizing superpositions (e.g. $\exp[+im\phi] + \exp[-im\phi]$) of spatio-temporal bullets that share the same ℓ number and opposite "spin" numbers, m. If for example $\ell = 2$ and $m = \pm 1$, the wavepacket will have a four-fold symmetry (Fig. 19(a)) and it will be d_{YT} symmetric. On the other hand, a d_{XY} symmetric wavefunction will be similar to the one shown Fig. 19(b) for characteristic indices $\ell = 2$ and $m = \pm 2$.

(a)   (b)
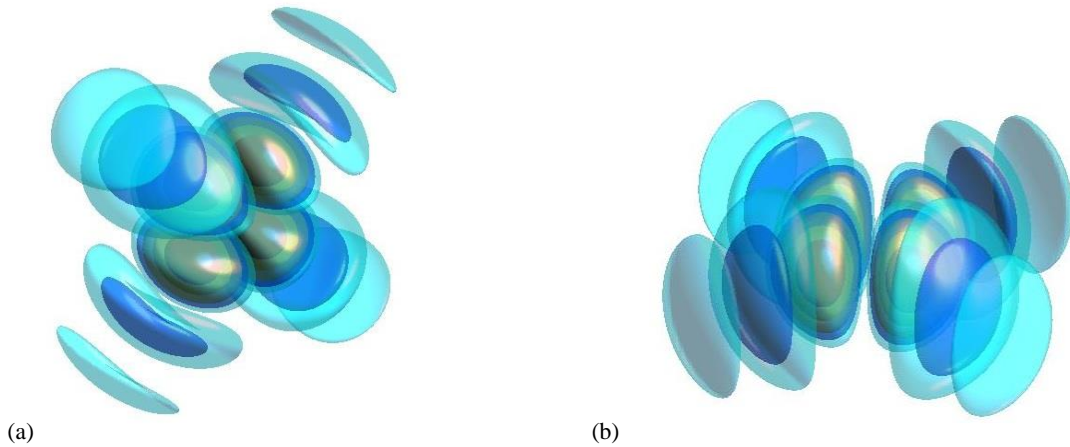
Figure 19| Superimposing optical bullets with $\ell = 2; \, m = \pm m_0$. (a) Intensity iso-surfaces with $m_0 = 1$ (b) Iso-surfaces with $m_0 = 2$.

In principle, a superposition of two such spatio-temporal hydrogen-like optical bullets that have identical "quantum numbers", ℓ and m, but with slightly different propagation constants ($\alpha_1 \approx \alpha_2$) can lead to a "breathing" wavepacket. If these two bullets exhibit opposite spins, $\pm m$, then the resulting intensity pattern rotates during propagation with period of $Z_0 = 2\pi/|\alpha_2^2 - \alpha_1^2|$. This behavior is suggested in Fig. (20) where a spinning optical bullet was generated with two almost degenerate states having $\ell = 2$, $m = \pm 2$ and $\alpha_1 \approx \alpha_2$.
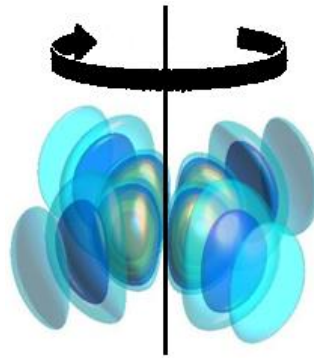
Figure 20| A rotating optical light bullet resulting from two slightly offset propagation constants.

2.3. Propagation dynamics of energy apodized light bullets

It is straightforward to show that the optical bullets presented in this paper carry infinite energy. In other words, these spatio-temporal waves happen to be dispersion-diffraction free because they are associated with an infinite norm – very much like the plane waves discussed earlier. In practice, any optical bullet can only involve finite energy. As a result, it is important to study the dynamics of this family of optical waves when they are appropriately apodized since it is necessary for their generation. In this case, a truncated bullet is expected to eventually expand in space and time depending on the degree of the apodization itself. Nevertheless, the bigger the space-time aperture is, the longer these bullets will maintain their features and the slower they will deteriorate or expand. In this section, we assume that the apodization is carried out in a Gaussian fashion [10, 35]. To analyze these dynamics, we recall that in all cases the electric field envelope obeys equation (22). We also note that in 3D a Gaussian wavepacket of the form $G(X, Y, T; Z = 0) = \exp(-R^2/w^2)$ satisfies Eq. (22) and according to the analytical solution:

$$G(X, Y, T; Z) = \frac{1}{\mu^{3/2}(Z)} \exp\left(-\frac{X^2 + Y^2 + T^2}{w^2 \mu(Z)}\right), \qquad (33)$$

where $\mu(Z) = 1 + 4iZ/w^2$. Let us now assume that a certain envelope, $\tilde{\psi}(X, Y, T; Z)$, satisfies equation (22) as well. In that case, it is straightforward to show that its Gaussian apodized counterpart also satisfies equation (22), that is:

$$\psi(X, Y, T; Z) = \frac{1}{\mu^{3/2}(Z)} \exp\left(-\frac{R^2}{w^2 \mu(Z)}\right) \tilde{\psi}(\tilde{X}, \tilde{Y}, \tilde{T}; \tilde{Z}), \qquad (34)$$

where the new coordinates appearing in equation (34) have been renormalized with respect to $\mu(Z)$, i.e., $(\tilde{X}, \tilde{Y}, \tilde{T}, \tilde{Z}) = \mu^{-1}(Z)(X, Y, T, Z)$. Equation (34) is general and holds in all cases. In the specific case of the apodized hydrogen-like optical bullets discussed here, an application of equation (34) leads to:

$$\tilde{\psi} = \frac{1}{\mu^{3/2}(Z)} \exp\left(-\frac{R^2}{w^2\mu(Z)}\right) \cdot \psi_0\sqrt{2\pi}j_\ell(\alpha\tilde{R})P_\ell^m(\cos(\tilde{\theta}))\exp[im\tilde{\phi}]\exp[-i\alpha^2\tilde{Z}], \qquad (35)$$

Where the spherical coordinates, $(\tilde{R},\tilde{\theta},\tilde{\phi})$ are associated with the coordinates $(\tilde{X},\tilde{Y},\tilde{T};\tilde{Z})$ and are given by the relations $\tilde{R} = R/\mu(Z)$, $\tilde{\theta} = \theta$, $\tilde{\phi} = \phi$. Fig. 21 displays a $Y = 0$ intensity cross section at different diffraction lengths for equation (35) with $\ell = 2, m = 0, \alpha = 1, \psi_0 = 1, w = 2$.
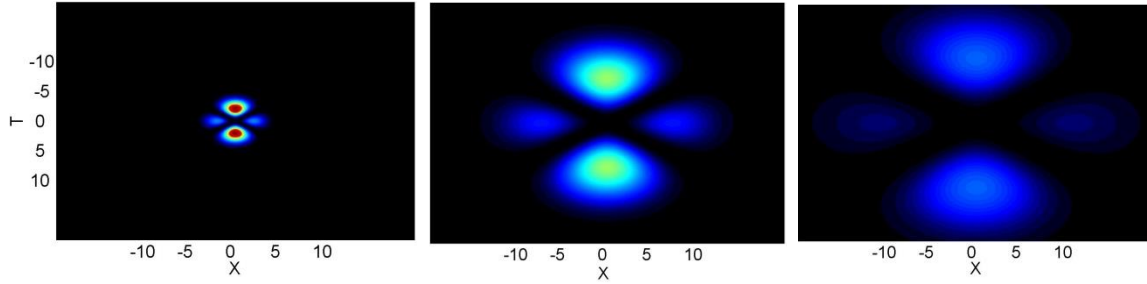
Figure 21| Propagation dynamics of an apodized hydrogen-like bullet with $\ell = 2$; $m = 0$ after a normalized distance of (a) $Z = 0$, (b) $Z = 2.66$, (c) $Z = 4$. Values are scaled to the maximum value of the bullet occurring at $= 0$.

As Fig. 21 clearly indicates, the apodized optical bullet eventually expands during propagation. This expansion can of course be slowed down by increasing the Gaussian apodization width, w .

2.4. Localized waves resulting from a spherical superposition on Archimedean and Platonic solids

In general, any non-spreading spatio-temporal wavepacket can be synthesized through a suitable superposition of "plane wave solutions" in the normalized $K_X, K_Y, \overline{\Omega}$ space as long as these points lie on a sphere (where in this last expression $\overline{\Omega} = \Omega\tau_0$). This can be understood from equation (22) by adopting invariant solutions of the form $\psi = \exp(-i\alpha^2 Z)\exp(i[K_X X + K_Y Y - \overline{\Omega T}])$. For this case, $K_X^2 + K_Y^2 + \overline{\Omega}^2 = \alpha^2$, i.e. the $K_X, K_Y, \overline{\Omega}$ the points should indeed lie on a sphere of radius α. Therefore, any superposition of such "plane wave solutions" will also remain also invariant as long as they share the same sphere of radius α in reciprocal space. Following this approach, infinitely many realizations of such invariant localized waves are attainable. One such possibility is to consider polyhedral that happen to be inscribable on a sphere such as the Platonic or Archimedean solids. In this case, the field envelope of the localized wave resulting from this superposition can be obtained by:

$$\psi_B = \exp(-i\alpha^2 Z)\sum_j \exp(i\vec{Q}_j \cdot \vec{R}) \tag{36}$$

Where $\vec{Q}_j$ represents the reciprocal vertices $\vec{Q}_j = (K_X, K_Y, -\overline{\Omega})$ on this sphere. Figure 22a displays the vertices of a Platonic regular hexahedron on a reciprocal space unit sphere occupying the sites $(\pm1/\sqrt{3}, \pm1/\sqrt{3}, \pm1/\sqrt{3})$. Similarly, the vertices corresponding to an octahedron and dodecahedron are depicted in Figs. 8b and 8c. The respective iso-intensity plots of the spatio-temporal wavepackets that are generated from these three polyhedral are shown in Figs. 8d-8f.
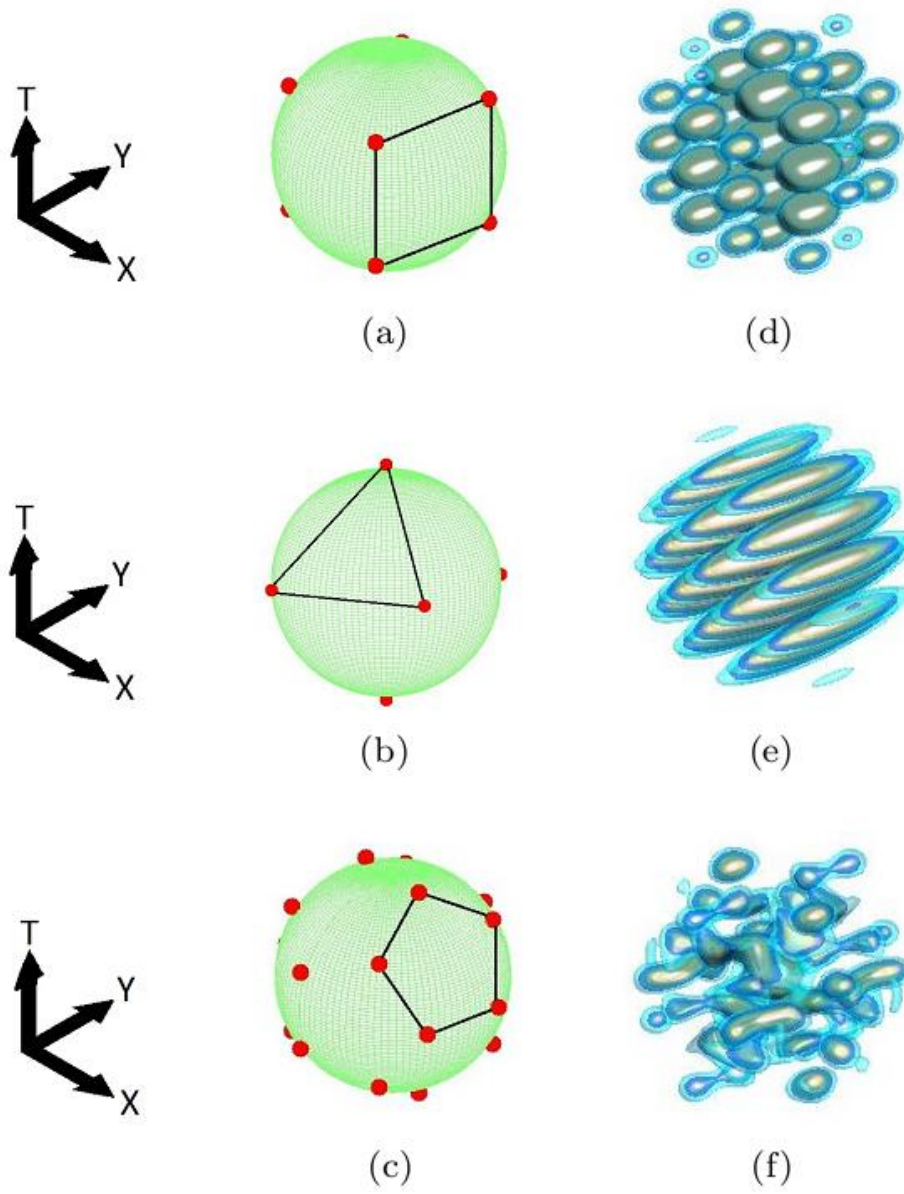
Figure 22| The vertices of a (a) regular hexahedron (b) octahedron (c) and dodecahedron inscribed in a Q-sphere. (d-f) The corresponding iso-intensity patterns generated from these arrangements.

2.5. Fourier spectra of apodized spatio-temporal bullets

Fourier spectra provide valuable physical insight not only about the structure of diffraction/dispersion-free waves, but also dictate the requirements concerning their realization in laboratory experiments. In this section, we provide a general analytical expression for the Fourier spectrum of a Gaussian apodized spatio-temporal wavepacket which obeys equation (22). More specifically, we obtain the spectrum at the origin $Z = 0$, in which case the initial field envelope is given by $\psi_B(X, Y, T, Z = 0) \exp(-R^2/w^2)$. In general, a non-spreading spatio-temporal wavepacket can be described as a Fourier superposition of plane waves in spherical coordinates. Note that in a spherical reciprocal space, $K_X = K_R \sin(\theta)\cos(\phi)$, $K_Y = K_R \sin(\theta)\sin(\phi)$, $\overline{\Omega} = -K_R \cos(\theta)$. Additionally, in this same domain, the spatio-temporal frequencies of a non-spreading wavepacket satisfying (22) lie on the surface of a sphere, $K_X^2 + K_Y^2 + \overline{\Omega}^2 = \alpha^2$, hence its spectrum can be described through the general function $\delta(K_R - \alpha)\zeta(\phi, \theta)$. In this case,

$$\psi_B(X, Y, T; Z = 0)$$

$$= \frac{1}{(2\pi)^3} \int_0^\infty \int_0^\pi \int_0^{2\pi} dK_R d\phi d\theta [K_R^2 \sin(\theta)\delta(K_R - \alpha)\zeta(\phi, \theta)] \qquad (37)$$

$$\times \exp(i\alpha[X\cos(\phi)\sin(\theta) + Y\sin(\phi)\sin(\theta) + T\cos(\theta)])$$

Thus

$$\psi_B(X, Y, T; Z = 0)$$

$$= \frac{1}{(2\pi)^3} \int_0^{2\pi} d\phi \int_0^\pi d\theta [\zeta(\phi, \theta)\alpha^2 \sin(\theta)] \qquad (38)$$

$$\times \exp(i\alpha[X\cos(\phi)\sin(\theta) + Y\sin(\phi)\sin(\theta) + T\cos(\theta)])$$

Given that this localized wave of equation (38) is apodized in a Gaussian fashion with width, w, its Fourier transform can be obtained from

$$\Psi(K_X, K_Y, \overline{\Omega}) = \int_{-\infty}^{\infty} \int_{-\infty}^{\infty} \int_{-\infty}^{\infty} dX dY dT \exp\left(-\frac{X^2 + Y^2 + T^2}{w^2}\right)$$

$$\times \psi_B(X, Y, T; Z = 0) \exp[-i(K_X X + K_Y Y - \overline{\Omega} T)] \tag{39}$$

Upon substituting equation (38) into (39) for $\psi_B(X, Y, T; Z = 0)$, all terms which do not depend on X, Y, or T may be carried out of the Fourier integral. Hence,

$$\Psi(K_X, K_Y, \overline{\Omega}) = \frac{1}{(2\pi)^3} \int_0^{2\pi} d\phi \int_0^{\pi} d\theta [\zeta(\phi, \theta)\alpha^2 \sin(\theta)]$$

$$\times \int_{-\infty}^{\infty} \int_{-\infty}^{\infty} \int_{-\infty}^{\infty} dX dY dT \exp\left(-\frac{X^2 + Y^2 + T^2}{w^2}\right) \tag{40}$$

$$\times \exp(i\alpha[X \cos(\phi) \sin(\theta) + Y \sin(\phi) \sin(\theta) + T \cos(\theta)])$$

$$\times \exp[-i(K_X X + K_Y Y - \overline{\Omega} T)]$$

Where now in equation (40), K_X, K_Y, and $\overline{\Omega}$ range from $(-\infty, \infty)$. By introducing the auxiliary reciprocal variables, $\Xi_X = K_X - \alpha \sin(\theta) \cos(\phi)$, $\Xi_Y = K_Y - \alpha \sin(\theta) \sin(\phi)$, and $\Xi_T = -\overline{\Omega} - \alpha \cos(\theta)$, equation (40) becomes:

$$\Psi(K_X, K_Y, \overline{\Omega}) = \frac{1}{(2\pi)^3} \int_0^{2\pi} d\phi \int_0^{\pi} d\theta [\zeta(\phi, \theta)\alpha^2 \sin(\theta)]$$

$$\times \int_{-\infty}^{\infty} \int_{-\infty}^{\infty} \int_{-\infty}^{\infty} dX dY dT \exp\left(-\frac{X^2 + Y^2 + T^2}{w^2}\right) \tag{41}$$

$$\times \exp(i\alpha[\Xi_X X + \Xi_Y Y + \Xi_T T])$$

The Fourier integrations in (41) can now be performed and lead to:

$$\Psi(K_X, K_Y, \overline{\Omega}) = \frac{1}{(2\pi)^3} \int_0^{2\pi} d\phi \int_0^{\pi} d\theta [\zeta(\phi, \theta)\alpha^2 \sin(\theta)]$$

$$\times w^3 \pi^{3/2} \exp\left[-\frac{w^2}{4}(\Xi_X^2 + \Xi_Y^2 + \Xi_T^2)\right] \tag{42}$$

Substituting the original expressions for the auxiliary parameters, Ξ_X, Ξ_Y, Ξ_T, equation (41) can be rewritten as follows:

$$\Psi(K_X, K_Y, \overline{\Omega}) = \frac{w^3 \pi^{3/2} e^{-(\alpha^2 + K_X^2 + K_Y^2 + \overline{\Omega}^2)}}{(2\pi)^3} \times \int_0^{2\pi} d\phi \int_0^{\pi} d\theta \, [\zeta(\phi, \theta) \alpha^2 \sin(\theta)]$$

$$\times \exp\left[i\alpha \left(\frac{w^2}{2i}\right) (K_X \cos(\phi) \sin(\theta) + K_Y \sin(\phi) \sin(\theta) - \overline{\Omega} \cos(\theta)) \right]$$

(43)

From equation (43) and equation (38), one finally obtains the Fourier spectrum of these apodized waves which is simply given in terms of their original envelope, ψ_B, where $[X, Y, T] \to (w^2/2i)[K_X, K_Y, -\overline{\Omega}]$. Therefore, the end result is:

$$\Psi(K_X, K_Y, \overline{\Omega}) = (\pi w^2)^{3/2} e^{-\left(\frac{w^2}{4}\right)(\alpha^2 + K_X^2 + K_Y^2 + \overline{\Omega}^2)} \times \psi_B\left(\frac{w^2}{2i} K_X, \frac{w^2}{2i} K_Y, -\frac{w^2}{2i}\overline{\Omega}\right)$$

(44)

Equation (44) states that if an invariant solution to equation (22) is known, then the Fourier transform of its Gaussian apodized version is immediately known. We now see that the Fourier transforms of all the spherical harmonic localized waves can be readily obtained by combining equations (44) and (35). As an example, consider the simplest of these, for which $\ell = m = 0$, and whose field profile is given by $\psi_0 \sqrt{2\pi} j_0(\alpha R) = \psi_0 \sqrt{2\pi} \sin(\alpha R)/\alpha R$. Using equation (44) we can immediately obtain the corresponding Gaussian apodized Fourier spectrum:

$$\Psi(K_X, K_Y, \overline{\Omega}) \propto w e^{-\left(\frac{w^2}{4}\right)(\alpha^2 + K_R^2)} \times \frac{\sinh\left(\frac{w^2 \alpha K_R}{2}\right)}{\alpha K_R}$$

(45)

Where $K_R^2 = K_X^2 + K_Y^2 + \overline{\Omega}^2$. Three reciprocal space iso-surfaces for both the $\ell = m = 0$ and $\ell = 1, m = 0$ cases are plotted for different degrees of Gaussian apodization (Fig. 23 and Fig. 24). As can be seen in Fig. 23, in the limit $w \to \infty$, the thickness of the surfaces become infinitesimally small, thus approaching a radius of α. As expected, in this limit the spectrum in Fig. 23 converges to the spectrum of the O-wave displayed in Fig. 15. This behavior can be readily understood from equation (45). Meanwhile the spectrum of a p_T- like orbital involving two lobes in displayed in Fig. 24.
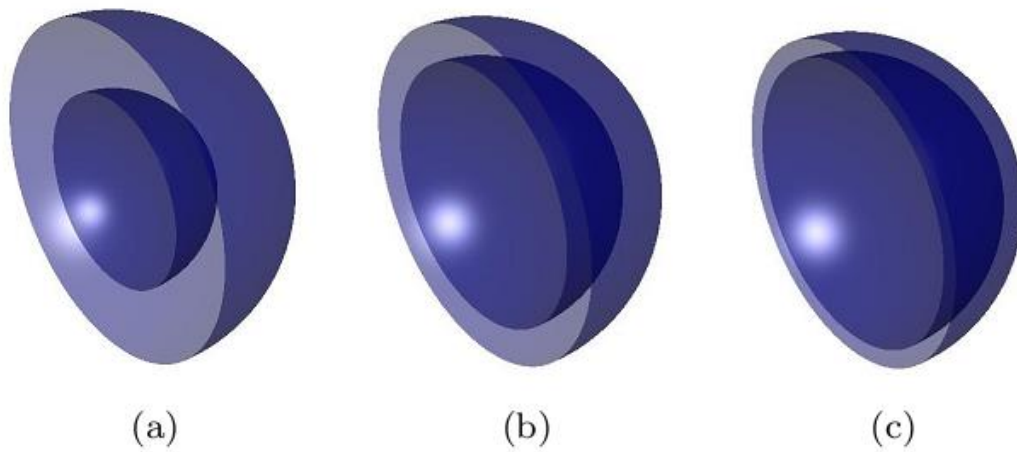
Figure 23| Isosurface spectrum plots of the $\ell = m = 0$ localized wave with various degrees of Gaussian apodization. The spherical spectrum has been sectioned in half so that the shell thickness can be viewed a) w = 5. b) w = 10. c) w = 20. In the limit that $w \to \infty$ the shell thickness becomes infinitesimally small representing the spectrum of the O-wave.
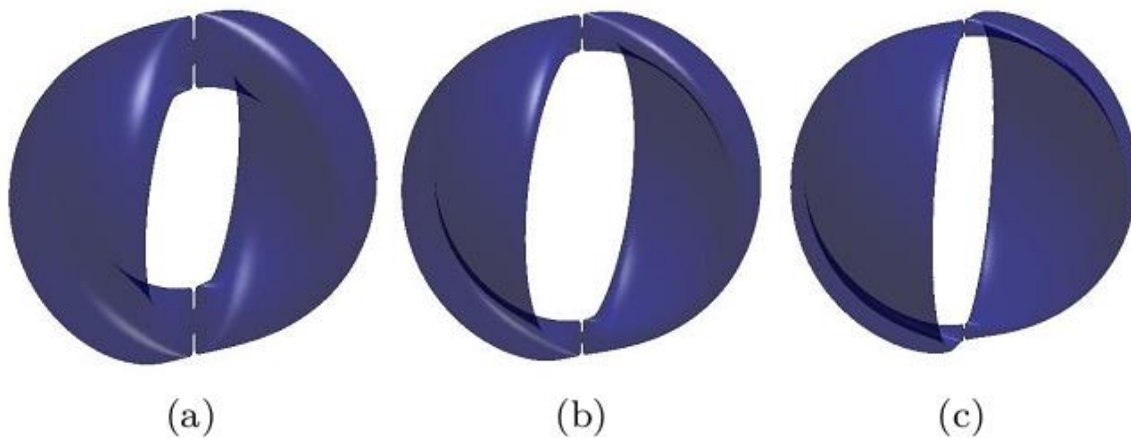
Figure 24| Isosurface spectrum plots of the $\ell = 1$, $m = 0$ localized wave with various degreees of Gaussian apodization. The spherical spectrum has been sectioned in half so that the shell thickness can be viewed a) w = 5. b) w = 10. c) w = 20.

CHAPTER THREE: DRESSED OPTICAL FILAMENTS

Since the first experimental observation by Braun *et al.* [64], optical filamentation in transparent media has been the focus of considerable attention. In general, an optical filament establishes itself through a dynamic balance of Kerr self-focusing effects and defocusing processes caused by multiphoton produced plasma [65]. To maintain this balance the filament must expend its own energy, and as expected once its power dips below a certain threshold, it eventually vanishes. Clearly, it will be important to devise schemes capable of extending the longevity of a filament. To this end, several methods have already been investigated [66-75]. For example, by introducing a negative temporal chirp, one can shift the position where a filament forms and possibly double its corresponding propagation length [66-71]. This same principle when applied to Bessel-Gauss beams has been shown to extend a filament as much as two and a half times its normal distance [74, 75]. Yet, if one is to adopt such methods, then the success of filament prolongation is ultimately limited by the amount of power contained in the initial self-focusing wavefront. One avenue to overcome this limitation would be to somehow replenish the energy of the filament during propagation.

Here, we explore a new approach by which the lifecycle of an optical filament in a transparent medium can be extended by almost an order of magnitude. Because a filament's propagation distance crucially depends on its surrounding energy [76-78], we propose to "dress" a filament with an encompassing low intensity auxiliary beam that will act as a secondary energy reservoir. This "dressing beam" is judiciously tailored so that it continuously resupplies power to the filament in a way that extends its longevity. Even more importantly, the dressing beam is prudently designed to maintain a low intensity profile throughout most its propagation; this prevents the dress from inducing nonlinear effects by itself. The role of the dress reservoir is solely to support the filament during propagation.

3.1 Theoretical treatment of dressed filaments

To describe the evolution dynamics of a dressed filament we use the Unidirectional Pulse Propagation Equation (UPPE) solver [79]. The electric field is represented in terms of its temporal and spatial spectral amplitude, $\vec{E}(k_\perp, \omega, z)$, which satisfies the equation,

$$\partial_z \vec{E}(k_\perp, \omega, z) = +ik_z \vec{E}(k_\perp, \omega, z) + \frac{i\omega^2}{2\epsilon_0 c^2 k_z} \vec{P}(k_\perp, \omega, z) - \frac{\omega}{2\epsilon_0 c^2 k_z} \vec{J}(k_\perp, \omega, z) \qquad (46)$$

Where $k_z(k_\perp, \omega) \equiv \sqrt{\omega^2 \epsilon(\omega)/c^2 - k_\perp^2}$ with $\epsilon(\omega)$ standing for frequency dependent permittivity of air. The nonlinear light-medium interactions are included within the polarization and current terms and account for the standard components of femtosecond filaments [65]. We use $n_2 \approx 1 \times 10^{-23} \ m^2/W$ for the electronic Kerr effect [80] and neglect the delayed Raman responses because of our short pulse durations. The strong-field ionization is parameterized as in [81] with effective power-law rates $\partial_t \rho = (\rho_{at} - \rho)\sigma|E(t)|^{2K}$ with $K_{N_2} = 7.5$, $K_{O_2} = 6.5$, $\rho_{at,N_2} = 2 \times 10^{25} m^{-3}$, $\rho_{at,O_2} = 5 \times 10^{24} m^{-3}$, $\sigma_{N_2} = 7.9 \times 10^{-124} s^{-1} m^{15}/W^{7.5}$, $\sigma_{O_2} = 8.85 \times 10^{-105} s^{-1} m^{13}/W^{6.5}$. We also include effective current and avalanche terms to model energy loss due to ionization; the defocusing effect of freed electrons is accounted for by a Drude model ($\tau_c = 350 \ fs$) with the current density driven by the electric field and the total freed electron density (see [82] for implementation).

For comparative purposes, we first examine the evolution dynamics of an undressed optical pulse with $\lambda_0 = 800 \ nm$ and a Gaussian envelope $\psi_F(r, t, z = 0) = \sqrt{2\eta_0 I_0} \exp[-r^2/w_F^2] \exp[-t^2/\tau_F^2]$, where $\eta_0 = 377\Omega$. For this filamenting field, we choose a beam width of $w_F = 2 \ mm$, a pulse duration of $\tau_F = 30 \ fs$, and a peak intensity of $I_0 = 5 \times 10^{15} \ W/m^2$. This corresponds to a power of about $3.27 P_{crit}$. Two cross-sections, $I_F(x, y = 0, t = 0, z)$ and $I_F(x = 0, y = 0, t = 0, z)$, resulting from UPPE simulations are displayed in Fig. 25.
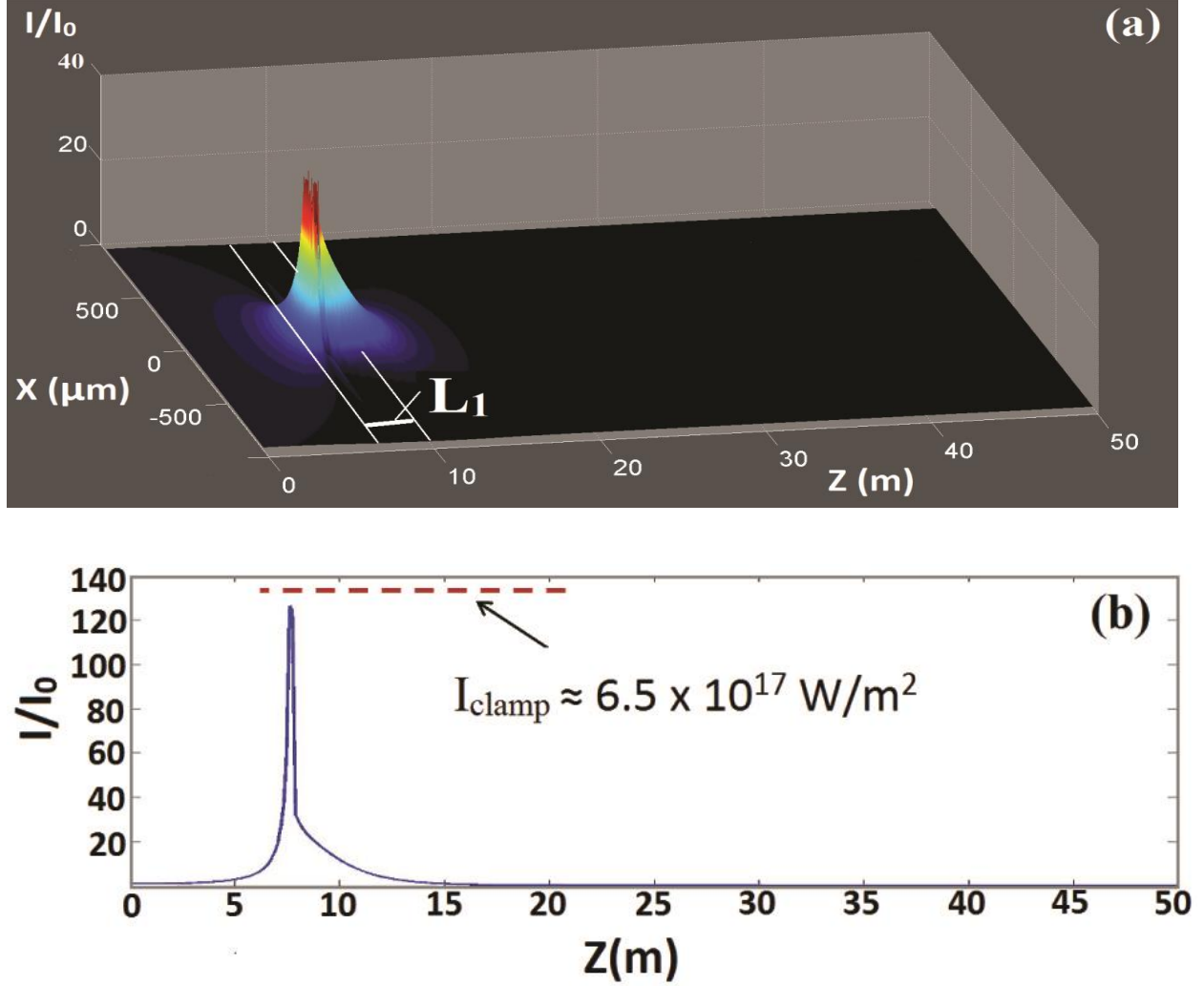
Figure 25| (a) Cross-section, $I_F(x, y = 0, t = 0, z)$, shows the formation of a filament which propagates for a distance, $L_1 \approx 2m$ and (b) inspection along the propagation axis, $I_F(x = 0, y = 0, t = 0, z)$, reveals a self-focusing collapse around 7 meters followed by one intensity clamped refocusing cycle. Intensity values are scaled to I_0 and the intensity limit in (a) is set to $40I_0$.

As indicated in Figs 25, a filament forms around 6 or 7 meters [83] and propagates for approximately $L_1 = 2m$ with a clamped intensity of a few $10^{17}\ W/m^2$ [84]. As seen, this particular filament only experiences one refocusing cycle. Next, we introduce an annular Gaussian dressing beam with a negative phase tilt of the form, $\psi_D(r, t, z = 0) = \sqrt{2\eta_0 I_D}\ \exp[-(r - r_0)^2/w_D^2]\ \exp[-i\delta r]\ \exp[-t^2/\tau_D^2]$. Note that unlike vortex beams this wavefront involves no phase singularity. The parameters for this optical dress are judiciously chosen to be $I_D = 1.5 \times 10^{14}\ W/m^2$, $w_D = 1.0\ cm$, $r_0 = 1.8\ cm$, $\delta = 85\ cm^{-1}$, and

44

$\tau_D = 30\,fs$. This corresponds to a low intensity wavefront with a large power reservoir containing $22P_{crit}$. The term $\exp[-i\delta r]$ causes the energy within this dressing beam to gently flow toward the propagation axis, and the parameter δ is tailored so that the dressing beam replenishes the filament (Fig. 26).
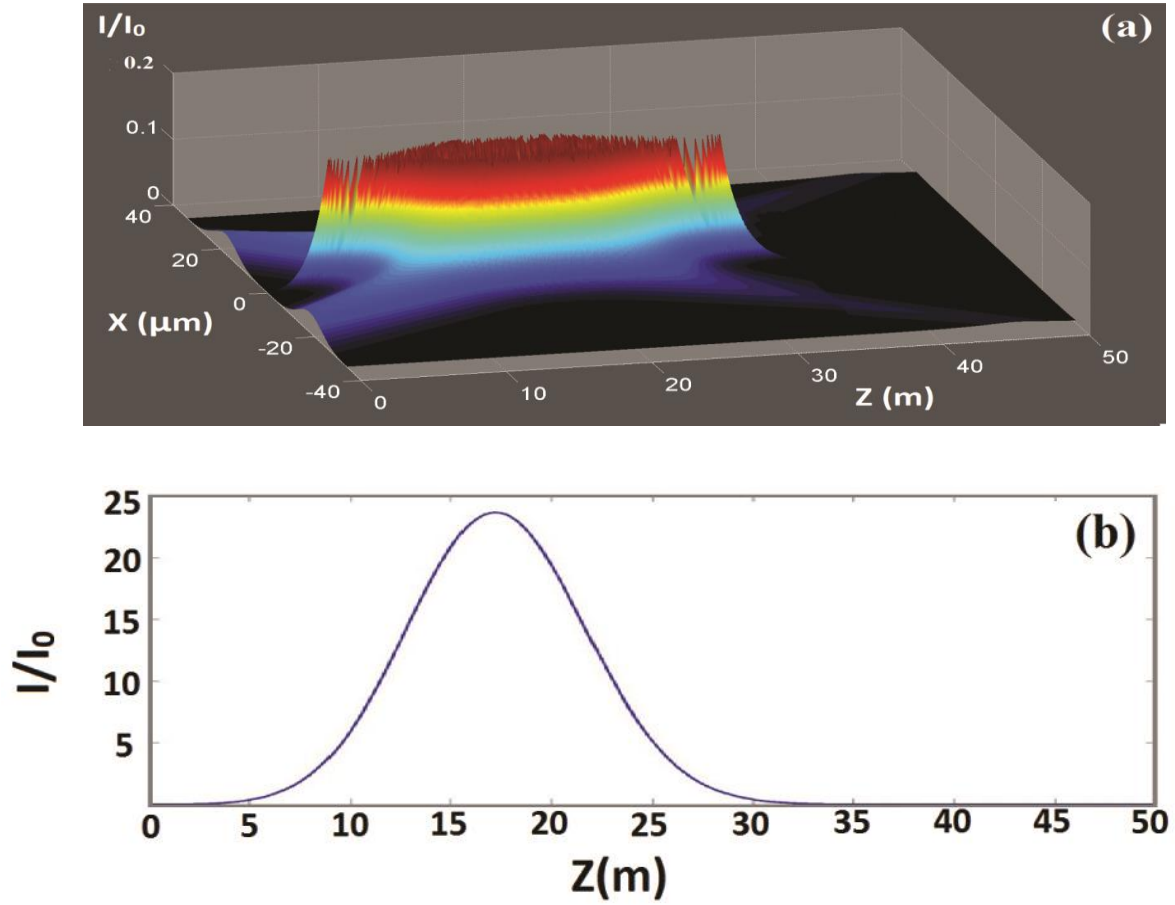
Figure 26| (a) Cross-section, $I_D(x, y = 0, t = 0, z)$, shows the evolution dynamics of the dress beam; note that the maximum intensity of the initial wavefront is only 3% that of the filament and (b) profile $I_D(x = 0, y = 0, t = 0, z)$ indicates that this particular Gaussian dress will supply additional power to the filament when it is necessary.

Figure 26 indicates that the initial maximum dressing beam intensity is quite low ($3\%I_0$) and retains a low intensity profile throughout most of its propagation. An area of concern, however, is along the propagation axis where the intensity can reach higher values. Nevertheless, while the term $\exp[-i\delta r]$ is responsible for channeling the energy toward the center, it also results in rapid defocusing.

Consequently, the dress beam itself does not induce lasting nonlinear effects and therefore does not develop a filament during propagation. This becomes evident by monitoring certain features. To begin with, the dress never undergoes self-focusing collapse; additionally, specific to these parameters, the maximum electron plasma densities generated by the dress beam are orders of magnitude less than those anticipated in a filament; lastly, a linear simulation with identical beam parameters produces virtually identical results.
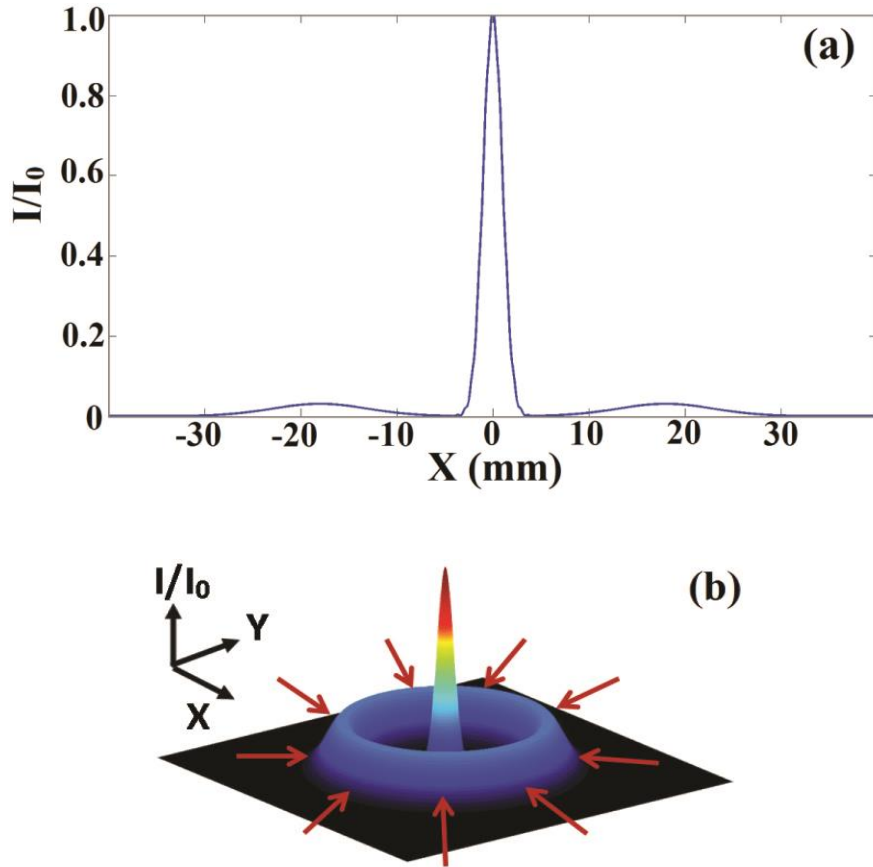
Figure 27| (a) Cross-section of the initial dressed filament, $I_{DF}(x, y = 0, t = 0, z = 0)$; note that the initial maximum intensity of the dress is only 3% that of the filament beam and (b) because of the negative phase tilt, the dress energy flows inward.

We then synthesize the dressed filament by combining the phase tilted Gaussian dress and the filamenting beam, $\psi_{DF}(r, t, z = 0) = \psi_F + \psi_D$ (initial intensity profiles are shown in Fig. 27). The

46

evolution dynamics resulting from this initial condition are displayed in Fig 28. Note that in Fig. 28a the dress beam is hardly noticeable since its peak intensity always remains low throughout propagation and is only manifested when it joins the filament beam. We wish to stress that this feature is paramount to the dress beam's efficacy, but also prohibits it from forming its own filament. Nevertheless, the results in Fig. 28b show a drastic extension of the filamentation process, which is further confirmed by the presence of plasma and a high intensity core with an average diameter of $\approx 100\ \mu m$. Thus, we are lead to conclude that both the filament and the dress are intimately intertwined during this effect. By comparing Figs. 25 and 28, we clearly see that the auxiliary dress beam replenishes the filament's power and results in many additional refocusing cycles. In this particular example, the filament's length is extended from about 2 meters to 18 meters, a nine fold improvement over the unaided case.
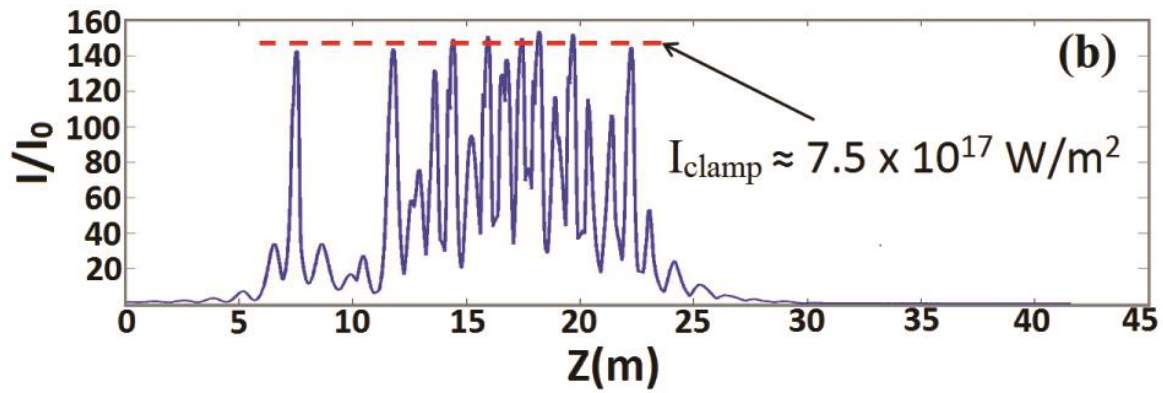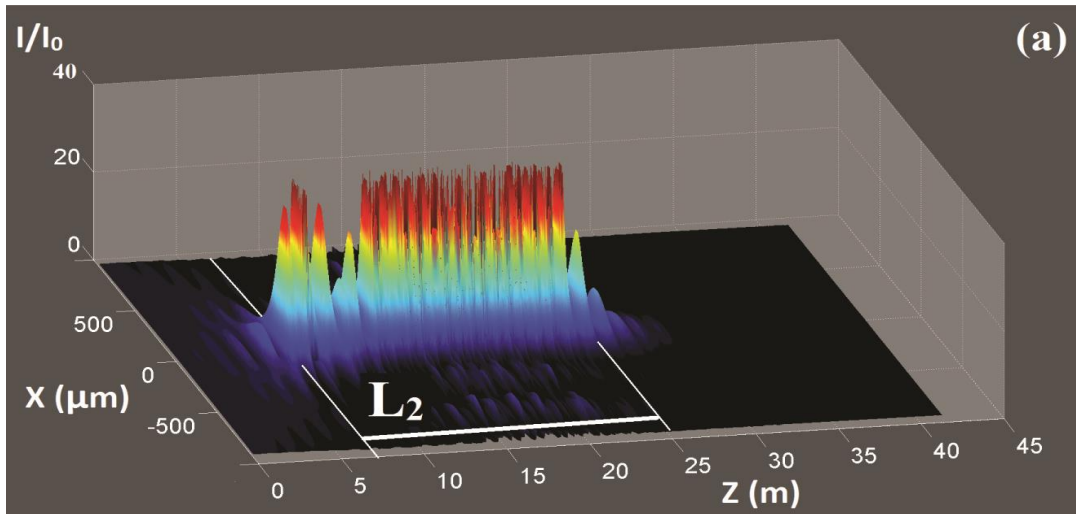
Figure 28| (a) Cross-section, $I_{DF}(x, y = 0, t = 0, z)$, shows the formation of a dressed filament which propagates for a distance, $L_2 \approx 18\ m$ after the initial focus and (b) inspection along the propagation axis, $I_{DF}(x = 0, y = 0, t = 0, z)$, reveals a self-focusing collapse around 7 meters followed by multiple refocusing cycles. The intensity limit in (a) is set to $40I_0$.

3.2. Experimental observation of dressed filaments

Here, an order of magnitude extension of an optical filament in air is reported experimentally. This is accomplished by appropriately employing a surrounding auxiliary dress beam which continuously supplies energy to the filament in a way that considerably protracts its longevity. Our experiments demonstrate that this low intensity dress acts like an artificial photon bath whose sole purpose is to continuously refuel the light string "in flight". As opposed to concentrating all the available laser energy into a single beam which can cause either a premature burn out because of ionization losses or chaotic multi-filamentation, our scheme provides a versatile route in appropriately economizing this power consumption for attaining maximum propagation distance. This mode of operation closely resembles that encountered in other dissipative systems associated with a finite amount of combustible material; maximum performance can be achieved by expending this energy at an optimal, gradual rate instead of igniting it all at once. As indicated in our study, such dressed beam configurations are in principle scalable and can thus be used in establishing long range filaments.

The basic idea behind the method is again illustrated in Fig. 29. Figure 29(a) depicts the dynamics of an unaided Gaussian pulsed filament in air. As clearly shown, this filament can only propagate for a while until dissipation effects deplete its energy after a characteristic length, L_1. Beyond this point, the beam irreversibly diffracts. On the other hand, as shown in Fig.29(b), this dynamic balance can be considerably extended up to a distance of L_2 when this same filament beam is initially surrounded by a low intensity annular dress. What makes this possible is the fact that the dress wave is radially distributed over a much broader region, so as to prevent it from triggering any nonlinear effects. In this scenario, both beams are coherent with respect to each other with the spatially-chirped dress constantly supplying energy to the high-intensity core.
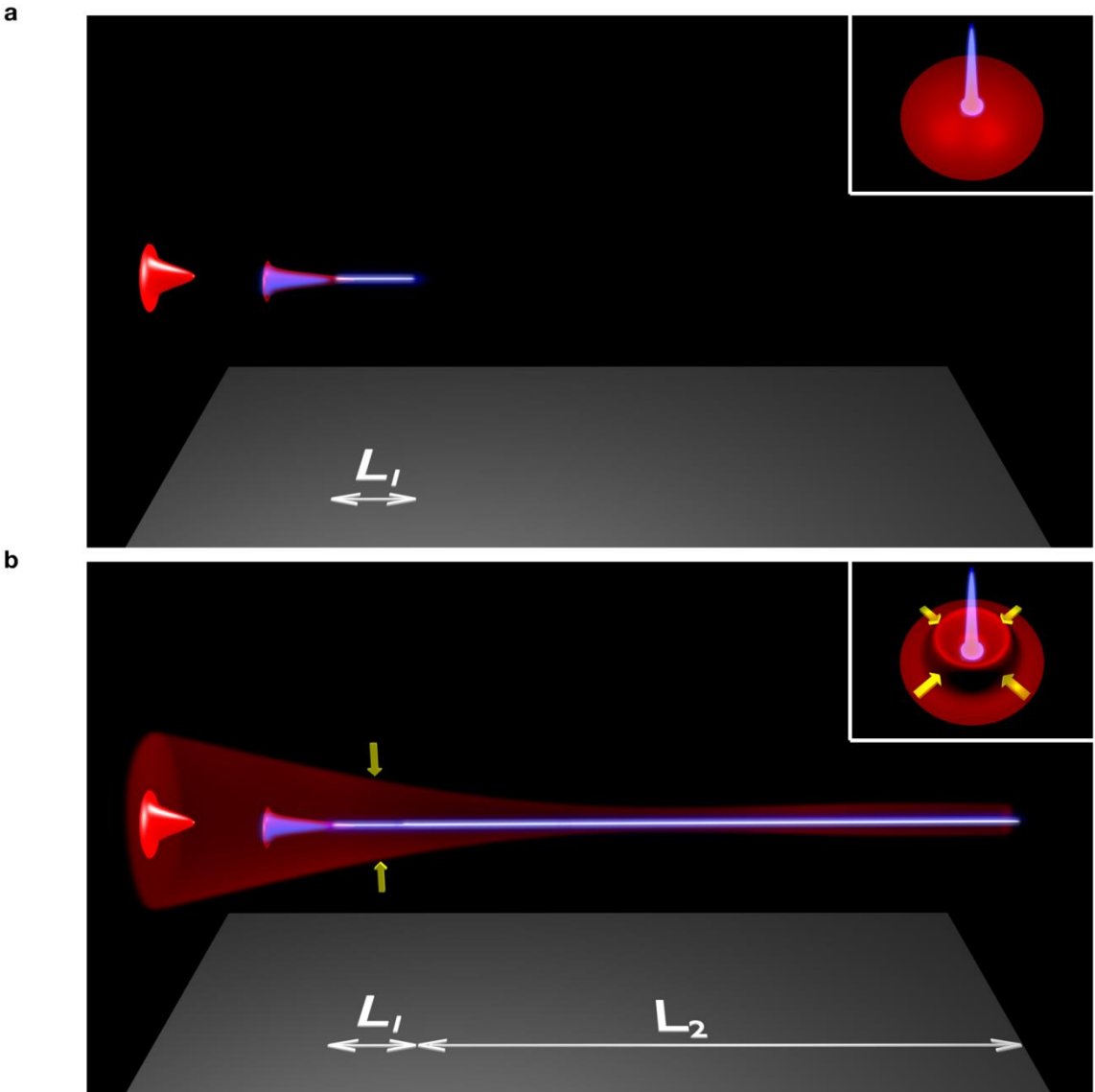
Figure 29|A dressed filament considerably protracts the longevity of an optical filament (a) A pulsed Gaussian beam (shown in the top inset) with sufficient energy will undergo self-focusing collapse and form a filament that propagates a distance L_1. (b) If, however, this same beam is appropriately dressed with a convergent annular beam (bottom inset), the filament range can be extended by an additional distance L_2. The yellow arrows in the inset represent the transverse Poynting vector for the energy influx into the filament core.

To demonstrate the aforementioned approach in a laboratory setting, a scaled-down arrangement is used, as schematically shown in Fig. 30(a). Both the primary Gaussian filament beam and the accompanying dress are derived from a single Ti: Sapphire femtosecond laser system that produces 40 fs pulses at 800 nm. The pulse repetition frequency is 10 Hz and the maximum energy per pulse can reach

50

up to 25 mJ. The output beam from the laser is unevenly split into two, one of which is weakly focused by a lens with a focal length of 2 m and becomes the primary Gaussian filament. Prior to focusing, this beam is truncated to a diameter of 4 mm. Meanwhile, the second wavefront has a much larger diameter (12 mm) and is focused by a conical axicon with an apex angle of 179.8° and undertakes the role of the low intensity dress beam. By using this approach, the resulting annular wave acquires a linear spatial chirp in the transverse plane, $\propto \exp(-i\delta r)$, where δ is a constant defined by the geometry of the axicon and r is the transverse radial coordinate. The radial chirp causes a gradual transport of energy from the periphery to the central core of the beam upon propagation, as shown by the transverse Poynting vector arrows, $\overrightarrow{S_t}$, in Fig. 29(b). In this configuration, the two wavefronts share the same polarization and wavelength and are designed to interact for about 2m over which refueling is expected to take place. The two beams are temporally synchronized using a motorized delay stage and are spatially recombined (Fig. 30(a)). After accounting for the losses resulting from optical elements in our setup, the maximum pulse energies delivered in the interaction zone are 0.87 mJ and 3.5 mJ for the filament and the dress beam, respectively. The peak power of the main beam is about twice the threshold power for self-focusing in air. The intensity profile of this filament-dress arrangement just before the Rayleigh zone is shown in Fig.30(b). It should also be noted that relative optical phase fluctuations between the Gaussian and dress beam resulted in time-averaged intensity patterns.

Our experimental results are summarized in Figure 30(c). With the primary Gaussian beam acting alone, the length of the generated plasma channel is about 20 cm. The dress beam on the other hand, by itself, does not produce any measurable plasma and thus does not form a filament. This is anticipated since the dress energy reservoir is meant to behave linearly so as to discourage the onset of its own filamentation. On the other hand, when the two beams are launched together (with $\delta \approx 21 \text{ mm}^{-1}$), the length of the generated plasma channel reaches up to 220 cm, indicating an eleven-fold improvement over the former result. As previously indicated, what contributes to this prolongation is the constant refueling offered by the dress energy tank. In our experiments, we found that this interaction is robust and is

51

relatively insensitive to existing imperfections in either beam. We emphasize again that this interaction involves only one light string and is by no means a multifilamentary process.
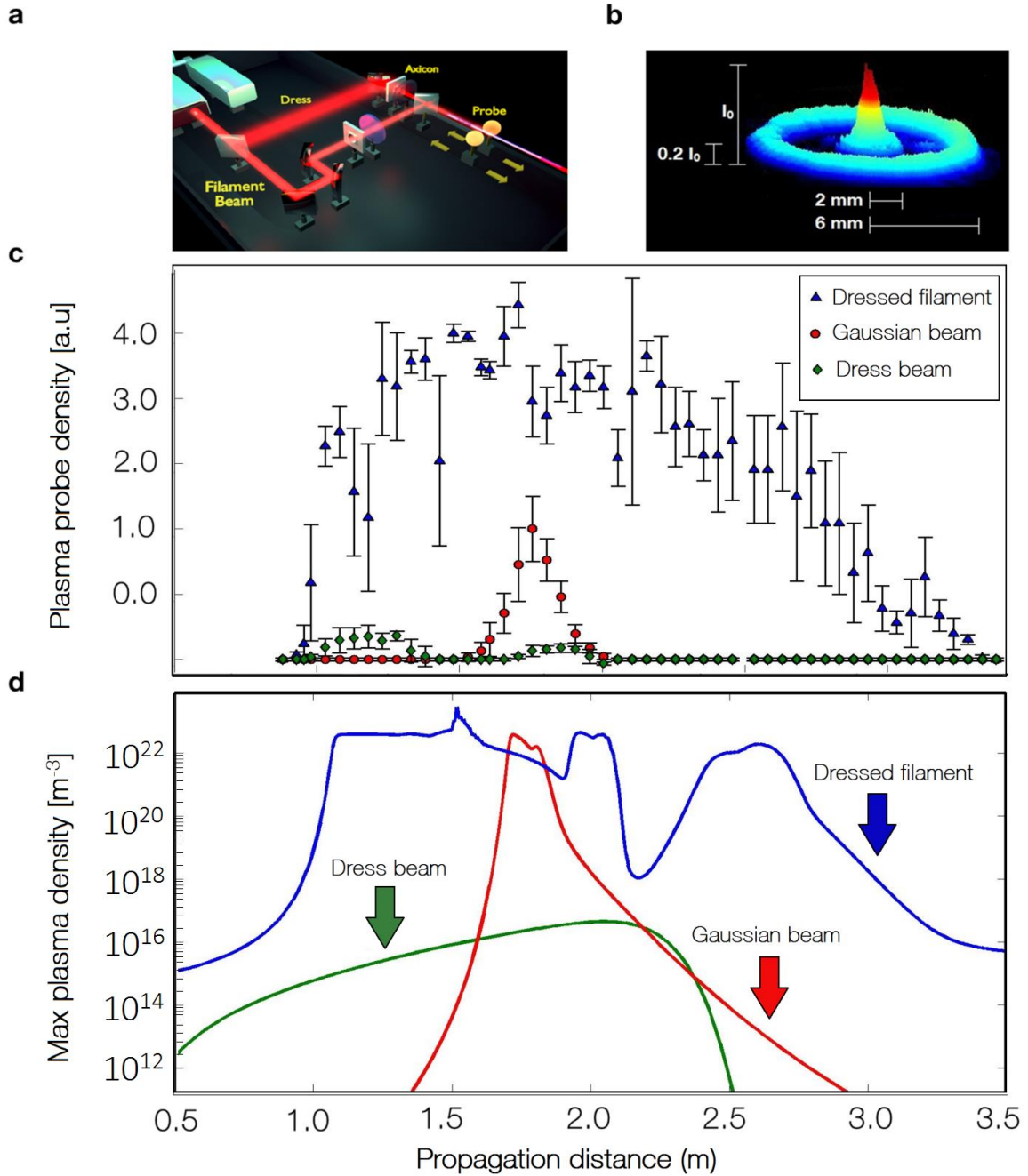
Figure 30| Experimental investigation of dressed optical filaments. (a) Experimental setup. The input beam is unevenly divided into two parts. The lower-energy portion is focused by a convergent lens with a focal length of $2m$ and produces a short plasma filament in air; the higher-energy beam is passed through

a shallow axicon lens and assumes the role of the dressing beam. Plasma generation in air is quantified using a capacitive plasma probe. (b) The intensity profile of the primary and dress beams together, as observed right before the interaction zone. (c) Experimental demonstration of an extended filament when the primary beam carries an energy of $0.87\,mJ$ and the accompanying dress beam, $3.50\,mJ$. In this arrangement, the light string propagates for $220\,cm$ which corresponds to an eleven-fold improvement over the unaided filament. (d) Plasma density as obtained from numerical simulations for the three cases shown in (c). This also corroborates an eleven-fold extension of the filamentation process with the aid of a dress beam.

We have also conducted similar experiments using different focusing parameters for both the Gaussian and dress beam. In all cases, the results were found to be qualitatively the same: The dressed filament always outperforms its unaided counterpart. Note that this significant filament elongation is possible in spite of the fact that its range is ultimately limited within the Rayleigh zone of the lens. This improvement can become even more impressive once quasi-collimated dressed filaments are used in long-range arrangements. Results from numerical computations corresponding to our experiments are shown in Fig. 30(d). Our simulations utilize a femtosecond pulse propagator based on the Unidirectional Pulse Propagation Equation (UPPE) [79]. In all cases our numerical findings are in good agreement with experiment. The minor differences observed are because of statistical fluctuations in initial conditions. To demonstrate that the observed plasma elongation is specifically due to the constant refueling process and is not the outcome of simply increasing the total energy in a pulse, experiments were conducted where energy levels comparable to those used in our previous filament-dress configurations (4.4 mJ) were packed in the same primary filament beam. In every case, the beam collapsed much faster and its energy was inefficiently consumed. In addition, the plasma density generated by the auxiliary beam alone remained several orders of magnitude below the values necessary for the filamentation process. The dependence of the filament's elongation on the dress energy was also investigated in detail.

To better understand how the throughput of a dissipative phenomenon like a light string can be externally enhanced, one can offer the following argument: The peak on-axis intensity in a femtosecond laser filament is clamped to a value, I_{clamp}, determined by the onset of plasma generation which is by

nature a threshold-like process. If we only consider losses from ionization (i.e. by ignoring diffraction/defocusing losses), then in this quasi-steady state regime, the filament diameter remains almost invariant and as a result the rate of the eight-photon oxygen ionization loss, $n_{o_2}(8\hbar\omega)(\sigma I_{clamp}^8)S_f\tau$, is approximately constant. Here, n_{o_2} is volumetric molecular density of oxygen in air, $8\hbar\omega$ is the energy associated with eight-photon absorption, σ is an eight-photon absorption coefficient, S_f represents the filament cross-sectional area, and τ the pulse duration. Interestingly, the performance of any dissipative configuration can always be optimized with respect to the rate at which energy is replenished. For example, this becomes evident even in relatively simple first-order systems where variational principles through Lagrange multipliers can be directly employed. Under such conditions, one can show that the longevity of such an energy consuming process can be maximized as long as the resupply rate is constant and related to the initial conditions and constraints. In other words, the most efficient rate of energy inflow would be that which just compensates for losses. Supplying any more additional energy would result in wasteful ionization loss, while an insufficient energy in-flow would cause the filament to cease. In regular filaments, the energy flow from the photon bath towards the beam axis is driven by beam self-focusing – an intrinsically unstable nonlinear process that inevitably causes unnecessary local intensity overshooting. On the other hand, in the dressed filament case, energy from the auxiliary beam flows into the filament core in a controllable manner, which ensures a steady energy resupply rate and results in optimized energy expenditure.

As an alternative to dressed-filaments, one could have also employed diffraction-free wavefronts, like self-healing Bessel beams—similar to those previously used in other settings [74, 75]. Experimental data obtained from intense Bessel beams are depicted in Fig. 31. Clearly, when compared to Fig. 30(c), this arrangement still underperforms even though it contains twice the energy level (8.4 mJ). This is because the transverse energy influx within a Bessel beam is not ideally suited in the prolongation of a filament.
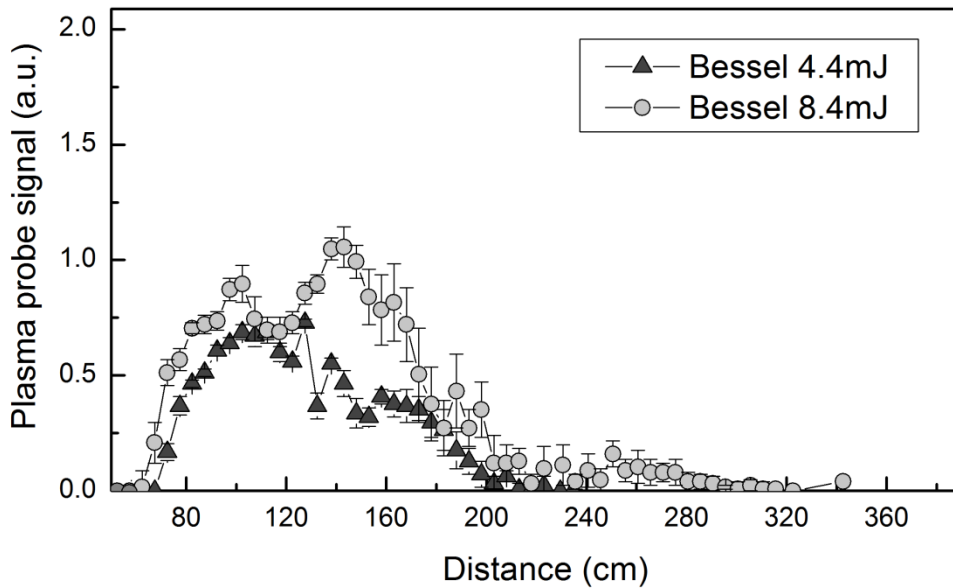
Figure 31| Experimental investigation of dressed optical filaments. **(a)** Experimental setup. The input beam is unevenly divided into two parts. The lower-energy portion is focused by a convergent lens with a focal length of **$2m$** and produces a short plasma filament in air; the higher-energy beam is passed through a shallow axicon lens and assumes the role of the dressing beam. Plasma generation in air is quantified using a capacitive plasma probe. **(b)** The intensity profile of the primary and dress

As previously mentioned, the advantage offered by our scheme becomes even more evident in long-range settings (Fig. 32). In this case, both the filament and the dress are almost collimated thus allowing for extended interaction regions. To demonstrate this possibility, pertinent simulations were carried out using the UPPE method (axicon apex angle of $\approx 179.9°$, and clear aperture radius of $\approx 1cm$). Filament extensions up to 45 meters are possible in air using dressed beams containing a total energy of 28 mJ as opposed to a filament alone (carrying 2 mJ) that lasts up to 3 meters. This is possible in spite of the fact that the filament beam is initially launched with a moderate ~ 2 mm intensity FWHM. Instead, if this same energy of 28 mJ is concentrated in the primary filament, it only propagates 13 meters after the onset of self-focusing. In this latter setting, the energy in-flow from the photon bath into the filament core is driven by nonlinear self-focusing, resulting in inefficient energy consumption. We would like to note that in general, the dynamic balance between the different focusing and de-focusing effects is more

complex given that it results from a temporal and spectral re-shaping of the pulse waveform during propagation.
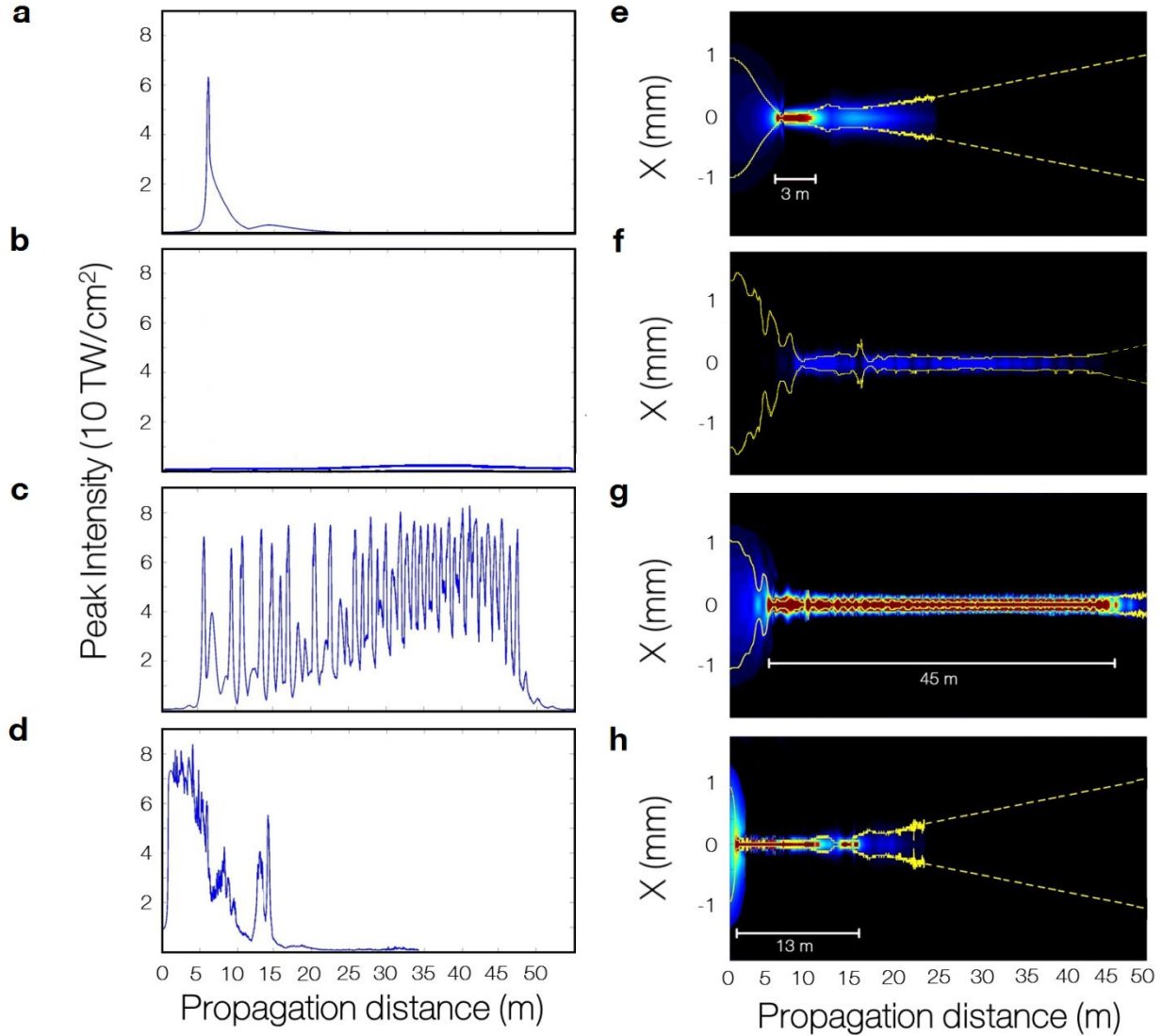
Figure 32| Dressed optical filaments in long-ranged settings. (a) Numerical simulation of the peak on-axis intensity for a collimated Gaussian beam starting with a 2 mm FWHM and 2 mJ of energy. The string decays after about 3 meters. (b) Maximum on-axis intensity when a dress beam with 26 mJ of energy propagates alone. Even with this large amount of energy, a filament never forms because the dress maintains a low intensity throughout propagation and only refuels the pre-existing filament. (c) On-axis intensity when the central beam in (a) is aided by the same co-propagating dress wave in (b). Here, the dressed filament propagates over 45 meters, a fifteen-fold improvement over the previous result. (d) Propagation dynamics when all 28 mJ of the energy are packed in a Gaussian beam that propagates alone. High on-axis intensity is maintained for only 13 meters. (e-h), Intensity cross sections as a function of the propagation distance corresponding to (a-d) respectively; in each case, the propagation varying FWHM of

the central beam is indicated by a pair of yellow lines. (f) The intensity of the dress beam propagating alone is considerably lower during propagation. In (g) the filament maintains an intensity FWHM of ~100 microns over a distance of 45 meters.

3.3. Supplementary details of dressed optical filaments

In the following sections, various supporting details concerning the experimental observation of dressed filaments are explored.

3.3.1. Filament elongation by increasing the dress energy

The effectiveness of a dress beam depends intricately on several factors such as its shape, spatial chirp, pulse width and power. In this section, we show that by keeping all other dress parameters constant, one can monotonically increase the length of a dressed filament by simply increasing the dress's peak power.
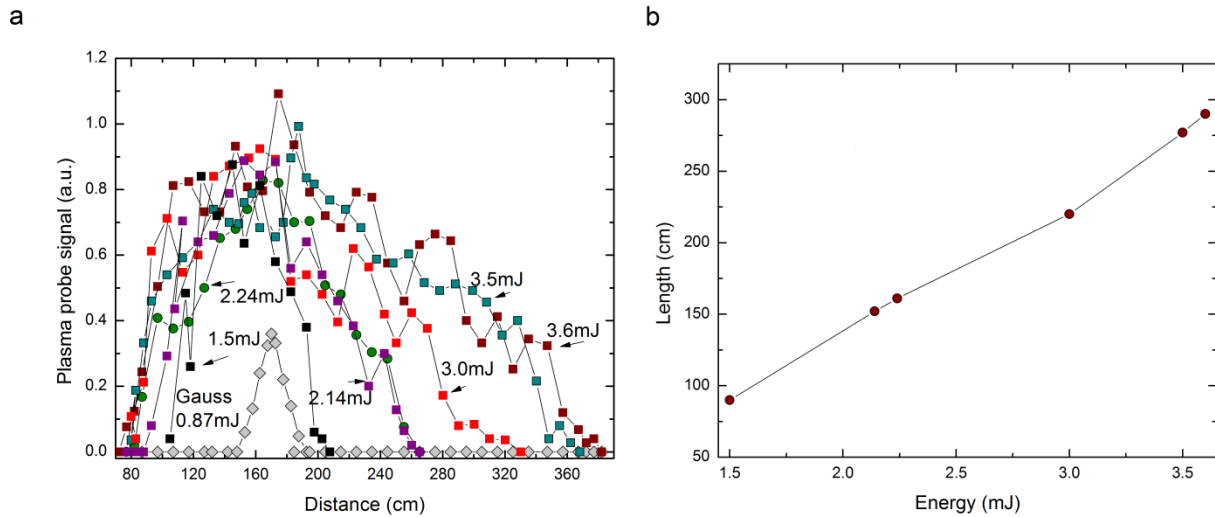
Figure 33| Dressed filament extension as a result of dress energy. (a) The on-axis plasma probe signal as a function of propagation distance using the same experimental setup presented in Fig. 30 but with several different dress energies. (b) The filament length is found to monotonically increase with increasing dress energy.

Figure 33 depicts experimental results illustrating this aspect. These results correspond to the dressed filament experiment that was presented in Fig. 30 but with different dress energies. Fig. 33a overlays the observed plasma probe signal for both the Gaussian beam alone ($E_{in} = .87 \ mJ$) and multiple dressed filament arrangements with various energies ($E_{DF} = E_{in} + \{1.5, 2.14, 2.24, 3.0, 3.5, 3.6\} \ mJ$). It is clear that as the energy within the dress beam increases, the propagation length of the dressed filament also increases. Fig. 33b summarizes these results by displaying the filament length as a function of the input dress energy; the elongation is found to increase with larger dress energies.

3.3.2. Variational Analysis of dissipative systems

In order to gain insight as to how in general a dissipative process can be optimized when a finite amount of energy is provided, one can resort to variational principles. This becomes more evident by assuming a constant energy consumption rate. In this regime, this complex refueling process can be effectively described via the following "phenomenological" equation:

$$\frac{d}{dz}\langle U \rangle + \bar{\gamma}\langle U \rangle = f(z) \tag{47}$$

where $\langle U \rangle$ is the time averaged energy stored in the optical filament: $\langle U \rangle = \langle \iint_{-\infty}^{+\infty} dx dy |\psi|^2 \rangle$. Here the function $f(z)$ represents the rate of energy supplied by the dress beam and $\bar{\gamma}$ is an effective decay rate because of multi-photon absorption.

Of interest is to find an optimum function $f(z)$ which maximizes the filamentation distance or the functional $J = \int_0^L \langle U \rangle dz$ subject to the constraint $K = \int_0^L f(z)\langle U \rangle dz$ where K is a constant. This can be achieved under the condition that any variation in the function f, extremizes the functional $J - \lambda K$, i.e.:

$$\delta[J - \lambda K] = 0 \tag{48}$$

where λ is a Lagrange multiplier to be determined. This latter relation can be written in its integral form:

$$\delta \int_0^L [\langle U \rangle - \lambda f(z) \langle U \rangle] dz = 0 \tag{49}$$

This can be written in the form of $\delta \int_0^L \mathcal{L} dz = 0$ where $\mathcal{L} = (1 - \lambda f) \langle U \rangle$ is an effective lagrangian for this problem. In order to solve this variational equation, first of all it should be noted that the phenomenological equation admits the following general solution:

$$\langle U \rangle = e^{-\bar{\gamma} z} \left[\langle U \rangle_0 + \int_0^z e^{\bar{\gamma} z'} f(z') dz' \right] \tag{50}$$

where $\langle U \rangle_0$ represents $\langle U \rangle$ at $z = 0$. Therefore we have:

$$\mathcal{L} = \left(1 - \lambda f(z) \right) e^{-\bar{\gamma} z} \left[\langle U \rangle_0 + \int_0^z e^{\bar{\gamma} z'} f(z') dz' \right] \tag{51}$$

Now, by defining the following variable:

$$q = \int_0^z e^{\bar{\gamma} z'} f(z') dz' \tag{52}$$

one can easily show that:

$$\mathcal{L}(q, q_z, z) = (1 - \lambda e^{-\bar{\gamma} z} q_z) e^{-\bar{\gamma} z} [\langle U \rangle_0 + q] \tag{53}$$

where $q_z = \frac{d}{dz} q$. By using the Euler-Lagrange equations:

$$\frac{\partial}{\partial z} \left(\frac{\partial \mathcal{L}}{\partial q_z} \right) = \frac{\partial \mathcal{L}}{\partial q} \tag{54}$$

One can then obtain the optimum resupply rate $f(z)$:

$$f(z) = \frac{1}{2\lambda} \tag{55}$$

which happens to be a constant function. The constraint $K = \int_0^L f(z) \langle U \rangle dz$ can be used again to determine the constant λ.

3.3.3. Temporal dynamics of dressed filaments

In general, the refueling dynamics of a dressed filament is a complex spatio-temporal process. To account for the time evolution of this particular beam configuration, we provide temporal data suggesting that refocusing cycles occur provided that the power levels exceed the critical threshold for each cross section in time.

As an example, we here study the temporal profiles of a dressed filament with parameters identical to those used in Fig. 32 (Fig. 34).
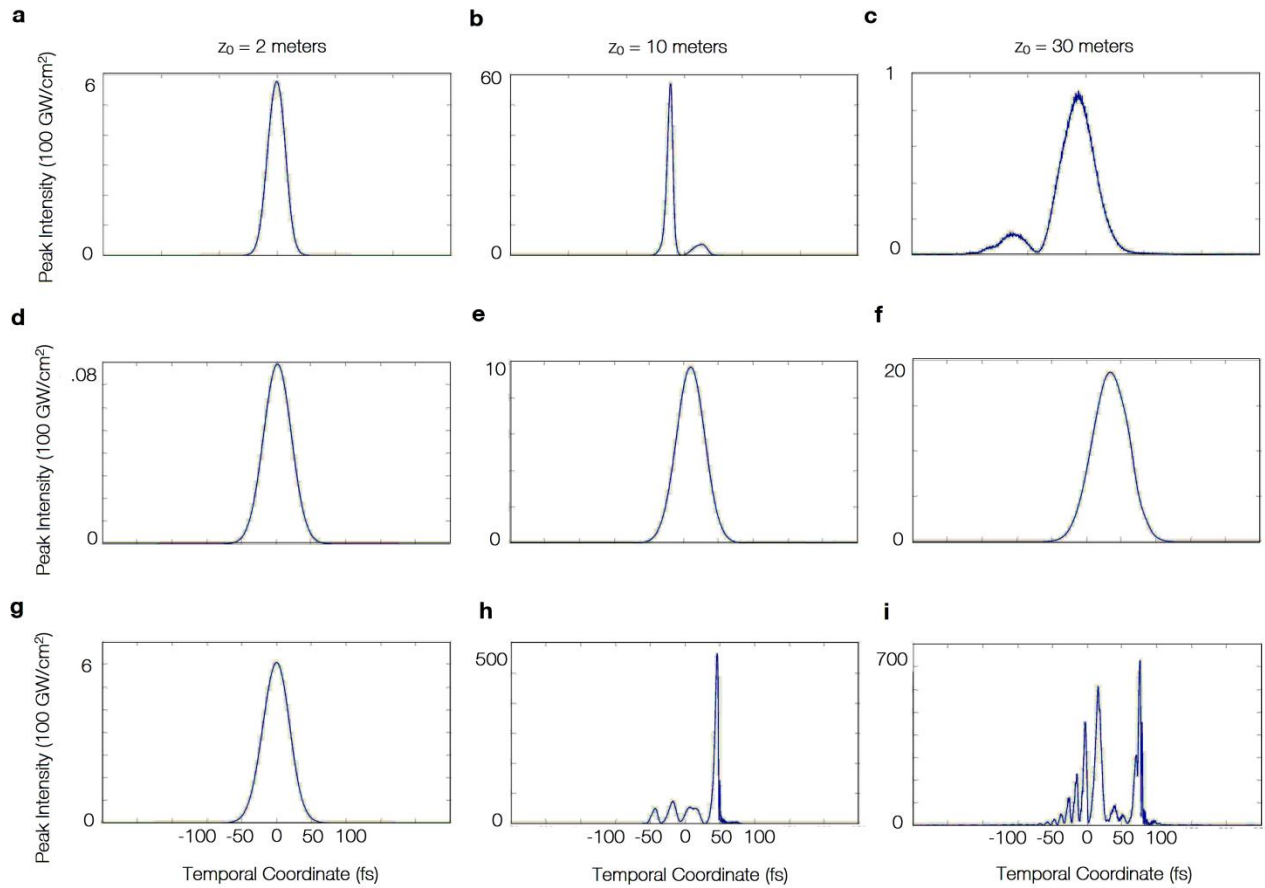
Figure 34| Temporal pulse profiles along $r = 0$ for three different propagation distances (2, 10, and 30 meters). The parameters in the simulations are identical to those in Fig. 32 (a-c) Pulse shapes for the Gaussian filament alone, (d-f) the annular dress alone, and the (g-i) dressed filament.

Fig. 34 displays cross sections of the pulse shapes (along $r = 0$) at three different propagation distances for the central Gaussian filament, the dress beam, and the dressed filament. Figs. 34(a-c), associated with the Gaussian filament alone, indicate that the pulse is initially normally distributed in time, (a); however, after the self-focusing collapse, the pulse splits (because of normal dispersion) as illustrated at 10 m of propagation, (b). This split pulse is then below the critical power for any further self-focusing and thus begins to broaden, (c). Figs. 34(d-f) show the pulse evolution of the dress beam by itself. Because this wavefront remains quasi-linear throughout most of its propagation, it mostly retains its original Gaussian shape. Furthermore, the intensity of the cross sections begin to rise as the dress beam approaches the axis. Finally, Figs. 34(g-f) display the pulse shapes of the combined dressed filament. Although the pulse begins with approximately the same intensity and shape as in the unaided case, (g), the extra energy provided by the dress beam causes the filament to undergo multiple refocusing cycles. This in turn splits the pulse multiple times as is apparent after 10 meters of propagation, (h). By 30 meters of propagation, the nonlinear dressed filament is still undergoing refocusing cycles and the pulse shape becomes more involved (i).

3.3.4. Power flow of refueled optical filaments

During propagation, the transfer of power between a filament and an optical dress beam can reveal some of the interaction dynamics between the two entities. This information can be extracted once the axially symmetric electric field envelope, ψ, is known at a specific position along the propagation direction, z_0. After integrating over the temporal coordinate, the time-averaged power flow in the transverse radial direction, S_r, is then proportional to, $S_r(r, z = z_0) \propto i \left(\psi \frac{\partial \psi^*}{\partial r} - \psi^* \frac{\partial \psi}{\partial r} \right)$.

To illustrate this process, let us consider the arrangement in Fig. 32. We are interested in how S_r behaves for three of the cases presented, i.e. a central Gaussian beam alone, a dress beam alone, and a dressed filament arrangement. For each of these three scenarios, Fig. 35 displays S_r as a function of radius at two locations along the propagation axis.

Figs. 35(a,b) provide the radial Poynting vector before and after the collapse point for the central beam alone. In this case, we find that power flows inward before the collapse (as evident by the negative values) and then outward afterwards (positive values). Figs. 35(c,d), on the other hand, show that the power from the dress beam first gradually approaches the central axis and then monotonically emanates away from it. Most interestingly, however, is the dressed filament case seen in Figs. 35(e,f). Apart from some oscillatory-like behavior, power flows primarily from the surrounding photon bath into the filament core during portions of the refocusing cycles which are dominated by self-focusing collapse. However, when plasma has caused the filament to defocus, power moves from the center of the beam toward the energy reservoir.
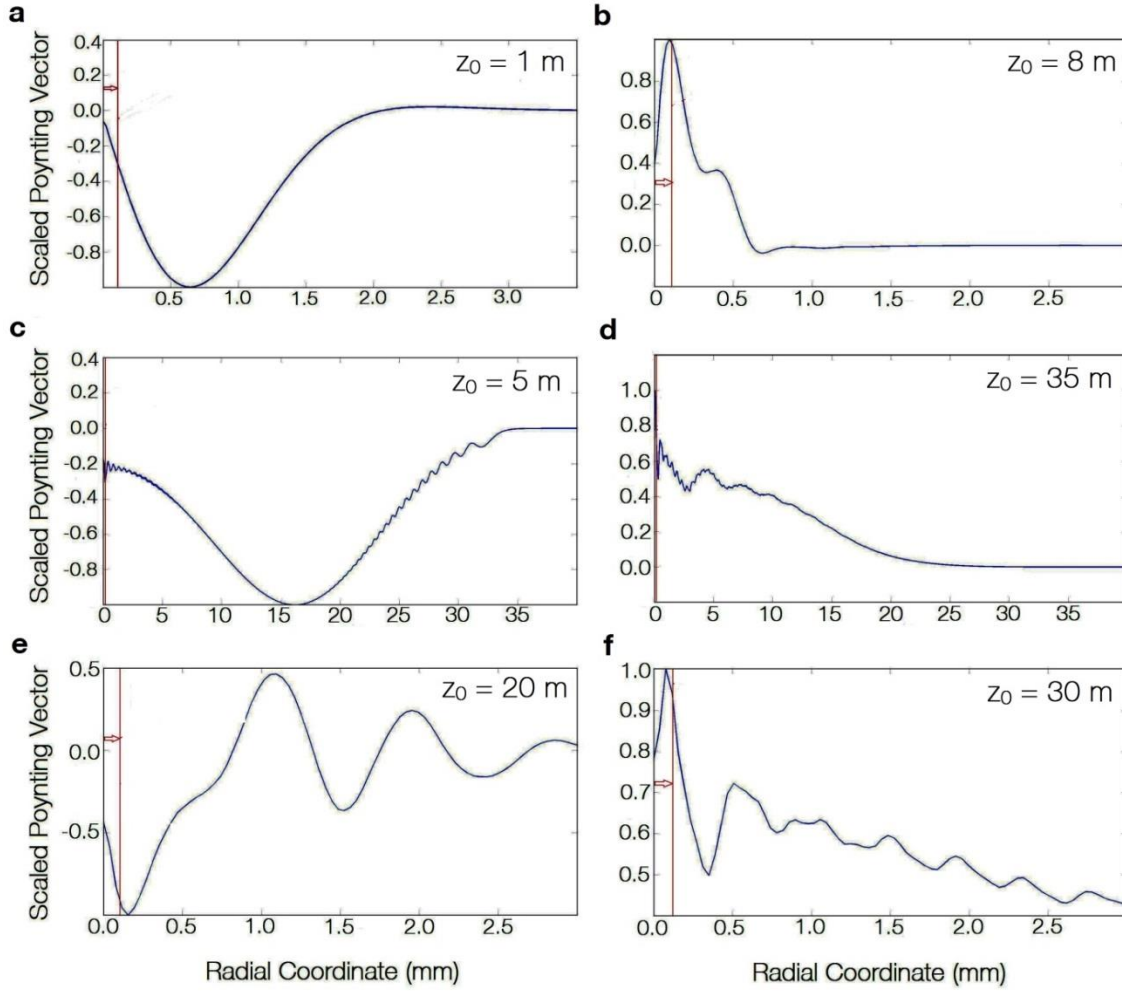
Figure 35| Numerically computed transverse time-averaged radial Poynting vectors at different propagation lengths corresponding to Fig. 32. In each plot, the vertical red line represents the extent of the ≈ **100 μm** filament. Power flow of the central beam by itself (a) before and (b) after collapse. Note that during self-focusing, power flows toward the center of the beam (negative values) while the opposite occurs after the collapse point (positive values). Computation of the power flow for the dress beam (c) before and (d) after the extended focus reveals that the dress beam's power monotonically flows inward and then monotonically outward respectively. (e,f) The power flow dynamics of the dressed filament are now more complex. Power primarily flows from the surrounding bath to the filament core during portions of the refocusing cycles dominated by self-focusing collapse, (e). On the other hand, when plasma defocusing is significant, power moves from the filament core to the surrounding energy reservoir, (f).

3.3.5. Experimental methods

The Gaussian and dress beam in the experimental setup were not phase-stabilized. The relative phase between the two beams fluctuated from one laser shot to another, due to air turbulence and other environmental factors in the laboratory. At each longitudinal location along the propagation path, the measurement of the plasma density was averaged over 100 laser shots, which effectively averaged out the fluctuations of the generated plasma due to the randomly varying phase between the two beams. By producing single- and multiple-shot burns at different points along the propagation path, we found that the resulting plasma generation was either enhanced or inhibited depending on whether the Gaussian filament and the dominant intensity peak of the dress wave were either in or out of phase. Furthermore, for each specific laser shot, the relative phase between the two beams undulated along the propagation direction, due to the difference in their phase velocities. The spatial period of this undulation is approximately given by $\Lambda \approx 8\pi^2/\lambda_0\delta^2$. In Fig. 36, we show examples of multi-shot burn patterns produced by the dressed laser beam when the Gaussian and dress pulses were out of temporal synchronization (left) and when the pulses were synchronized (right). When the two beams were not synchronized, they acted independently and produced two distinct partially overlapping burn spots. The displacement between the two spots is due to the less than ideal alignment between the beams. On the other hand, when the two beams were synchronized and locally interfered, the contribution of the laser shots with the two beams being locally in-phase produced an enhanced burn spot which appeared at the location of the main intensity peak of the dress beam. The shots with the two beams being out of phase produced a faint halo pattern that was scattered around the central dominant burn feature.
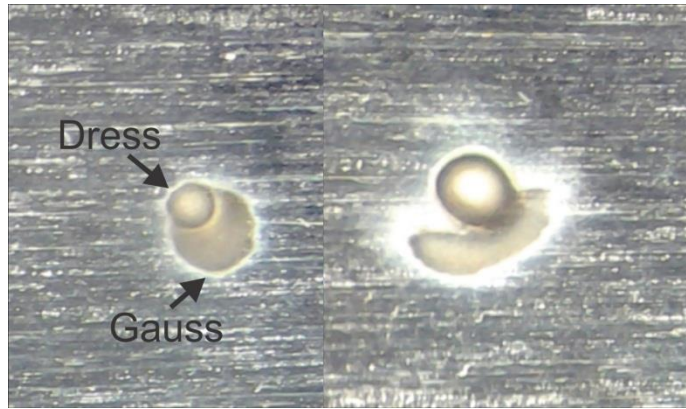
Figure 36| Multi-shot burn patterns produced by the Gaussian and dress beam on aluminum foil, when the two beams were out of temporal synchronization and acted independently (left) and when they were synchronized (right).

3.3.6 Plasma density distribution associated with a long-ranged dressed optical filament

In this section, we present additional data concerning Fig. 32. Fig. 37 displays the maximum plasma density vs. propagation distance for the four cases mentioned in that figure.
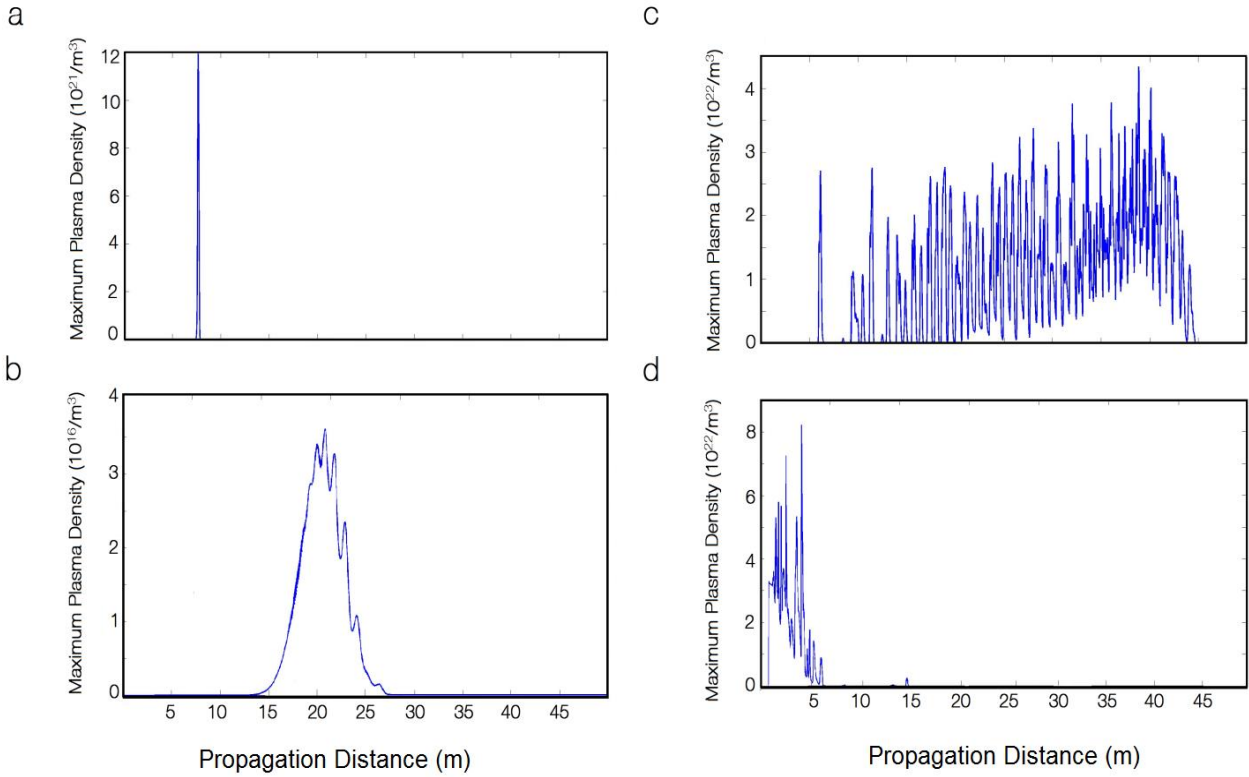
Figure 37| Maximum plasma density vs. propagation distance for the four cases presented in Fig. 32. (a) The central collimated beam containing 2 mJ. (b) The auxiliary dress beam containing 26 mJ of energy; note that in this case, the plasma density peaks $\approx 3 \times 10^{16} \ m^{-3}$ – this implies that no filament is formed. (c) The plasma density corresponding to a long-lived dressed filament. (d) The resulting maximum plasma density if all 28 mJ of available energy are packed into the primary Gaussian beam.

Figure 37(a) shows the main filament beam alone produces a single plasma density spike ($\approx 10^{22} m^{-3}$) at $2m$. On the other hand, Supplementary Fig. 37(b) shows a longer plasma channel resulting from the $26 \ mJ$ dress beam which is orders of magnitude below that typically seen during a filamentation process. In this case, plasma values peak around $3 \times 10^{16} \ m^{-3}$ which conveys that the dress beam does not itself form a filament. In a similar manner, Fig. 37(c) displays the plasma signature

of a 45 meter long dressed filament. If instead, all the available energy in this example is packed into a central Gaussian filament beam, the resulting plasma density channel is much shorter (Fig. 37(d)).

CHAPTER FOUR: DIFFERENT DRESS ARRANGMENTS

In this section, we theoretically expand on this idea of dressed filaments in air [85]. Along these lines, we simulate several types of auxiliary beams in order to identify regimes where the filament extension can be maximized for a given amount of available energy. These effects are examined by varying a number of pertinent parameters including the dress shape, width, and its inward radial chirp.

4.1. Overview of quasi-linear dress dynamics

A dress beam is specifically engineered so that during propagation, it gradually approaches the $\hat{z}$-axis while concurrently maintaining a relatively low intensity profile; as so, the wavefront replenishes the optical filament as needed and at the same time evolves in a quasi-linear fashion. For simplicity, if we assume continuous wave conditions, the slowly varying envelope of the associated dress-field component, ψ_D, satisfies the paraxial wave equation:

$$i2k_0\partial_z\psi_D + \nabla_\perp^2\psi_D = 0. \tag{56}$$

Where here $k_0 = 2\pi\lambda_0^{-1}$. The envelope of this auxiliary beam can be described in terms of its initial profile at any arbitrary propagation distance through a Fresnel diffraction integral:

$$\psi_D(x, y, z) = \frac{1}{i\lambda_0 z}\iint_{-\infty}^{+\infty}\psi_D(x', y', z = 0)$$

$$\times \exp\left(\frac{ik_0}{2z}[(x - x')^2 + (y - y')^2]\right)dx'dy'. \tag{57}$$

By narrowing our attention to wavefronts only exhibiting azimuthal symmetry, this expression can now be written in cylindrical coordinates as follows:

$$\psi_D(r,z) = \frac{2\pi}{i\lambda_0 z} \exp\left(\frac{ik_0}{2z} r^2\right) \int_0^\infty \psi_D(r', z = 0) J_0\left(\frac{k_0 r}{z} r'\right) \exp\left(\frac{ik_0}{2z} r'^2\right) r' dr'. \qquad (58)$$

To illustrate this effect, we choose a dress wave that has the form of a radially chirped Gaussian ring (Fig 38a):

$$\psi_D(r', z = 0) = \sqrt{2\eta_0 I_0} \exp\left(-\frac{(r' - r_0)^2}{w_D^2}\right) \exp(-i\delta r') \qquad (59)$$

Here, $\sqrt{2\eta_0 I_0}$ is the peak electric field strength, δ represents the inward linear spatial chirp, r_0 is the ring radius of this beam, w_D is the field's half-width, and $\eta_0 \approx 120\pi \ \Omega$. The negative spatial chirp term, δ, is essential in refuelling the optical filament since it dictates the rate at which the auxiliary beam gently approaches the propagation axis. As an example, consider a Gaussian ring-dress with $r_0 = 6 \ mm$, $w_D = 1 \ mm$, and $\delta = 21 \ mm^{-1}$. For these parameters, the dress feeds the on-axis filament from approximately $z = 1.2 \ m$ to $z = 2.5 \ m$ (Fig. 38b). Upon inspection, the full width at half maximum of this high intensity region is about $2 \ mm$ (Fig. 38c) which is approximately 20 times larger than the diameter of a filament in air at $\lambda_0 = 800 \ nm$. Therefore, the dressed filament configuration is able to tolerate appreciable displacements of the original filament from the center of the annular dress.
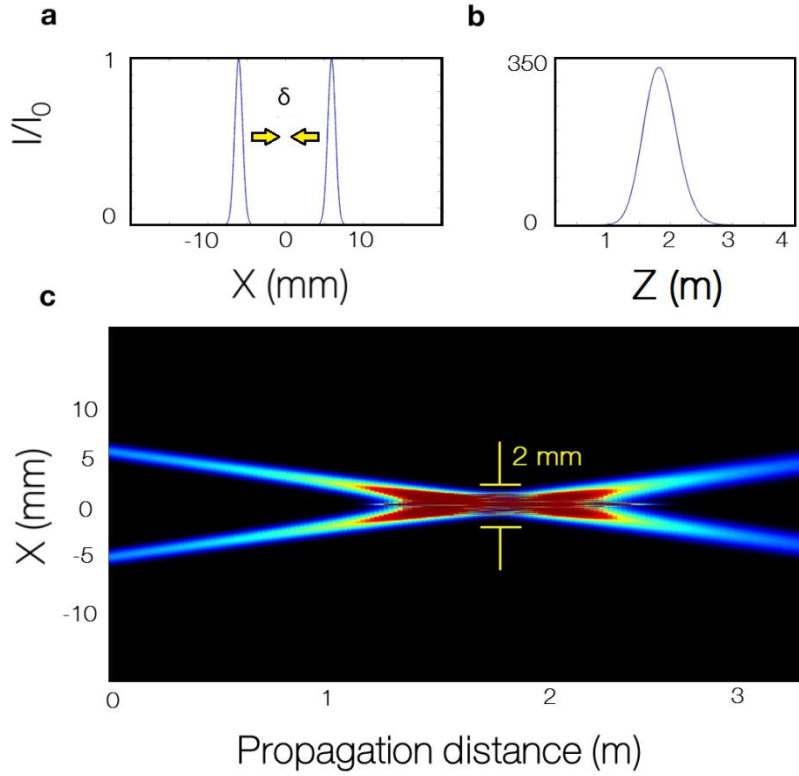
Figure 38| (a) A cross section along $Y = 0$ of a radially symmetric optical dress, $\psi_D(r, t = 0, z = 0)$, with $r_0 = 6\ mm$, $w_D = 1\ mm$, and $\delta = 21\ mm^{-1}$. (b) The negative spatial chirp causes the on-axis intensity to ramp up at a specific distance along the propagation axis; the value of δ must be chosen such that it prudently refuels its co-propagating beam (central beam not displayed here). (c) Propagation dynamics of the dress beam reveals an interaction region which is much larger than the $\sim 100\ \mu m$ filament. This property makes the dress beam robust to off-axis displacements. All values are scaled with respect to the maximum intensity of the initial dress beam, I_0.

4.2. Filaments surrounded by Gaussian rings

As a first case, we examine the filamentation dynamics resulting from a filament when surrounded with an auxiliary Gaussian spatially chirped ring. In this arrangement, the total electric field envelope can be written as follows:

$$\psi_{DF} = \sqrt{2\eta_0 I_F} \exp\left(-\frac{r^2}{w_F^2} - \frac{t^2}{\tau_F^2}\right) + \sqrt{2\eta_0 I_D} f(r) \exp\left(-\frac{t^2}{\tau_D^2} - i\delta r\right) \qquad (60)$$

Here, I, w and τ represent the peak intensity, beam waist, and pulse duration of the filament and dress beams respectively. The latter of these two wavefronts is set to have a radially symmetric Gaussian shape, $f(r) = \exp[-(r-r_0)^2/w_D^2]$. Consider, for now, two unaided filament beams having different peak intensities but identical parameters otherwise: $I_{F1} = 1 \times 10^{16} \, W/m^2$, $I_{F2} = 4 \times 10^{16} \, W/m^2$, $w_F = 1 \, mm$, and $\tau_F = 50 \, fs$. These wavefronts contain $E_F = 1 \, mJ$ and $E_F = 4 \, mJ$ of energy respectively and produce a $z_{f1} = 1 \, m$ and $z_{f2} = 2.5 \, m$ long filament after its initial collapse (Fig. 39 a,b). Note that the 4 mJ unaided filament in (b) prematurely collapses within the first meter and squanders its available energy. If, however, the 1 mJ beam is wrapped with a $E_D = 3 \, mJ$ Gaussian dress given by $f(r) = \exp[-(r-r_0)^2/w_D^2]$ with $I_D = 2.5\% I_F$ $w_D = 3 \, mm$, $\tau_D = 50 \, fs$, $r_0 = 8 \, mm$, and $\delta = 10 \, mm^{-1}$, a 5m filament occurs (Fig. 39c). For these parameters, the peak/critical power ratios contained in the two terms of Eq. (60) are $P_F/P_{crit} = 6.5$ and $P_D/P_{crit} = 20$.
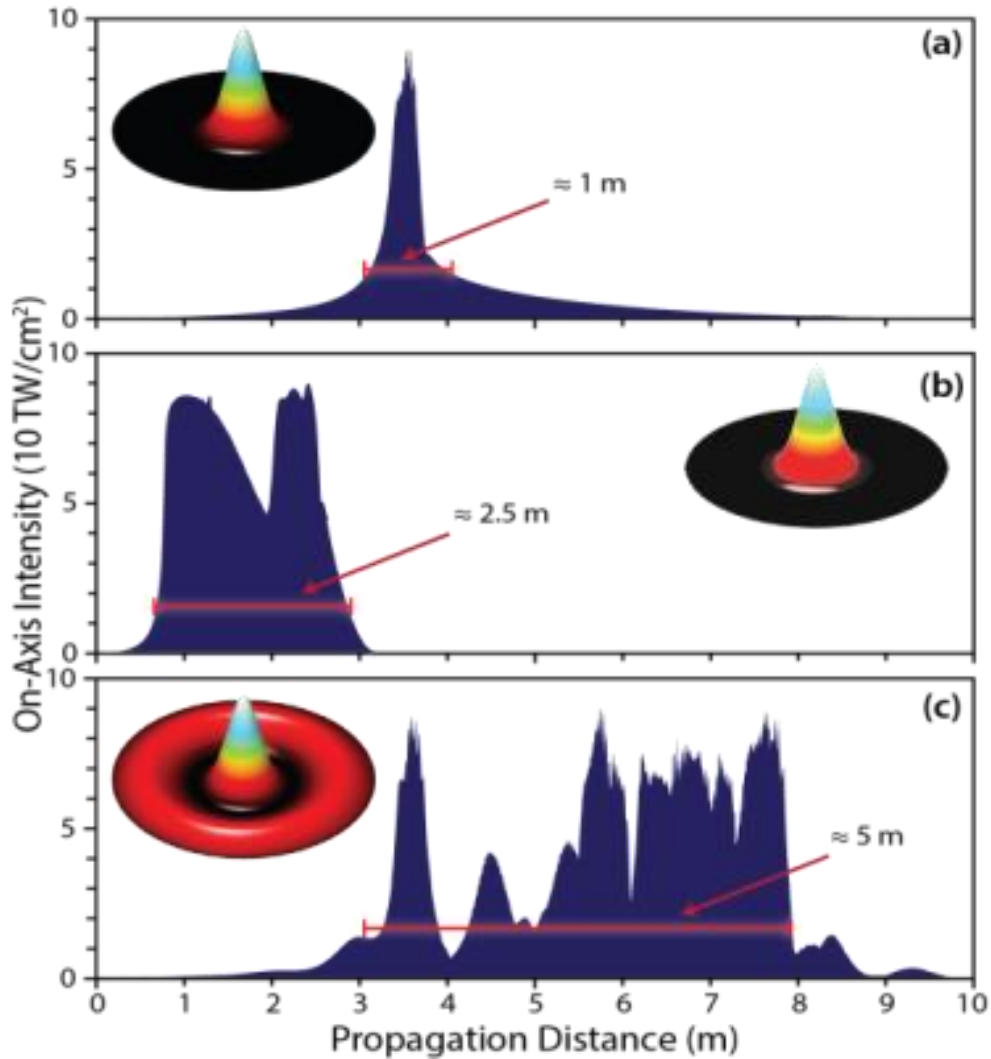
Figure 39| An accompanying optical dress significantly protracts longevity of a filament. (a,b) Two Gaussian beams (see insets) with $E_{F1} = 1\ mJ$, $E_{F2} = 4\ mJ$ $w_F = 1\ mm$, $\tau_F = 50\ fs$, $I_{F1} = 1 \times 10^{16} W/m^2$, $I_{F2} = 4 \times 10^{16} W/m^2$ form a **1 m** and 2.5m long filament respectively. (c) If the beam in (a) is wrapped with a Gaussian shaped optical dress (see inset) with $E_D = 3\ mJ$, $I_D = 2.5\% \cdot I_F = 2.53 \times 10^{14}\ W/m^2$, $r_D = 8\ mm$, $w_D = 3\ mm$, $\delta = 10\ mm^{-1}$, the filament extends to 5m.

As illustrated in Fig. 39, it is apparent that an accompanying dress beam increases the longevity

of an optical filament [86]; however, it is natural to ask: does it do so in the most efficient way? In other

words, are there comparable dress configurations which perform better given the same amount of input

power? There are several parameters that can be varied in this respect. Here, we will explore the impact of dress width, inward radial chirp, and dress shape.
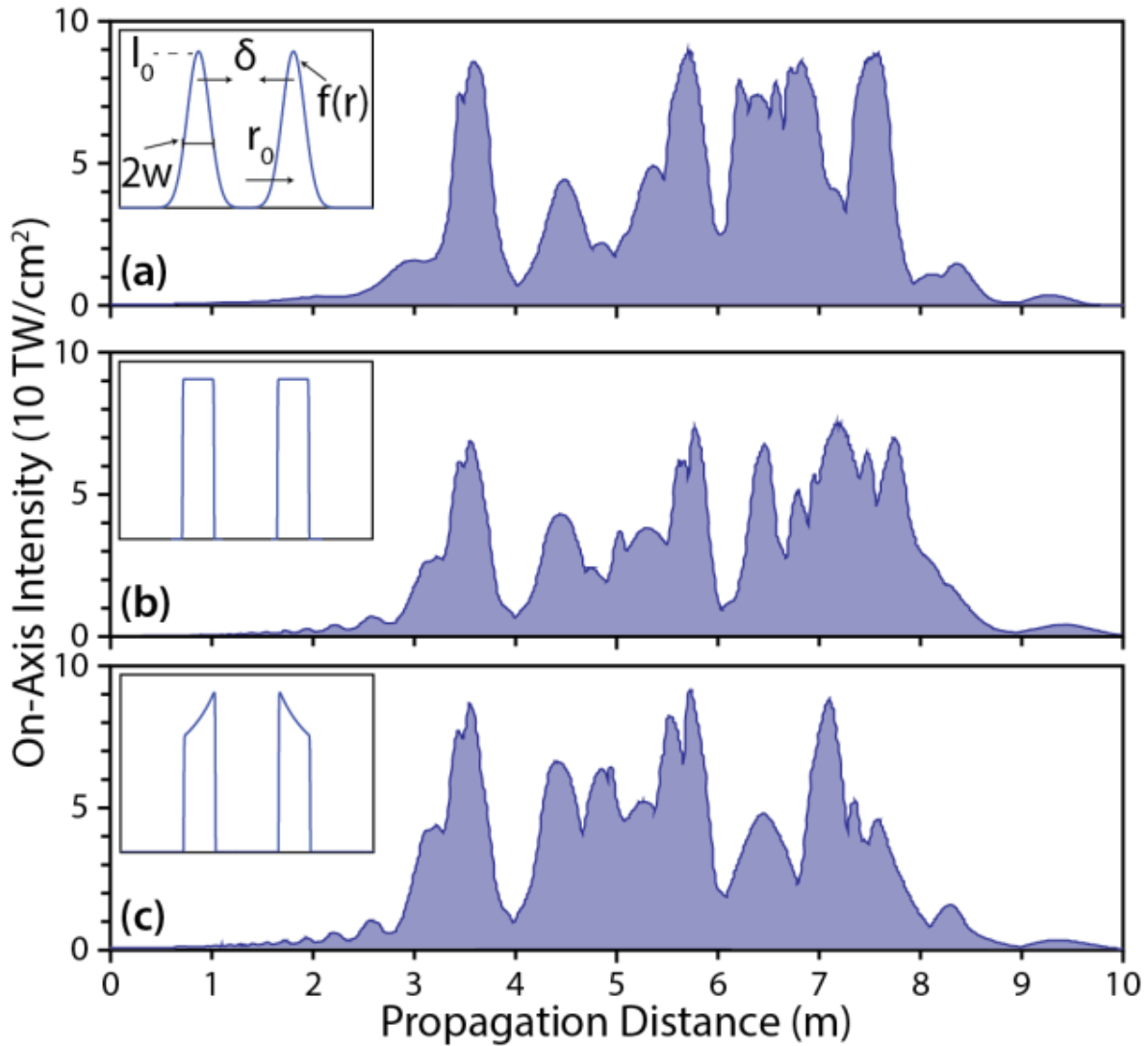
Figure 40| Dressed filaments containing the same energy, $E_{DF} = 4\ mJ$, dress width, $w_D = 3\ mm$, dress radius, $r_0 = 8\ mm$, and inward radial phase, $\delta = 10\ mm^{-1}$, but with different dress shapes, $f(r)$. Although the different initial arrangements (see insets) affect the occurrence of the intensity spikes, no significant filament prolongation is observed. (a) A Gaussian dress; (b) A step dress; (c) A step dress with an $r^{-1/2}$ dependence.

4.3. Different spatial dress shapes

In this section, we simulate two different dress shapes, $f(r)$, while keeping all other parameters identical to those used in the previous Gaussian dressed filament (Fig. 3). The extensions are then juxtaposed next to the Gaussian dressed filament (Fig. 40a). As an alternative dress, we use a step-like ring beam (Fig. 40b), which is described by a revolved rectangular function, $f(r) = rect([r - r_0]/w_D)$. In addition, we also investigate the same dynamics when this same auxiliary beam drops as $r^{-1/2}$; i.e. $f(r) = \sqrt{r_0/r} \cdot rect([r - r_0]/w_D)$ (Fig. 40c).

One would be inclined to think that the step dress arrangement would behave poorly because as the energy flows inward toward the axis, the steep edges suddenly combine causing a sharp increase in intensity. This could lead to wasted energy and inefficient coupling between the two wavefronts. However, as seen in Fig. 40b, this is no so the case. Even in this situation, we observe considerable protraction of the filament that seems to be impervious to the radial shape of the secondary beam. To some extent, these results indicate that the refuelling process happens to be robust and is relatively insensitive to the way power is distributed around the filament itself.

Similar results are also obtained for a wavefront whose intensity falls as r^{-1} ($I_{DF} \propto |\psi_{DF}|^2$) as depicted in Fig. 40c. In this scenario, the power flow towards the axis of the filament happens to be more uniform during propagation since the amount of power contained in any radially symmetric auxiliary wavefront is always proportional to the radius. Yet, as the three cases in Fig. 40 display, the shape of the dress only affects the intensity variations that occur during the refocusing cycles. In fact, when all other parameters are kept the same, the specific spatial shape of the dress does not significantly affect filament extension.

4.4. Different widths and radial chirps

The focusing term, $\exp[-i\delta r]$, which appears in equation (60), describes the spatial chirp needed to refuel the filament. It has to be judiciously chosen in such a way so that the auxiliary beam accompanies the filament in both space and time within a certain propagation range. The required angular tilt can be easily estimated using a ray approach (see Fig. 41).
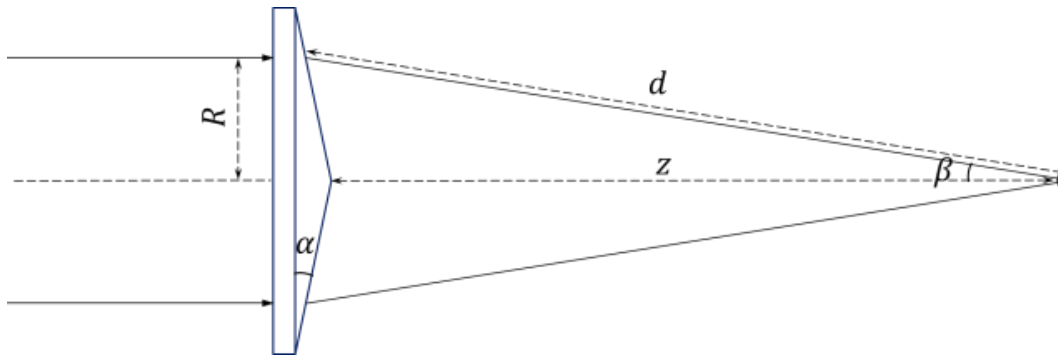
Figure 41| Ray diagram of collimated light entering an axicon

As seen in Fig. 41, after passing through an axicon, the depth of focus is given by $z = R/\beta$ where R is the radius of the axicon and $\beta \approx \delta/k_0$ represents the focusing angle which is related to the shallow angle of the axicon, α, via $\beta = \alpha(n-1)$. Our simulations assume auxiliary beams with a large diameter, $r_0 = 8\ mm$ and $w_D = 3\ mm$, which needs to approach the axis after roughly $z = 3\ m$ of propagation. This requires an inward radial chirp of $\delta \approx 10\ mm^{-1}$. The geometry of this arrangement also leads to a temporal walk-off between the two wavefronts, $\Delta t \approx \alpha\beta/2c$. Assuming a very shallow glass ($n = 1.45$) axicon bending angle, $\beta \approx .153°$, a small walk-off of $\Delta t \approx 26\ fs$ is expected. Note that the efficacy of the resulting filament further improves in long-ranged scenarios. In principle, these beams can propagate over one hundred meters when appropriate collimating optical systems are used.
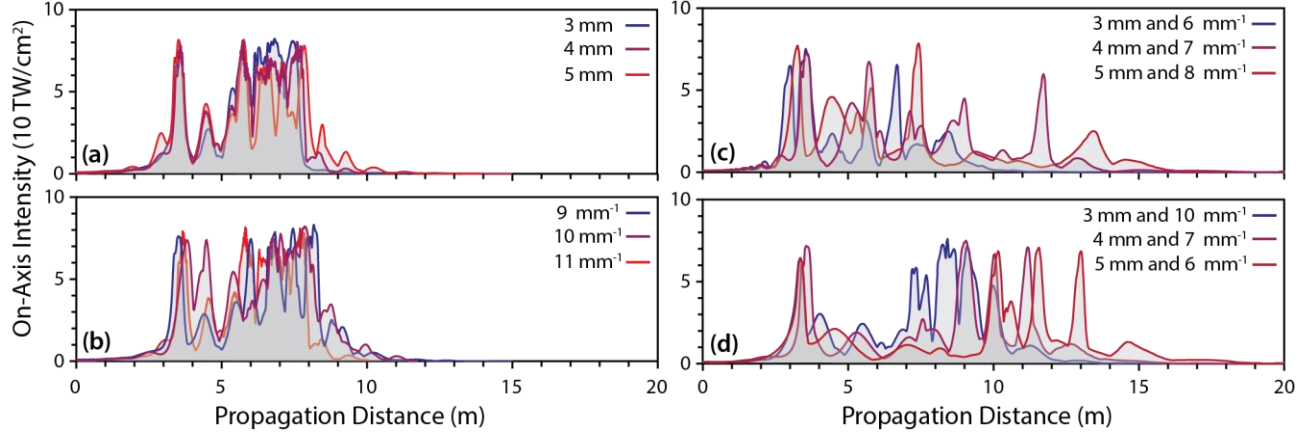
Figure 42| Several dressed filaments realizations in which the dress width, w_D, and inward radial chirp, δ, are varied. For each case, the energy ($E_{DF} = 4\,mJ$), dress radius ($r_0 = 8\,mm$), and dress shape (Gaussian-ring) are held constant. (a). Comparison of three different dress widths each chirped with $\delta = 10\,mm^{-1}$. (b) Similar comparison but with varied inward radial chirps; each dress has $w_D = 3\,mm$. (c) Increasing dress widths in conjunction with higher spatial chirp results in considerable filament extension. (d). Increasing dress width while decreasing inward focusing results in the longest possible filaments. In all cases, the filament and the auxiliary beam contain $E_F = 1\,mJ$ and $E_D = 3\,mJ$ of energy respectively. Quantities measured in mm represent dress widths while those in mm^{-1} spatial chirps.

By assuming an inward chirp of $\delta = 10\,mm^{-1}$, we now investigate how the width of the secondary beam could affect filament prolongation (Fig. 5a). Note that in order to compare equal-energy dress beams, an increase/decrease in dress width will always be accompanied by a necessary decrease/increase in the peak intensity. Additionally, for each case we explore in this section, we use the Gaussian-ring spatial profile, and we assume $\tau_D = 50\,fs$, $r_0 = 8\,mm$, and $w_D = 3\,mm$.

Fig. 5a displays the on-axis intensity of three dressed filaments differing only in width. Although the total filament length increases by about a meter as the size of the dress is enlarged from $w_D = 3\,m$ to $w_D = 5\,mm$, the amount of extension is not that noticable. Fig. 5b illustrates a similar finding. However, when both values are appropriately adjusted together, significant extension occurs (Fig. 5c and 5d). Fig. 5c illustrates that a broader dress will perform better if the inward chirp is shallow enough to allow for extended on-axis interaction but at the same time sharp enough to focus the dress on-axis when needed. Fig. 5d, on the other hand, shows that a broader dress accompanied by an ever decreasing radial chirp will

also continue to extend the filamentation length as long as the overlap between the two wavefronts is maintained. With $r_0 = 8\,mm$, a dressed filament with $E_D = 3\,mJ$ of energy results in a fifteen-fold extension; this greatly exceeds the five-fold prolongation achieved with the standard case.

4.5. Different dress conclusions

While the quasi-linear propagation dynamics of the auxiliary dress can be readily predicted through a Fresnel diffraction integral, this is not the case when it refuels a filament.

In our example, a $1\,m$ long unaided filament was able to propagate $5\,m$ when a suitable yet un-optimized Gaussian-ring beam was appended. Even in the case when all $4\,mJ$ of energy was packed into the main beam, the wavefront prematurely collapsed and only propagated for $2.5\,m$. In general, we found that changing the spatial distribution of the auxiliary beam had little effect on the filament elongation. A possible explanation for this is as follows: the filamentation process is known to continue as long as the power contained within the primary beam is above the critical power required for self-focusing to dominate. Ideally, the spatial dress shape should be moulded in such a way that the power flow toward the axis is constant throughout propagation – keeping the system above the critical threshold. As such the process is becomes relatively insensitive to the shape itself and as a result no significant improvement is observed. On the other hand, significant improvement can be observed whenever the dress width is prudently adjusted with the spatial chirp as clearly shown in Figs. 5c and 5d.

In summary, we found that both the beam width and inward radial chirp, when judiciously adjusted in unison, play a crucial role in maximizing the range of a dressed filament. On the other hand, the spatial shape of the dress beam only affects the characteristic intensity fluctuations seen during refocusing cycles. Our results indicate that this process is robust to the distribution of power within the dress beam.

CHAPTER FIVE: SUPERCONTINUUM GENERATION IN PARABOLIC MULTIMODE FIBERS

In recent years, ultra-short pulses have paved the road to laser light which can boast both an expansive and continuous spectrum. First observed in borosilicate glass [87], it is now known that an expansive white-light spectrum or "supercontinuum" can be generated in a large variety of materials and structures [88-95]. Along these lines, a platform of particular interest is the production of supercontinuum in optical fibers such as chalcogenide based [96, 97] or photonic crystal fibers [93, 98]; to this end, focus is beginning to accumulate around the relatively unexplored territory of nonlinear multimode fibers [99-101]. Currently, simulations which describe optical propagation in nonlinear multimode fibers are done by isolating the evolution of a specific spatial mode, creating a time-dependent PDE describing its motion, and then coupling this to the evolution of the other existing spatial modes via nonlinear overlapping terms [102]. However, for highly multimoded fibers, this approach quickly becomes a cumbersome, nay impossible, bookkeeping task, and only a few modal profiles can be reasonably followed [103]. This immediately restricts the study of any situation where multimode interactions are a significant ingredient.

5.1. Simulation parameters for silica glass multimode fibers

In this section, we explore supercontinuum generation in a highly multimode graded index silica glass fiber using the numerical scheme introduced in the filamentation chapters, the Unidirectional Pulse Propagator (UPPE). We now recall its form:

$$\partial_z \vec{E}(k_\perp, \omega, z) = +ik_z \vec{E}(k_\perp, \omega, z) + \frac{i\omega^2}{2\epsilon_0 c^2 k_z} \vec{P}(k_\perp, \omega, z) - \frac{\omega}{2\epsilon_0 c^2 k_z} \vec{J}(k_\perp, \omega, z) \qquad (61)$$

This method allows us to fully incorporate the effects of the approximately 200 possible spatial modes into the analysis [82, 104]. For the task at hand, the UPPE core is primed to account for several nonlinear

phenomenon such as self-phase modulation (SPM), four-wave mixing, third harmonic generation, shock-effects, and the Raman-Kerr effect with nonlinear fraction, $f = 0.18$, index, $n_2 = 2.9 \times 10^{-20} m^2/W$, and oscillation period $\tau = 32\,fs$ [105].

In our numerical computations, we model a silica glass fiber having a core radius of $a = 62.5\,\mu m$ and excite it in the anomalously dispersive regime using $\lambda = 1550\,nm$ light. The sizable transverse area of the fiber permits a high spatial mode count on the order of $N \approx V^2/4 = 240$ modes. Here, $V = k_0 a(NA_{max}) \approx 31$, is the "$V$-number" figure of merit ascribed to optical fibers which depends on the maximum numerical aperture, $NA_{max} = \sqrt{n_c^2 - n_{cl}^2} = .122$. Our simulations always assume a dispersion coefficient of $\beta'' \approx -28\,fs^2/km$ at $\lambda = 1550\,nm$ [100], account for the wavelength dependent index via Sellmeier curves, and include any absorption effects through an imaginary susceptibility.

In our case, the refractive index of the graded fiber is subject to the following law:

$$n(r) = \begin{cases} n_c\sqrt{1 - 2\Delta(r/a)^{\gamma}} & r \leq a \\ n_{cl} = n_c\sqrt{1 - 2\Delta} & r \geq a \end{cases} \tag{62}$$

Where $n_c = 1.501$ and $n_{cl} = 1.496$ are the indices of the fiber core and cladding and γ is a free parameter which adjusts the radial taper of the graded-index (Fig. 43a). In general, the time it takes for a mode with a specific group velocity, v_g, to travel a certain distance, L, is given by

$$t = \frac{L}{v_g} = \frac{L}{c}\frac{d\beta}{dk} \tag{63}$$

Here, c is the speed of light, and $d\beta/dk$ is the change in a mode's propagation constant, β, with wavenumber, k. If the refractive index is given by Eq. 62, the propagation constant is intricately dependent on the wavenumber [106]:

$$\beta = kn_c \left(1 - 2\Delta \left\{ 1 - \frac{\left(\frac{\beta}{k}\right)^2 + n_{cl}^2}{n_c^2 - n_{cl}^2} \right\} \right) = n_c(1 - 2\Delta\Gamma) \tag{64}$$

The parameter, $\Delta = (n_c^2 - n_{cl}^2)/2n_c \approx 0.5\%$, defines how shallow the contrast is between the core and cladding indices and the symbol Γ is simply meant to be a placeholder for the expression inside the curly brackets. After substituting Eq. 64 into Eq. 63 and Taylor expanding in Δ, we obtain an expression for the walk-off between modes:

$$t = \frac{L}{c} n_{group} \left[1 + \frac{\gamma - 2 - y_d}{\gamma + 2} \Gamma + \frac{3\gamma - 2 - 2y_d}{2\gamma + 4} \Gamma^2 \Delta^2 + O(\Delta^3) \right] \tag{65}$$

Where $y_d \propto \lambda \Delta^{-1} d(\Delta)/d\lambda$, is a characteristic parameter. Note that the second term can be best minimized by when the refractive index taper is $\gamma = 2 + y_d$. For our test-bed situation, we choose the case of a parabolic graded-index fiber, $\gamma \approx 2$, because it indeed significantly minimizes the unwanted walk-off that occurs between each transverse mode (Fig. 43b) [107]. Such a profile supports transverse modes which follow Laguerre-Gauss functions:

$$N_{lm} r^\ell \exp\left[-\frac{1}{2} \gamma^2 r^2 \right] L_{m-1}^\ell (\gamma^2 r^2) \exp(i\ell\theta) \exp(i\omega t - i\beta z) \tag{65}$$

Where $r^2 = x^2 + y^2$, $\theta = \text{atan}(y/x)$, $N_{\ell m}$ is a normalization constant, and L_{m-1}^ℓ is the associated Laguerre polynomials of integer spin order $\ell = 0,1,2,...$ and radial order $m = 0, 1, 2$, etc.
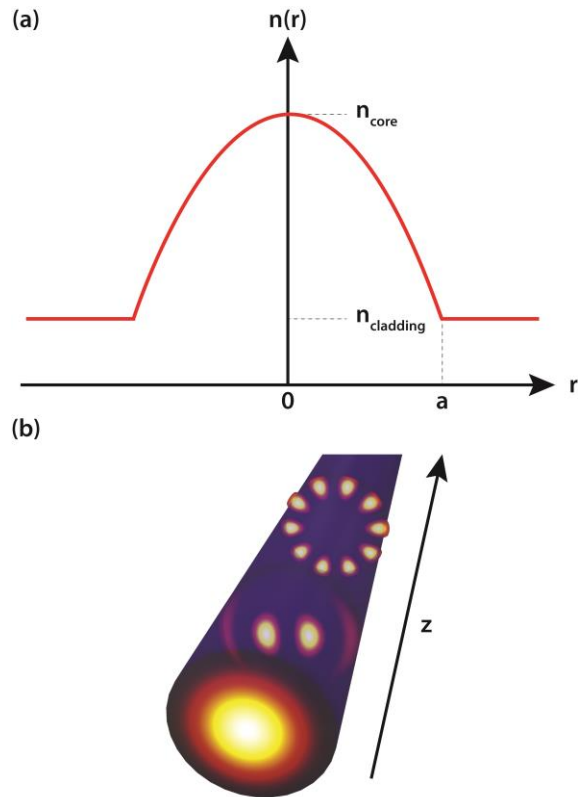
Figure 43| (a) Graded index profile represented by Eq. (1) with $\gamma \approx 2$. (b) For a parabolic fiber, the walk-off amongst the spatial modes excited at the input of the fiber is minimized.

5.2. Example supercontinuums in parabolic silica fibers

Supercontinuum generation is a result of a conglomeration of multiple nonlinear effects which act upon each other in a cascading-like way. For example, a new frequency which sprung forth from Raman-scattering could later find itself phased matched in a four-wave mixing process leading to yet another produced color. Although there are many aspects that contribute to the complex evolution of these highly nonlinear spectra, several parameters, such as the material in use, gently constrain the supercontinuum to a specific form.

Take for example, a $400 \, fs$ Gaussian spatio-temporal wavefront containing $150 \, nJ$ of energy and spatial $FWHM$ of $30 \, \mu m$. Simulations of such a beam show that it quickly invokes several of the

mentioned nonlinear effects. In fact, after only $z = 10\ cm$ of propagation, several features in the spectrum including frequencies caused by Raman scattering (RS) and pump dispersive waves (PDW) begin to appear (Fig. 44a). By $z = 20\ cm$ of propagation, these features have become more defined and the appearance of peaks stemming from third harmonic generation (THG) and Raman scattering induced dispersive waves (RSDW) are present.
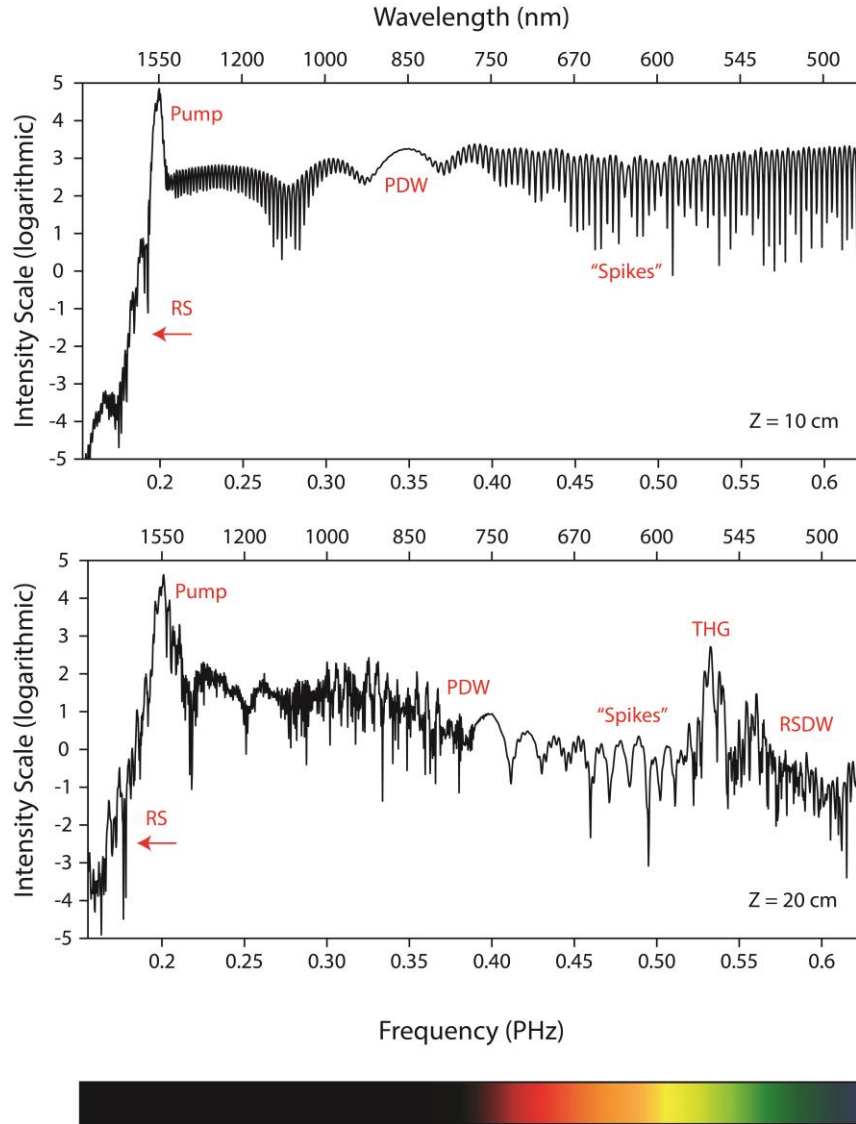
Figure 44| (a) Launching a $E = 150\ nJ$ on-axis Gaussian beam into the parabolic fiber quickly begins to form several distinct spectral features. After only $z = 10\ cm$ of propagation, the formation of Raman lines (RS), pump dispersive waves (PDW), and sharp visible color spikes begin to form. (b) By $z =$

20 *cm* of propagation, these characteristics have become well-defined, and new features have now appeared including a peak caused by third harmonic generation (THG) and another dispersive wave originating from RS (RSDW).

However, if the simulation results of Fig. 44 are rerun with fourfold energy, the general shape of the spectrum at $z = 20\ cm$ appears similar yet much more uniform and with specific features washed out (Fig. 45). This is because the increased energy allows for more and more nonlinear interactions within the fiber – opening up opportunities for each and every frequency.
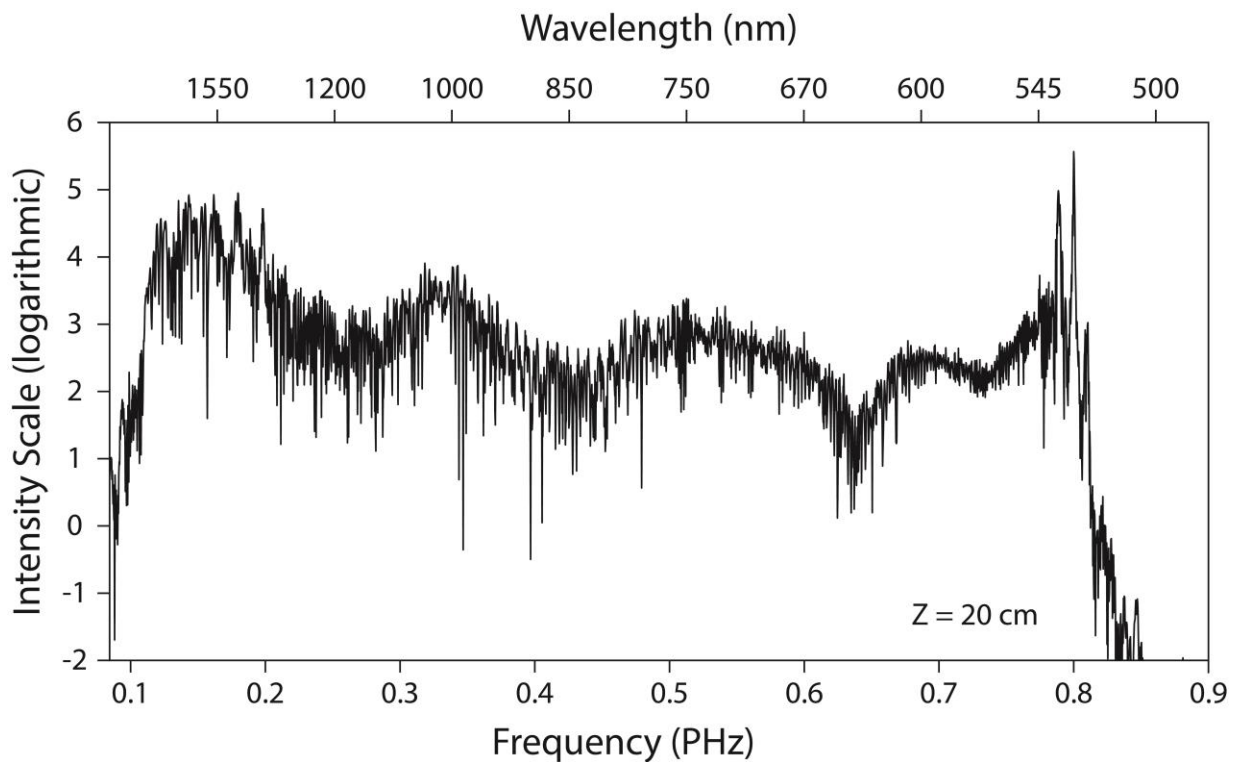
Figure 45| Spectrum after $z = 20\ cm$ of propagation for a high energy $E = 600\ nJ$ on-axis Gaussian beam.

Yet one should take note that regardless of the nonlinear interactions, the spread of the supercontinuums in both Fig. 44 and Fig. 45 are approximately the same. This is because the material of choice, in this case silica glass, contains absorption peaks which essentially forms a bandpass area for the frequencies.

Regardless of the fact that constraints may exist on the generation of supercontinuum for a given material, of interest will be to study ways of controlling the other exigent features.

5.3. Versatile supercontinuum generation stemming from different initial spatial conditions

Equipped with Eq. 61 and the previously mentioned parameters, we simulate four different initial nonlinear excitations of the fiber core and then examine the resulting changes that occur in both the spatial and spectral domains.

We first blast, on-axis, the front facet of the fiber with a $E_{in} \approx 400 \, nJ$ space-time Gaussian of pulse width $\tau = 300 \, fs$ and radial e^{-2} size of $w = 20 \, \mu m$. This illuminates a localized portion of the fiber with radiation setting into motion a rapidly expanding supercontinuum. In fact, after only about $z = 4 \, cm$ of propagation, wavelengths ranging from the mid infrared to the visible are present; considering a $20 \, dB$ dynamic range (not including pump height), the resulting supercontinuum already spans beyond one octave (Fig. 46a)

Extracting the spectral content within the fiber after $z = 8 \, cm$ of propagation, we find that it is rich with unique features (Fig. 46b). As mentioned before these include the existence of pump side-peaks from Raman-scattering (RS), an accelerating dispersive wave emitted by the pulse (PDW), the creation of several quasi-equally spaced "spikes" around the red portions of the spectra (postulated to originate from periodic changes in the nonlinear refractive index during propagation [108]), a strong peak whose origins are due to third harmonic generation (THG), and yet another dispersive wave springing forth from Raman-scattering (RSDW).
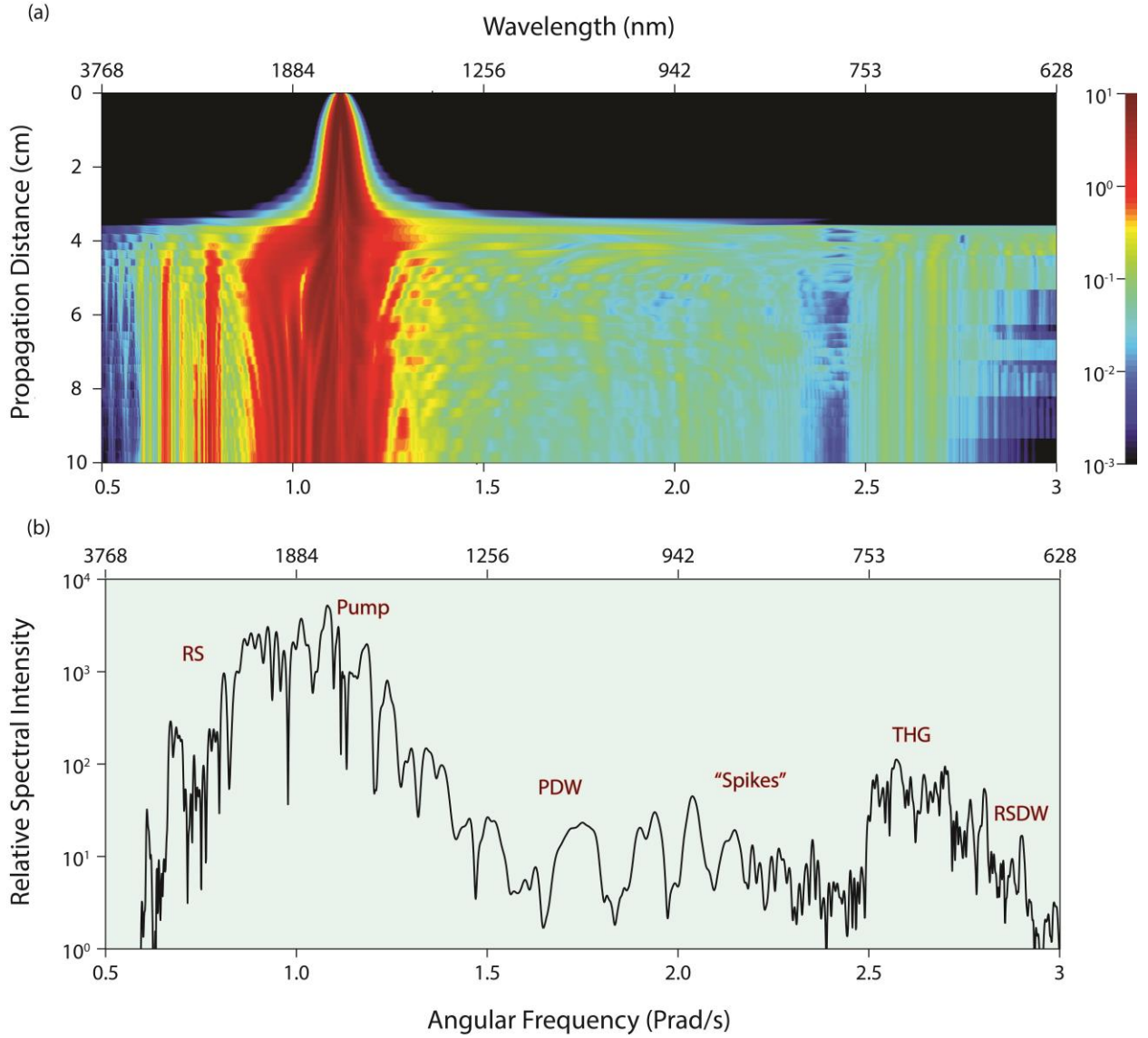
Figure 46| (a) An expansive supercontinuum forms in a highly multimode silica glass fiber after only $z = 4\ cm$ of propagation. In this case, the fiber core was incited with a $\tau = 400\ fs$ pulse at $\lambda_0 = 1550\ nm$, and the relevant material parameters are: $a = 62.5\ \mu m$, $n_c = 1.501$, $n_{cl} = 1.496$. (b) Viewing a cross section of the integrated spectrum at $z = 8\ cm$ reveals a host of features including: pump dispersive waves (PDW), raman-scattering peaks from both the pump and dispersive waves (RS and RSDW).

In general, our numerical results are consistent with past explorations of nonlinear silica glass fibers [98, 99]. Yet, as mentioned earlier, it should be noted that these highlighted nonlinear characteristics appear even when using single mode fibers as these salient features are primarily set in

86

motion by SPM and Raman-scattering [109]. Our interest, however, will be to see how this abundant spectrum changes when different initial fiber excitations are tried. This is to say: equipped with the ability to aggregate the activity of the approximately 240 modes, how will exciting different amounts of them affect the supercontinuum?

Keeping the total energy, pulse width and center wavelength the same as before, we excite the parabolic silica fiber with the following general initial condition:

$$\psi(x,y,t;z=0) = \sqrt{2\eta_0 I_0} \exp\left[-\left(\frac{(x-x_0)^2 + (y-y_0)^2}{w}\right)\right] \exp\left[-\frac{t^2}{\tau^2}\right] \tag{66}$$

Where I_0 is the max intensity, $\eta_0 \approx 377\ \Omega$, x_0 and y_0 are beam offsets, and w is the transverse spatial width. Recalling the test bed case displayed in Fig. 46, we had a circular, $w = 20\ \mu m$ Gaussian beam on axis, $x_0 = y_0 = 0$. Transverse spatial profiles viewed at $\Delta z = 2\ cm$ intervals show an oscillating radially symmetric pattern throughout propagation (Fig. 47a). When the same beam is launched slightly off-axis, $y_0 = 30\ \mu m$, the modal composition becomes more complicated and no longer retains radial symmetry (Fig. 47b). Then, using similar values, two beams containing $200\ nJ$ each with offsets $x_0 = \pm 30\ \mu m$, are launched revealing even more diverse evolutions (Fig. 47c). Finally, a ring beam with offset $r_0 = \sqrt{x_0^2 + y_0^2} = 20\ \mu m$ and width $w = 20\ \mu m$ is launched giving rise to complicated superpositions of LP_{0m} modes. It is curious to note that in every case, a certain condensed spot appears quite often near the center of the fiber; this feature can be seen easily throughout Fig. 47 and is a harbinger for optical rogue events.
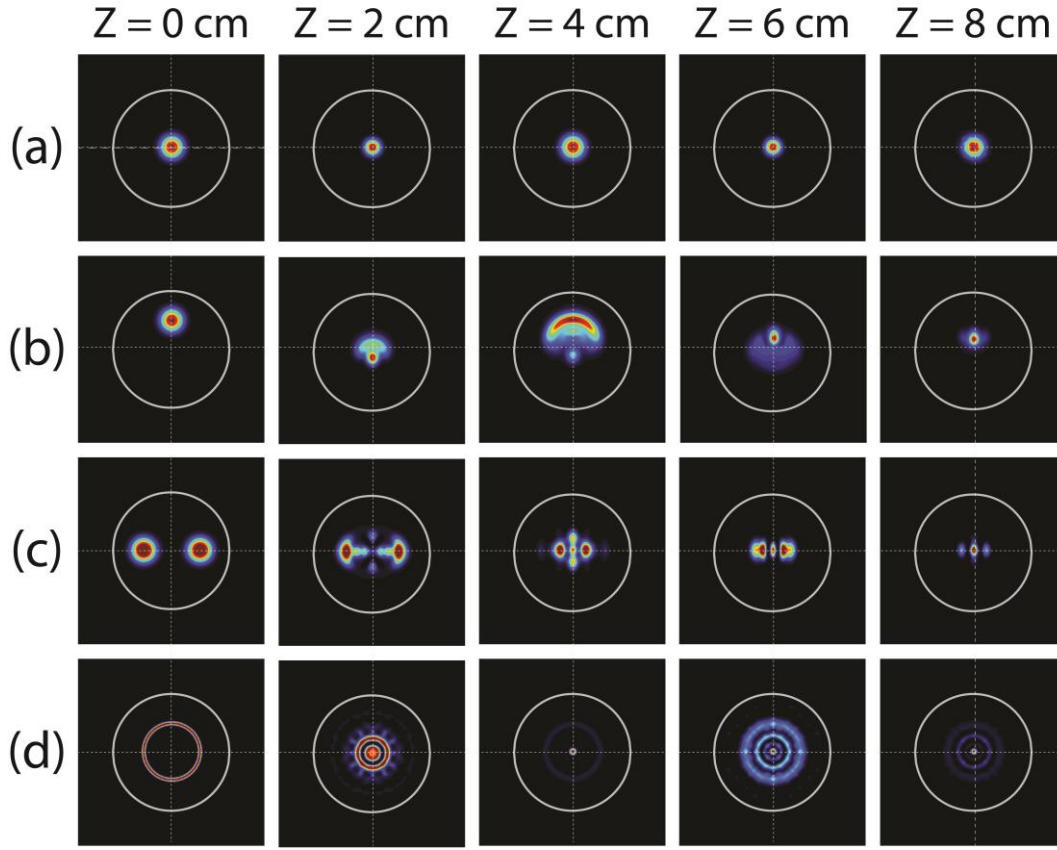
Figure 47| Radial cross-sections (along $T = 0$) at several propagation distances for four different initial spatial conditions. The white outline in each highlights the fiber's core. All inputs contain $400\,nJ$ of energy. (a) Evolution of a radially symmetric on-axis Gaussian beam of width $w = 20\,\mu m$. (b) This same beam but offset in the $\hat{y}$ dimension by $y_0 = 30\,\mu m$. (c) Two off-axis Gaussian beams with $x_0 = \pm 30\,\mu m$ containing $200\,nJ$ each. (d) Ring beam with $r_0 = \sqrt{x_0^2 + y_0^2} = 20\,\mu m$ and width $w = 20\,\mu m$.

It is plain to see from the evolution of the wavefronts in Fig. 47, that the slightest change in the wavefront's initial spatial conditions leads to entirely different sets of multi-wavelength modal combinations. More importantly, because all other parameters are strictly kept identical, any modifications which develop in the spectra will be solely attributable to multimode effects. In Fig. 48a, the integrated spectra at $z = 8\,cm$ for each of the scenarios presented in Fig. 47 are juxtaposed. For practical purposes, a dynamic range of four orders of magnitude are displayed in order to highlight the main features of each supercontinuum. Fig. 48a conveys that by simply altering the initial spatial

conditions of the beam, the distribution of wavelengths within the supercontinuum changes drastically. For example, an on-axis Gaussian beam (Fig. 47a) produces a large amount of radiation at $\lambda = 2\ \mu m$ whereas by simply splitting the beam into two pieces (Fig. 47c), that same energy becomes allocated in the shorter wavelengths. Although a myriad of differences can be extracted from Fig. 48a, the finer details concerning the processes responsible can be deciphered by plotting the difference between any two spectra. Fig. 48b shows one such result by subtracting the on-axis integrated Gaussian supercontinuum with the off-axis one. The interesting aspects of Fig. 4b occur in the sections where the features are not rapidly oscillating (three sections labeled on the plot). In this example, we see that by simply introducing asymmetric modes, the spectral content depletes in the $\lambda = 2\ \mu m$ and $\lambda = 700\ nm$ areas (labeled 1 and 3) and fills in the gap which exists in the $\lambda = [900, 1200]\ nm$ range. These differences lead to a qualitative conclusion: adjusting the modal composition, while keeping all other parameters constant, causes appreciable differences in the emitted dispersive wave, the Raman-scattering, and the third harmonic generation involved in this nonlinear process.
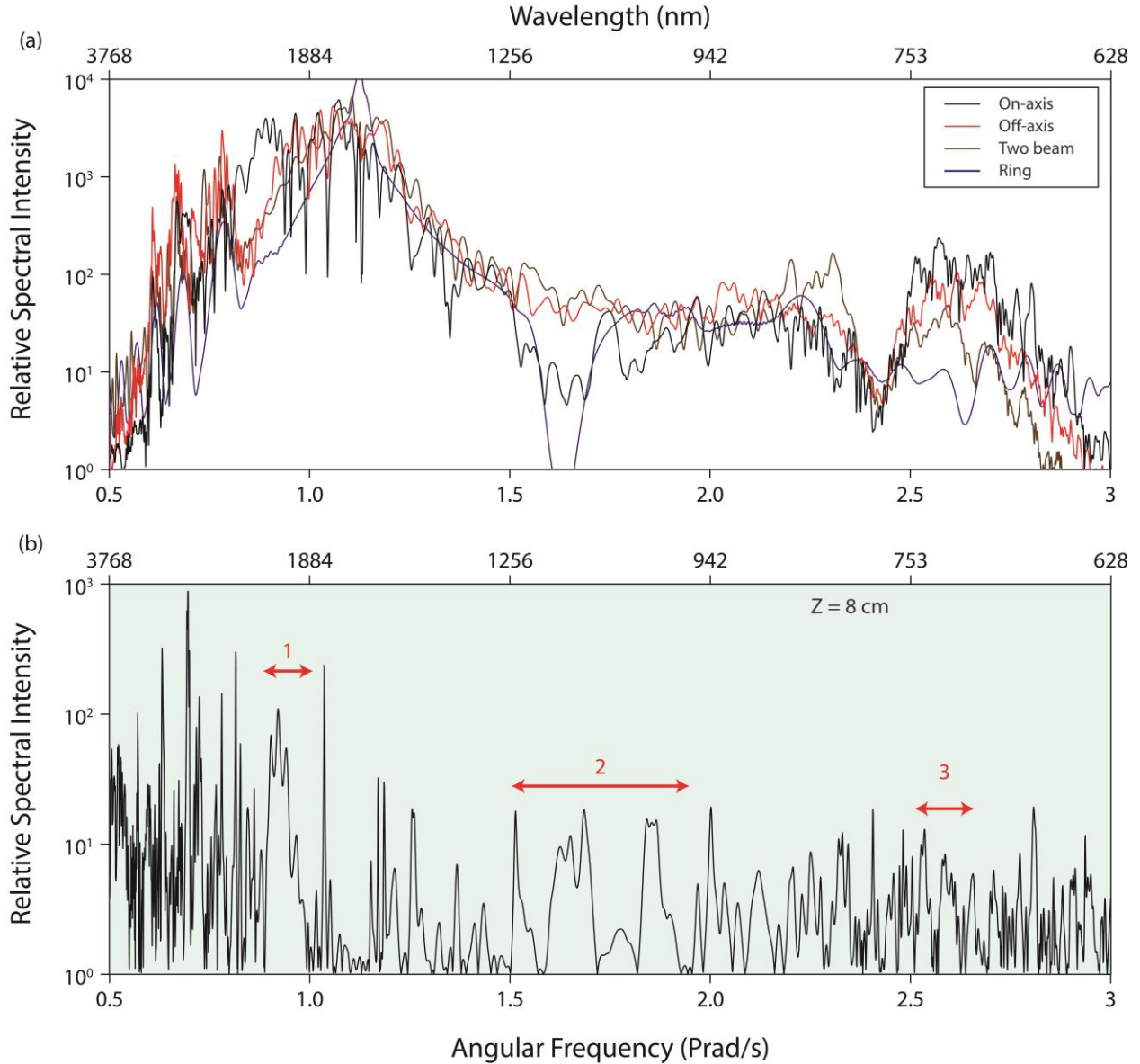
Figure 48| (a) Juxtaposed integrated spectra at $z = 8\ cm$ for the four spatial conditions introduced in Fig. 3. (b). By subtracting the on-axis Gaussian spectrum (Fig. 3a) from the off-axis one (Fig. 3b), a close examination can be made. Doing so reveals three distinct sections where the supercontinuum has appreciably changed.

5.4. Optical rogue waves in nonlinear multimoded fibers

Regardless of the initial spatial distribution of light within the parabolic fiber, a certain condensed and very intense light cluster appears frequently throughout propagation (often in the center of the fiber). Upon inspection, this concentrated entity's FWHM is smaller than the fundamental mode of the fiber and

therefore is composed of multi-modal superpositions. Although the initial wavefront is far below critical self-focusing powers, this condensed spot can still lead to erratic extreme-intensity rogue events on the order of $10 \, TW/cm^2$. Fig. 49 compares the number of freak wave occurrences encountered throughout the propagation of the on-axis Gaussian (Fig. 49a) and the colliding off-axis Gaussians (Fig. 49c).
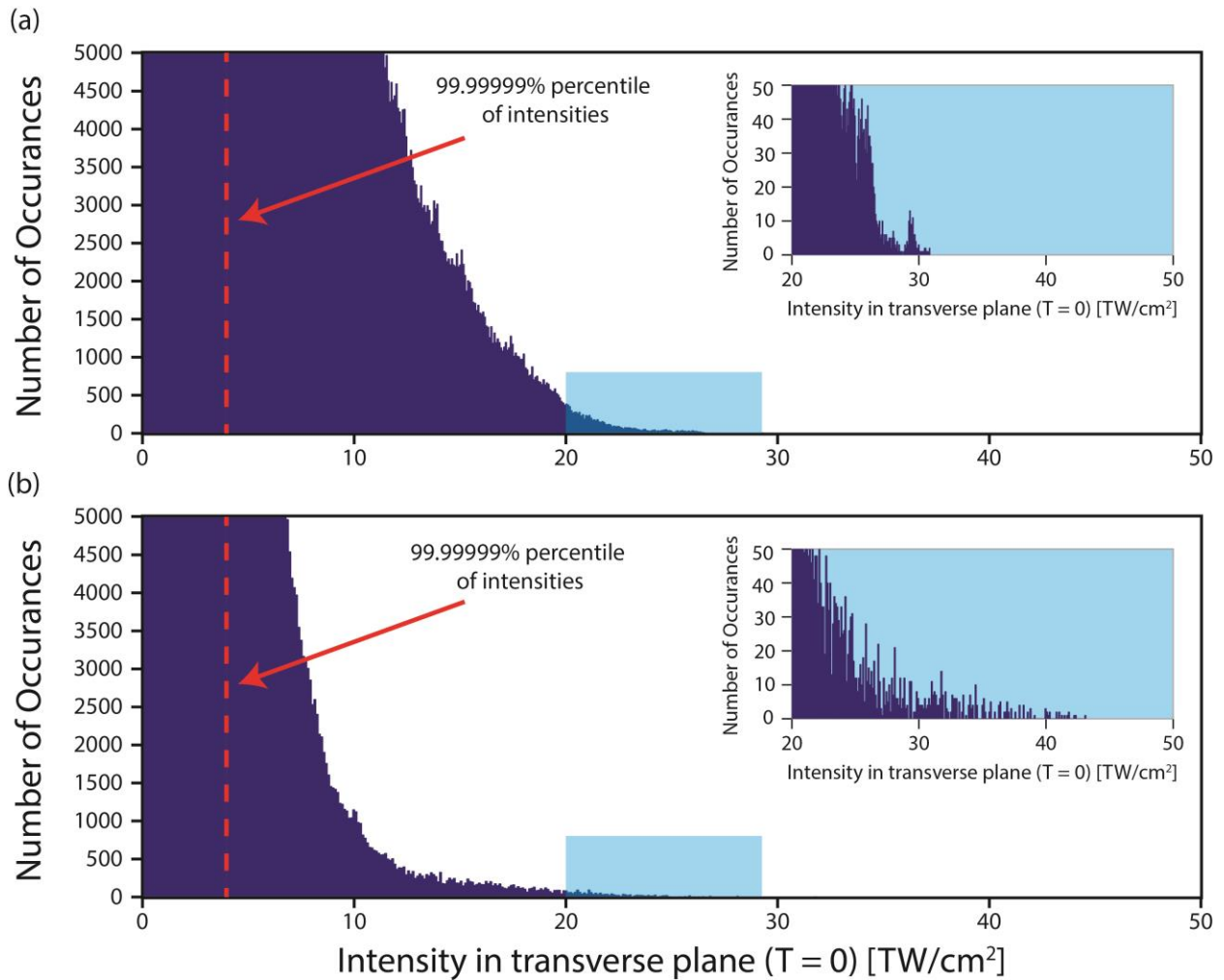
Figure 49| Histograms recording the number of rogue wave events for the (a) on-axis Gaussian (Fig. 47a) and (b) colliding off-axis Gaussian cases (Fig. 47c). Note that the former condition produces more high intensity events on average whereas the latter occasionally induces supremely high intensities on the order of $\mathbf{40 \, TW/cm^2}$.

We see from Fig. 49a that the on-axis Gaussian beam produces more intense events on average. This is because nearly all the radiation is localized in the center of the fiber during its propagation. On the

91

other hand, Fig. 49b, conveys that two colliding off-axis Gaussians cause ultra-high spikes on the order of $40\ TW/cm^2$. The increased likelihood of these exceptionally intense events is a direct result of the abundance of superimposed spatial modes that Fig. 47c produces throughout its propagation.

5.5. Future directions: concatenating nonlinear multimode fibers

One prospect that holds promise for ultra-broad supercontinuum generation is fiber concatenation. The idea is that each and every material has advantages and disadvantages with respect to what wavelengths they can produce, and that this limitation can be bypassed by making use of multiple different media during propagation. For example, silica glass fiber, which produces an appreciable supercontinuum from $\lambda \approx 500\ nm$ to $\lambda \approx 2000\ nm$, cannot reach beyond these colors due to absorption peaks (Fig. 45). However, other materials like ZBLAN (shown in Fig. 50) can stretch much further into the infrared; particularly nice are chalcogenide fibers which are highly nonlinear and are reasonably transparent from $\lambda \approx 3\ \mu m$ to $\lambda \approx 7\ \mu m$ [110-112].
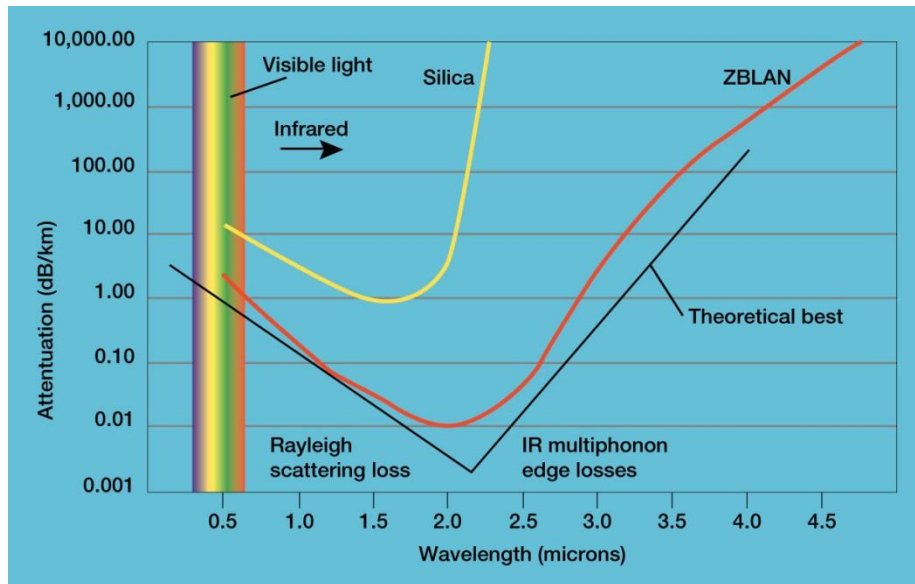
Figure 50: Attenuation of Silica and ZBLAN fibers. From the absorption spectrum, we see that ZBLAN is a material which can potentially produce a supercontinuum extending much further the infrared.

Let us now assume that we have a parabolic silica glass fiber which has produced a supercontinuum similar to that of Fig. 44b. We then take this radiation, couple it into a chalcogenide fiber, and propagate further. Our material parameters for the chalcogenide glass assume a combination of As_2S_3 and As_2Se_3 [111, 112].
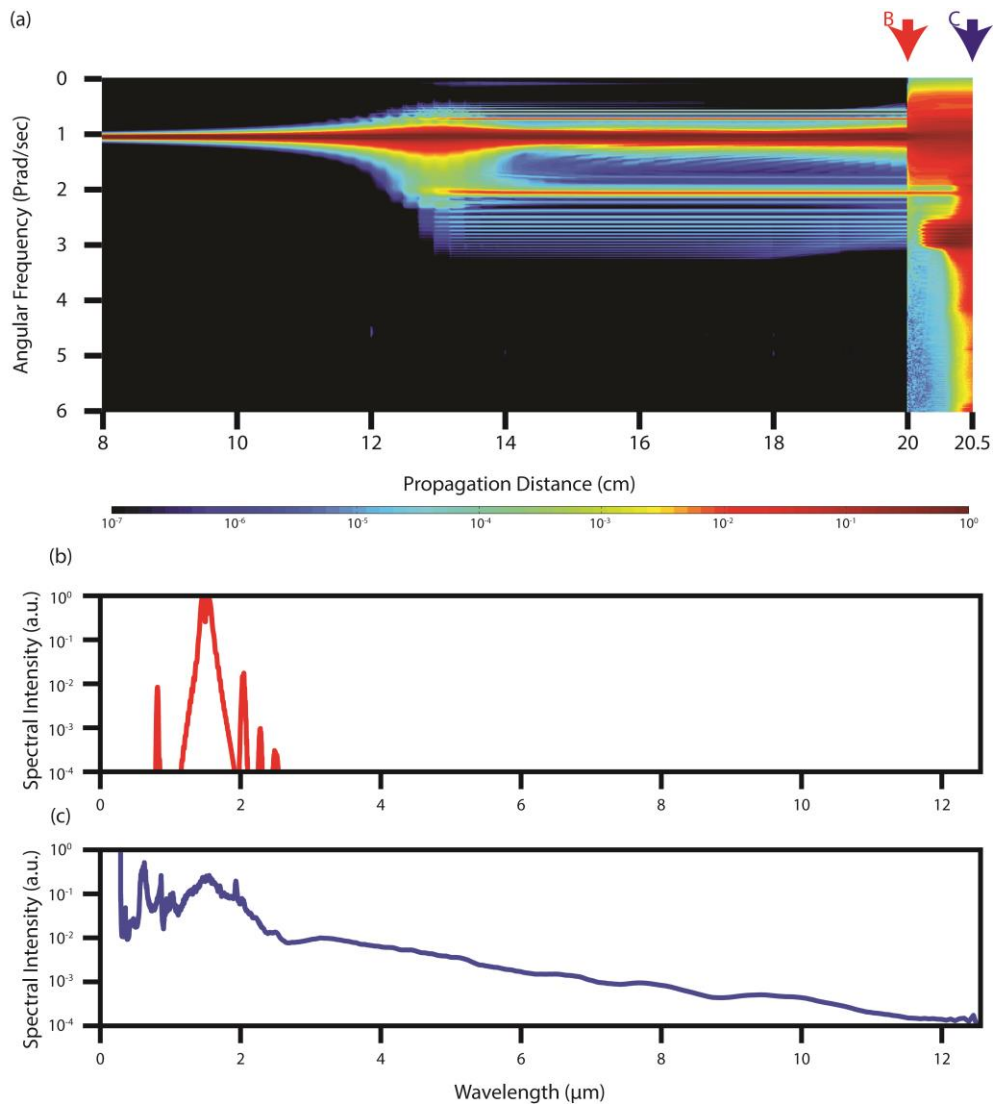
Figure 51| Concatenated silica glass and chalcogenide fibers. (a) Propagation showing the production of supercontinuum. (b) Distribution of frequencies at $z = 20\ cm$, just before light is coupled in the chalcogenide fiber. (c) Expansive supercontinuum after only $z = 50\ mm$ of propagation into the chalcogenide fiber.

The simulation results for this concatenation scenario are displayed in Fig. 51. Following the propagation, (Fig. 51a), we see that after the first $z = 20\ cm$, the supercontinuum now spans from $\lambda \approx 700\ nm$ to $\lambda \approx 2.5\ \mu m$. This span is quite small (Fig. 51b) compared to the expansive supercontinuum that forms when the output of the silica fiber is allowed to propagate for only $50\ mm$ in the chalcogenide fiber (Fig. 51c).

CONCLUSIONS

Optical wavefronts which are resilient to diffraction and dispersion offer many possibilities for the future of optics. Whether they are non-spreading Bessel beams, accelerating Airy beams, or localized spatiotemporal entities resembling the spherical symmetries of hydrogen quantum orbitals, these diffractionless self-healing linear beams will without a doubt be found in a multitude of forthcoming applications. In the nonlinear regime, dressed optical filaments can greatly extend the longevity of an optical filament by prudently providing an auxiliary dress beam to act as a secondary energy reservoir. This not only opens up the possibilities connected to long-range filamentation experiments including remote detection and weather control, but also in settings where higher harmonic generation is possible via these same phenomena. Finally, in nonlinear multimode optical fibers, the nonlinear generation of versatile supercontinuums remains a promising avenue in a variety of subjects ranging from optical metrology, rogue wave production, and spectroscopy, to microscopy and biomedicine. Exceptionally expansive and malleable supercontinuums are possible via several methods including the tailoring of initial spatial conditions of the lauch beam or concatenating different fiber materials.

LIST OF REFERENCES

1.   J. W. Goodman, *Introduction to Fourier Optics* (McGraw-Hill, 1968).

2.   A. Sommerfeld, *Partial differential equations in physics* (Elsevier Science, 1949).

3.   B. E. A. Saleh and M. C. Teich, *Fundamentals of photonics*, Wiley series in pure and applied optics (Wiley, New York, 1991), pp. xviii, 966 p.

4.   O. Svelto and D. C. Hanna, *Principles of lasers,* 2nd ed. (Plenum Press, New York, 1982), pp. xv, 375 p.

5.   J. Durnin, J. J. Miceli, and J. H. Eberly, "Diffraction-Free Beams," J Opt Soc Am A **3**, P128-P128 (1986).

6.   J. Durnin, J. J. Miceli, and J. H. Eberly, "Diffraction-Free Beams," Phys Rev Lett **58**, 1499-1501 (1987).

7.   M. A. Bandres, J. C. Gutierrez-Vega, and S. Chavez-Cerda, "Parabolic nondiffracting optical wave fields," Opt Lett **29**, 44-46 (2004).

8.   D. N. Christodoulides, N. K. Efremidis, P. Di Trapani, and B. A. Malomed, "Bessel X waves in two- and three-dimensional bidispersive optical systems," Opt Lett **29**, 1446-1448 (2004).

9.   O. Manela, M. Segev, and D. N. Christodoulides, "Nondiffracting beams in periodic media," Opt Lett **30**, 2611-2613 (2005).

10. J. C. Gutierrez-Vega, M. D. Iturbe-Castillo, and S. Chavez-Cerda, "Alternative formulation for invariant optical fields: Mathieu beams," Opt Lett **25**, 1493-1495 (2000).

11. G. A. Siviloglou and D. N. Christodoulides, "Accelerating finite energy Airy beams," Opt Lett **32**, 979-981 (2007).

12. M. S. Mills, G. A. Siviloglou, N. Efremidis, T. Graf, E. M. Wright, J. V. Moloney, and D. N. Christodoulides, "Localized waves with spherical harmonic symmetries," Phys Rev A **86**(2012).

13. M. A. Porras and P. Di Trapani, "Localized and stationary light wave modes in dispersive media," Phys Rev E **69**(2004).

14. P. Aleahmad, M. A. Miri, M. S. Mills, I. Kaminer, M. Segev, and D. N. Christodoulides, "Fully Vectorial Accelerating Diffraction-Free Helmholtz Beams," Phys Rev Lett **109**(2012).

15. A. Chong, W. H. Renninger, D. N. Christodoulides, and F. W. Wise, "Airy-Bessel wave packets as versatile linear light bullets," Nat Photonics **4**, 103-106 (2010).

16. Z. J. Ren, Q. Wu, H. F. Mao, Y. L. Shi, and C. J. Fan, "Propagation characteristics of Airy-Bessel wave packets in free space," Opt Express **21**, 4481-4492 (2013).

17. G. Hausler and W. Heckel, "Light Sectioning with Large Depth and High-Resolution," Appl Optics **27**, 5165-5169 (1988).

18. K. M. Iftekharuddin and M. A. Karim, "Heterodyne-Detection by Using a Diffraction-Free Beam - Tilt and Offset Effects," Appl Optics **31**, 4853-4856 (1992).

19. T. Wulle and S. Herminghaus, "Nonlinear Optics of Bessel Beams," Phys Rev Lett **70**, 1401-1404 (1993).

20. V. Garces-Chavez, D. McGloin, H. Melville, W. Sibbett, and K. Dholakia, "Simultaneous micromanipulation in multiple planes using a self-reconstructing light beam," Nature **419**, 145-147 (2002).

21. J. Arlt, V. Garces-Chavez, W. Sibbett, and K. Dholakia, "Optical micromanipulation using a Bessel light beam," Opt Commun **197**, 239-245 (2001).

22. P. Zhang, J. Prakash, Z. Zhang, M. S. Mills, N. K. Efremidis, D. N. Christodoulides, and Z. G. Chen, "Trapping and guiding microparticles with morphing autofocusing Airy beams," Opt Lett **36**, 2883-2885 (2011).

23. Z. Zhang, P. Zhang, M. Mills, Z. G. Chen, D. N. Christodoulides, and J. J. Liu, "Trapping aerosols with optical bottle arrays generated through a superposition of multiple Airy beams," Chin Opt Lett **11**(2013).

24.   R. P. MacDonald, S. A. Boothroyd, T. Okamoto, J. Chrostowski, and B. A. Syrett, "Interboard optical data distribution by Bessel beam shadowing," Opt Commun **122**, 169-177 (1996).

25.   C. Altucci, R. Bruzzese, C. de Lisio, A. Porzio, S. Solimeno, and V. Tosa, "Diffractionless beams and their use for harmonic generation," Opt Laser Eng **37**, 565-575 (2002).

26.   C. Altucci, R. Bruzzese, D. D?Antuoni, C. de Lisio, and S. Solimeno, "Harmonic generation in gases by use of Bessel?Gauss laser beams," J. Opt. Soc. Am. B **17**, 34-42 (2000).

27.   R. M. Herman and T. A. Wiggins, "Production and Uses of Diffractionless Beams," J Opt Soc Am A **8**, 932-942 (1991).

28.   R. Arimoto, C. Saloma, T. Tanaka, and S. Kawata, "Imaging Properties of Axicon in a Scanning Optical-System," Appl Optics **31**, 6653-6657 (1992).

29.   V. Grillo, E. Karimi, G. C. Gazzadi, S. Frabboni, M. R. Dennis, and R. W. Boyd, "Generation of Nondiffracting Electron Bessel Beams," Physical Review X **4**, 011013 (2014).

30.   M. Erdélyi, Z. L. Horváth, G. Szabó, Z. Bor, F. K. Tittel, J. R. Cavallaro, and M. C. Smayling, "Generation of diffraction-free beams for applications in optical microlithography," Journal of Vacuum Science & Technology B **15**, 287-292 (1997).

31.   D. McGloin and K. Dholakia, "Bessel beams: diffraction in a new light," Contemp Phys **46**, 15-28 (2005).

32.   Z. Bouchal, J. Wagner, and M. Chlup, "Self-reconstruction of a distorted nondiffracting beam," Opt Commun **151**, 207-211 (1998).

33.   M. Born and E. Wolf, *Principles of optics : electromagnetic theory of propagation, interference and diffraction of light,* 6th (corr.) ed. (Cambridge University Press, Cambridge, UK ; New York ;, 1997), pp. xxviii, 808 p.

34.   J. Durnin, J. J. Miceli, and J. H. Eberly, "Durnin, Miceli, and Eberly reply," Phys Rev Lett **66**, 838-838 (1991).

35.   F. Gori, G. Guattari, and C. Padovani, "Bessel-Gauss beams," Opt Commun **64**, 491-495 (1987).

36. G. A. Siviloglou, J. Broky, A. Dogariu, and D. N. Christodoulides, "Observation of accelerating airy beams," Phys Rev Lett **99**(2007).

37. M. A. Bandres, I. Kaminer, M. Mills, B. M. Rodríguez-Lara, E. Greenfield, M. Segev, and D. N. Christodoulides, "Accelerating Optical Beams," Opt. Photon. News **24**, 30-37 (2013).

38. J. Broky, G. A. Siviloglou, A. Dogariu, and D. N. Christodoulides, "Self-healing properties of optical Airy beams," Opt Express **16**, 12880-12891 (2008).

39. G. A. Siviloglou, J. Broky, A. Dogariu, and D. N. Christodoulides, "Ballistic dynamics of Airy beams," Opt Lett **33**, 207-209 (2008).

40. D. M. Greenberger, "Comment on ''Nonspreading wave packets''," Am J Phys **48**, 256-256 (1980).

41. D. Abdollahpour, S. Suntsov, D. G. Papazoglou, and S. Tzortzakis, "Spatiotemporal Airy Light Bullets in the Linear and Nonlinear Regimes," Phys Rev Lett **105**, 253901 (2010).

42. T. Juhasz, F. H. Loesel, R. M. Kurtz, C. Horvath, J. F. Bille, and G. Mourou, "Corneal refractive surgery with femtosecond lasers," Selected Topics in Quantum Electronics, IEEE Journal of **5**, 902-910 (1999).

43. M. Mlejnek, E. M. Wright, and J. V. Moloney, "Dynamic spatial replenishment of femtosecond pulses propagating in air," Opt. Lett. **23**, 382-384 (1998).

44. N. K. Efremidis and D. N. Christodoulides, "Abruptly autofocusing waves," Opt Lett **35**, 4045-4047 (2010).

45. I. Chremmos, N. K. Efremidis, and D. N. Christodoulides, "Pre-engineered abruptly autofocusing beams," Opt Lett **36**, 1890-1892 (2011).

46. A. Torre, "Airy beams beyond the paraxial approximation," Opt Commun **283**, 4146-4165 (2010).

47. A. V. Novitsky and D. V. Novitsky, "Nonparaxial Airy beams: role of evanescent waves," Opt Lett **34**, 3430-3432 (2009).

48.   L. Froehly, F. Courvoisier, A. Mathis, M. Jacquot, L. Furfaro, R. Giust, P. A. Lacourt, and J. M. Dudley, "Arbitrary accelerating micron-scale caustic beams in two and three dimensions," Opt Express **19**, 16455-16465 (2011).

49.   I. Kaminer, R. Bekenstein, J. Nemirovsky, and M. Segev, "Nondiffracting Accelerating Wave Packets of Maxwell's Equations," Phys Rev Lett **108**, 163901 (2012).

50.   I. Kaminer, J. Nemirovsky, and M. Segev, "Self-accelerating self-trapped nonlinear beams of Maxwell's equations," Opt Express **20**, 18827-18835 (2012).

51.   P. Zhang, Y. Hu, T. Li, D. Cannan, X. Yin, R. Morandotti, Z. Chen, and X. Zhang, "Nonparaxial Mathieu and Weber Accelerating Beams," Phys Rev Lett **109**, 193901 (2012).

52.   B. A. Malomed, D. Mihalache, F. Wise, and L. Torner, "Spatiotemporal optical solitons," J Opt B-Quantum S O **7**, R53-R72 (2005).

53.   Y. Silberberg, "Collapse of Optical Pulses," Opt Lett **15**, 1282-1284 (1990).

54.   S. Longhi, "Localized subluminal envelope pulses in dispersive media," Opt Lett **29**, 147-149 (2004).

55.   J. Y. Lu and J. F. Greenleaf, "Nondiffracting X-Waves - Exact-Solutions to Free-Space Scalar Wave-Equation and Their Finite Aperture Realizations," Ieee T Ultrason Ferr **39**, 19-31 (1992).

56.   P. Di Trapani, G. Valiulis, A. Piskarskas, O. Jedrkiewicz, J. Trull, C. Conti, and S. Trillo, "Spontaneously generated X-shaped light bullets," Phys Rev Lett **91**(2003).

57.   H. Sonajalg, M. Ratsep, and P. Saari, "Demonstration of the Bessel-X pulse propagating with strong lateral and longitudinal localization in a dispersive medium (vol 22, pg 310, 1997)," Opt Lett **22**, 745-745 (1997).

58.   S. Malaguti, G. Bellanca, and S. Trillo, "Two-dimensional envelope localized waves in the anomalous dispersion regime," Opt Lett **33**, 1117-1119 (2008).

59.   S. Malaguti and S. Trillo, "Envelope localized waves of the conical type in linear normally dispersive media," Phys Rev A **79**, 063803 (2009).

60. X. Liu, L. J. Qian, and F. W. Wise, "Generation of optical spatiotemporal solitons," Phys Rev Lett **82**, 4631-4634 (1999).

61. M. Dallaire, N. McCarthy, and M. Piche, "Spatiotemporal bessel beams: theory and experiments," Opt Express **17**, 18148-18164 (2009).

62. S. Lopez-Aguayo, Y. V. Kartashov, V. A. Vysloukh, and L. Torner, "Method to Generate Complex Quasinondiffracting Optical Lattices," Phys Rev Lett **105**(2010).

63. O. V. Borovkova, Y. V. Kartashov, V. E. Lobanov, V. A. Vysloukh, and L. Torner, "General quasi-nonspreading linear three-dimensional wave packets," Opt Lett **36**, 2176-2178 (2011).

64. A. Braun, G. Korn, X. Liu, D. Du, J. Squier, and G. Mourou, "Self-Channeling of High-Peak-Power Femtosecond Laser-Pulses in Air," Opt Lett **20**, 73-75 (1995).

65. A. Couairon and A. Mysyrowicz, "Femtosecond filamentation in transparent media," Phys Rep **441**, 47-189 (2007).

66. G. Méchain, A. Couairon, Y. B. André, C. D'Amico, M. Franco, B. Prade, S. Tzortzakis, A. Mysyrowicz, and R. Sauerbrey, "Long-range self-channeling of infrared laser pulses in air: a new propagation regime without ionization," Appl Phys B **79**, 379-382 (2004).

67. M. Rodriguez, R. Bourayou, G. Méjean, J. Kasparian, J. Yu, E. Salmon, A. Scholz, B. Stecklum, J. Eislöffel, U. Laux, A. P. Hatzes, R. Sauerbrey, L. Wöste, and J.-P. Wolf, "Kilometer-range nonlinear propagation of femtosecond laser pulses," Phys Rev E **69**, 036607 (2004).

68. G. Méchain, C.D'Amico, Y. B. André, S. Tzortzakis, M. Franco, B. Prade, A. Mysyrowicz, A. Couairon, E. Salmon, and R. Sauerbrey, "Range of plasma filaments created in air by a multi-terawatt femtosecond laser," Opt Commun **247**, 171-180 (2005).

69. I. S. Golubtsov, V. P. Kandidov, and O. G. Kosareva, "Initial phase modulation of a high-power femtosecond laser pulse as a tool for controlling its filamentation and generation of a supercontinuum in air," Quantum Electron+ **33**, 525 (2003).

70.   H. Wille, M. Rodriguez, J. Kasparian, D. Mondelain, J. Yu, A. Mysyrowicz, R. Sauerbrey, J. P. Wolf, and L. Woste, "Teramobile: A mobile femtosecond-terawatt laser and detection system," Eur Phys J-Appl Phys **20**, 183-190 (2002).

71.   Y. Fu, H. Xiong, H. Xu, J. Yao, B. Zeng, W. Chu, Y. Cheng, Z. Xu, W. Liu, and S. L. Chin, "Generation of extended filaments of femtosecond pulses in air by use of a single-step phase plate," Opt. Lett. **34**, 3752-3754 (2009).

72.   A. Couairon, G. Mechain, S. Tzortzakis, M. Franco, B. Lamouroux, B. Prade, and A. Mysyrowicz, "Propagation of twin laser pulses in air and concatenation of plasma strings produced by femtosecond infrared filaments," Opt Commun **225**, 177-192 (2003).

73.   S. Tzortzakis, G. Méchain, G. Patalano, M. Franco, B. Prade, and A. Mysyrowicz, "Concatenation of plasma filaments created in air by femtosecond infrared laser pulses," Appl Phys B **76**, 609-612 (2003).

74.   P. Polynkin, M. Kolesik, A. Roberts, D. Faccio, P. Di Trapani, and J. Moloney, "Generation of extended plasma channels in air using femtosecond Bessel beams," Opt. Express **16**, 15733-15740 (2008).

75.   P. Polynkin, M. Kolesik, and J. Moloney, "Extended filamentation with temporally chirped femtosecond Bessel-Gauss beams in air," Opt Express **17**, 575-584 (2009).

76.   M. Mlejnek, M. Kolesik, J. Moloney, and E. Wright, "<title>Optically Turbulent Femtosecond Light Guide in Air</title>," Phys Rev Lett **83**, 2938-2941 (1999).

77.   W. Liu, F. Theberge, E. Arevalo, J. F. Gravel, A. Becker, and S. L. Chin, "Experiment and simulations on the energy reservoir effect in femtosecond light filaments," Opt Lett **30**, 2602-2604 (2005).

78.   W. Liu, J. F. Gravel, F. Theberge, A. Becker, and S. L. Chin, "Background reservoir: its crucial role for long-distance propagation of femtosecond laser pulses in air," Appl Phys B-Lasers O **80**, 857-860 (2005).

79.   M. Kolesik and J. V. Moloney, "Nonlinear optical pulse propagation simulation: From Maxwell's to unidirectional equations," Phys Rev E **70**(2004).

80.   J. K. Wahlstrand, Y. H. Cheng, and H. M. Milchberg, "Absolute measurement of the transient optical nonlinearity in N${}_{2}$, O${}_{2}$, N${}_{2}$O, and Ar," Phys Rev A **85**, 043820 (2012).

81.   J. Kasparian, R. Sauerbrey, and S. L. Chin, "The critical laser intensity of self-guided light filaments in air," Appl Phys B **71**, 877-879 (2000).

82.   A. Couairon, E. Brambilla, T. Corti, D. Majus, O. Ramírez-Góngora, and M. Kolesik, "Practitioner's guide to laser pulse propagation models and simulation," Eur. Phys. J. Spec. Top. **199**, 5-76 (2011).

83.   J. H. Marburger, "Self-focusing: Theory," Progress in Quantum Electronics **4, Part 1**, 35-110 (1975).

84.   A. Becker, N. Akozbek, K. Vijayalakshmi, E. Oral, C. M. Bowden, and S. L. Chin, "Intensity clamping and re-focusing of intense femtosecond laser pulses in nitrogen molecular gas," Appl Phys B-Lasers O **73**, 287-290 (2001).

85.   M. Mills, H. Matthias, K. Miroslav, and C. Demetrios, "Extending optical filaments using auxiliary dress beams," Journal of Physics B: Atomic, Molecular and Optical Physics **48**, 094014 (2015).

86.   M. S. Mills, M. Kolesik, and D. N. Christodoulides, "Dressed optical filaments," Opt. Lett. **38**, 25-27 (2013).

87.   R. R. Alfano and S. L. Shapiro, "Emission in the Region 4000 to 7000 Angstroms Via Four-Photon Coupling in Glass," Phys Rev Lett **24**, 584-587 (1970).

88.   W. Yu, R. R. Alfano, C. L. Sam, and R. J. Seymour, "Spectral broadening of picosecond 1.06 μ pulse in KBr," Opt Commun **14**, 344-347 (1975).

89.   W. L. Smith, P. Liu, and N. Bloembergen, "Superbroadening in H20 and D20 by self-focused picosecond pulses from a YAlG: Nd laser," Phys Rev A **15**, 2396-2403 (1977).

90.   R. L. Fork, W. J. Tomlinson, C. V. Shank, C. Hirlimann, and R. Yen, "Femtosecond white-light continuum pulses," Opt Lett **8**, 1-3 (1983).

91.   P. B. Corkum, P. P. Ho, R. R. Alfano, and J. T. Manassah, "Generation of infrared supercontinuum covering 3-14 micron in dielectrics and semiconductors," Opt Lett **10**, 624-626 (1985).

92.   J. H. Glownia, J. Misewich, and P. P. Sorokin, "Ultrafast ultraviolet pump?probe apparatus," J. Opt. Soc. Am. B **3**, 1573-1579 (1986).

93.   J. M. Dudley, G. Genty, and S. Coen, "Supercontinuum generation in photonic crystal fiber," Rev Mod Phys **78**, 1135-1184 (2006).

94.   T. A. Birks, W. J. Wadsworth, and P. S. Russell, "Supercontinuum generation in tapered fibers," Opt Lett **25**, 1415-1417 (2000).

95.   S. L. Chin, S. A. Hosseini, W. Liu, Q. Luo, F. Theberge, N. Akozbek, A. Becker, V. P. Kandidov, O. G. Kosareva, and H. Schroeder, "The propagation of powerful femtosecond laser pulses in optical media: physics, applications, and new challenges," Can J Phys **83**, 863-905 (2005).

96.   R. E. Slusher, G. Lenz, J. Hodelin, J. Sanghera, L. B. Shaw, and I. D. Aggarwal, "Large Raman gain and nonlinear phase shifts in high-purity As2Se3 chalcogenide fibers," J. Opt. Soc. Am. B **21**, 1146-1155 (2004).

97.   B. J. Eggleton, B. Luther-Davies, and K. Richardson, "Chalcogenide photonics," Nat Photonics **5**, 141-148 (2011).

98.   M. Z. Aleksei, "Let there be white light: supercontinuum generation by ultrashort laser pulses," Physics-Uspekhi **49**, 605 (2006).

99.   L. G. Wright, W. H. Renninger, D. N. Christodoulides, and F. W. Wise, "Spatiotemporal dynamics of multimode optical solitons," Opt Express **23**, 3492-3506 (2015).

100.   A. Mecozzi, C. Antonelli, and M. Shtaif, "Nonlinear propagation in multi-mode fibers in the strong coupling regime," Opt Express **20**, 11673-11678 (2012).

101.   A. Mafi, "Pulse Propagation in a Short Nonlinear Graded-Index Multimode Optical Fiber," Lightwave Technology, Journal of **30**, 2803-2811 (2012).

102.   G. P. Agrawal, "Nonlinear fiber optics: its history and recent progress [Invited]," J Opt Soc Am B **28**, A1-A10 (2011).

103.   S. Mumtaz, R. Essiambre, and G. P. Agrawal, "Nonlinear Propagation in Multimode and Multicore Fibers: Generalization of the Manakov Equations," Lightwave Technology, Journal of **31**, 398-406 (2013).

104.   M. Kolesik and J. V. Moloney, "Nonlinear optical pulse propagation simulation: From Maxwell's to unidirectional equations," Phys Rev E **70**, 036604 (2004).

105.   D. Hollenbeck and C. D. Cantrell, "Multiple-vibrational-mode model for fiber-optic Raman gain spectrum and response function," J. Opt. Soc. Am. B **19**, 2886-2892 (2002).

106.   K. Okamoto, "Chapter 3 - Optical fibers," in *Fundamentals of Optical Waveguides (Second Edition)*, K. Okamoto, ed. (Academic Press, Burlington, 2006), pp. 57-158.

107.   A. K. Ghatak and K. Thyagarajan, *An introduction to fiber optics* (Cambridge University Press, Cambridge ; New York, 1998), pp. xvi, 565 p.

108.   S. M. J. Kelly, "Characteristic sideband instability of periodically amplified average soliton," Electron Lett **28**, 806-807 (1992).

109.   C. Lin and R. H. Stolen, "New nanosecond continuum for excited-state spectroscopy," Appl Phys Lett **28**, 216-218 (1976).

110.   F. Théberge, N. Thiré, J.-F. Daigle, P. Mathieu, B. E. Schmidt, Y. Messaddeq, R. Vallée, and F. Légaré, "Multioctave infrared supercontinuum generation in large-core As2S3 fibers," Opt Lett **39**, 6474-6477 (2014).

111.   E. Guillevic, X. Zhang, T. Pain, L. Calvez, J.-L. Adam, J. Lucas, M. Guilloux-Viry, S. Ollivier, and G. Gadret, "Optimization of chalcogenide glass in the As–Se–S system for automotive applications," Opt Mater **31**, 1688-1692 (2009).

112.   G. Boudebs, S. Cherukulappurath, M. Guignard, J. Troles, F. Smektala, and F. Sanchez, "Linear optical characterization of chalcogenide glasses," Opt Commun **230**, 331-336 (2004).